Silicon Based MBE of Manganese-Silicide and Silicon-Suboxide

Dissertation zur Erlangung des
naturwissenschaftlichen Doktorgrades
der Bayerischen Julius-Maximilians-Universität Würzburg

vorgelegt von

Christoph Pohl

aus Oldenburg

Würzburg 2013

Eingereicht am: 08.04.2013
bei der Fakultät für Physik und Astronomie

1. Gutachter: Prof. Dr. K. Brunner
2. Gutachter: Prof. Dr. J. Pflaum
der Dissertation.

1. Prüfer: Prof. Dr. K. Brunner
2. Prüfer: Prof. Dr. J. Pflaum
3. Prüfer: Prof. Dr. R. Oppermann
im Promotionskolloquium.

Tag des Promotionskolloquiums: 04.11.2013

Doktorurkunde ausgehändigt am: .....

From birth, man carries the weight of gravity on his shoulders. He is bolted to earth. But man has only to sink beneath the surface and he is free.

Jacques Cousteau (French Explorer, 1910-1997)

Abstract

The present thesis deals with the fabrication, optimization of growth process and characterization of silicon based materials with molecular beam epitaxy. Two material systems are investigated in the course of this work: silicon/silicon suboxide multilayer structures and mono manganese silicide thin films.

Mono manganese silicide (MnSi) is grown on Si(111) substrates with an hydrogen passivated surface, that is prepared by wet chemical processes. The growth start is performed by deposition of an amorphous Mn wetting layer that is subsequently annealed to form a MnSi seed layer on which the MnSi molecular beam epitaxy (MBE) is achieved. An amorphous or a crystalline Si cap layer is deposited onto the MnSi film to finalize the growth process and protect the sample from oxidation. With Raman spectroscopy it is shown that the crystalline cap layer is in fact single crystalline silicon.

Results of x-ray diffraction and Raman spectroscopy confirm the growth of mono manganese silicide in contrast to other existing manganese silicide phases. In addition, in-plane and out-of-plane residual strain, and twinning of the MnSi thin film is detected with x-ray diffraction of symmetric and asymmetric reflections. Orientation between the Si substrate and the MnSi film is determined with the parallel lattice planes MnSi(210) and Si(511).

Transport measurements show a T^2 dependence of the resistivity below 30 K and metallic behavior above, a magneto resistance of 0.9 % and an unusual memory like effect of the resistance for an in-plane magnetic field sweep measurement.

Silicon/Silicon suboxide (SiO_x) multilayer structures are grown on Si(100) by interrupting the Si growth and oxidizing the surface with molecular oxygen. During oxidation the RHEED pattern changes from the Si(2×1) reconstruction to an amorphous pattern. When silicon growth is resumed a spotty RHEED pattern emerges, indicating a rough, three dimensional surface. The rough surface can be smoothed out with Si growth at substrate temperatures between 600°C and 700°C. Measurements with transmission electron microscopy show that a silicon suboxide layer of about 1 nm embedded in single crystalline silicon is formed with the procedure. Multilayer structures are achieved by repeating the oxidation procedure when the Si spacer layer has a smooth and flat surface. The oxygen content of the suboxide layers can be varied between 7.6 % and 26.8 %, as

determined with secondary ion mass spectrometry and custom-built simulations models for the x-ray diffraction.

Structural stability of the multilayer structures is investigated by x-ray diffraction before and after rapid thermal annealing. For temperatures up to 1000°C the multilayer structures show no modification of the SiO_x layer in x-ray diffraction.

Zusammenfassung

Die vorgelegte Arbeit handelt von der Herstellung siliziumbasierter Materialien mittels Molekularstrahlepitaxie, der Charakterisierung der Proben und der Optimierung der Wachstumsprozesse. Zwei Materialsysteme werden in dieser Arbeit behandelt: Silizium/Siliziumsuboxid Vielschichtstrukturen und dünne Schichten Mono-Mangansilizid.

Mono-Mangansilizid (MnSi) wird auf Wasserstoff passivierten Si(111)-Substraten gewachsen. Für den Wachstumsstart wird eine amorphe Schicht Mangan auf den Si-Wafer abgeschieden und anschließend getempert. Dieser Prozess erzeugt eine ultra dünne Schicht MnSi, die als Keimschicht für das Wachstum dient. Zum Abschluss des Wachstums wird die MnSi-Schicht mit einer amorphen oder einkristallinen Deckschicht vor dem Oxidieren an der Luft geschützt. Das einkristalline Überwachsen der MnSi-Schicht ist mittels Ramanspektroskopie bestätigt.

Röntgendiffraktometrie und Ramanspektroskopie bestätigen, dass es sich bei der gewachsenen Schicht um MnSi handelt und nicht um die manganreiche oder siliziumreiche Phasen von Mangansilizid. Anhand der Röntgendiffraktometrie von symmetrischen und asymmetrischen Reflektionen wird die laterale und vertikale Restverspannung gemessen, zusätzlich wird die Entstehung von Zwillingen in der Schicht gezeigt. Die Orientierung der MnSi-Schicht relativ zum Si Substrat ist anhand der parallelen Netzebenen MnSi(210) und Si(511) bestimmt.

Transportmessungen an den Schichten zeigen unterhalb von 30 K eine T^2-Abhängigkeit des spezifischen Widerstands, oberhalb metallisches Verhalten. Der Magneto Widerstand der MnSi Schicht beträgt 0.9 %. Bei einem Magnetfeldsweep in der Schichtebene wird ein kurioses, dem Memory-Effekt ähnliches Verhalten beobachtet.

Silizium/Siliziumsuboxid (SiO_x)-Vielschichtstrukturen werden auf Si(100) Substraten gewachsen. Das Siliziumwachstum wird unterbrochen und die Probenoberfläche mit molekularem Sauerstoff oxidiert. Dabei verändert sich das RHEED-Muster von der Si-(2×1) Rekonstruktion zu einem amorphen Muster. Das Siliziumwachstum wird nach der Oxidation fortgesetzt und im RHEED entsteht dabei ein Punktmuster das von einer rauen, drei-dimensionalen Oberfläche zeugt. Durch Siliziumwachstum bei Substrattemperaturen zwischen 600°C und 700°C wird die Oberfläche wieder geglättet. Aufnahmen mit dem Transmissionselektronenmikroskop zeigen, dass bei diesem Wachstum eine 1 nm dicke

SiO_x -Schicht eingebettet zwischen einkristalline Siliziumschichten entsteht. Wenn die Siliziumoberfläche wieder glatt ist, kann durch wiederholen der Wachstumssequenz eine Vielschichtstruktur hergestellt werden. Der Sauerstoffgehalt der hergestellten Suboxidschichten wurde mittels Sekundärionen-Massenspektrometrie und eigens zu diesem Zweck angepassten Röntgendiffraktometrie-Simulationen auf 7.6% bis 26.8% bestimmt.

Die strukturelle Stabilität der Proben wurde mit Röntgendiffraktometrie vor und nach kurzem Hochtemperaturtempern untersucht. Bei Temperaturen bis 1000°C kann mittels Röntgendiffraktometrie keine Änderung der Si/SiO_x Vielschicht-Strukturen festgestellt werden.

Contents

List of Abbreviations and Symbols xiii

1 Introduction 1

2 Silicon Based Material Systems 5
2.1 Silicon Epitaxy 5
2.2 Manganese Silicide 7
2.2.1 MnSi Thin Film Growth on Si(111) 8
2.2.2 Properties of MnSi 10
2.3 Silicon Suboxide 10
2.3.1 Theoretical Models 11
2.3.2 Growth Processes at the Si/SiO_2 interface 11
2.3.3 Properties of SiO_x 16

3 Experimental Techniques 17
3.1 Sample Preparation 17
3.2 Molecular Beam Epitaxy 17
3.2.1 Technology and Set-Up of MBE 18
3.2.2 MBE Growth Process and Growth Modes 23
3.3 RHEED 25
3.4 X-Ray Techniques 26
3.4.1 High Resolution X-Ray Diffraction 26
3.4.2 X-Ray Reflectivity 30
3.5 Atomic Force Microscopy 31
3.6 Transmission Electron Microscopy 32
3.7 Secondary Ion Mass Spectrometry 33

4 MnSi Film Growth and Characterization 35
4.1 Preliminary Work 35
4.1.1 Manganese Flux Calculation 35
4.1.2 Manganese Thin Film Annealing 37
4.1.3 Determining Film Material 38
4.1.4 Discussion 40

4.2 Molecular Beam Epitaxy of MnSi 41
4.2.1 Growth of MnSi Thin Films 41
4.2.2 Characterization of MnSi Thin Films 43
4.2.3 Discussion 56
4.3 Summary 57

5 SiO_x Growth and Characterization 59
5.1 Growth and Crystalline Overgrowth of Single SiO_x layer 59
5.1.1 RHEED Observations 60
5.1.2 Verification of Surface Roughness 62
5.1.3 XRD and TEM of Single Layers 66
5.1.4 Qualitative Model of Si/SiO_x/Si Growth 69
5.2 SiO_x Multilayer Structures 72
5.2.1 XRD Measurements and Simulations 73
5.2.2 Optimization of Growth Parameters 86
5.2.3 Further Analysis 95
5.3 Summary 102

Bibliography 105

Acknowledgment 119

List of Abbreviations and Symbols

$a_\perp$ .... vertical lattice constant
a .... lattice constant
$a_{\|}$ .... lateral (in plane) lattice constant
AFM .... atomic force microscopy
ΔH_{vap} .... enthalpy of vaporization
EIES .... electron impact emission spectroscopy
f_m .... misfit
fcc .... face centered cubic
FWHM .... full width at half maximum
HF .... hydrofluoric acid
HMS .... higher manganese silicides
HRTEM .... high resolution transmission electron microscopy
HRXRD .... high resolution x-ray diffraction
k_B .... Boltzmann constant
λ .... wavelength
λ_{mfp} .... mean free path
LN_2 .... liquid nitrogen
Lp correction ... Lorentz polarization correction
m_{O_2} .... mass of oxygen molecule: 31.9988 u
MBE .... molecular beam epitaxy
ML .... mono layer
ν .... Poisson ratio
N_A .... Avogadro constant
ρ .... density
RHEED .... reflection high energy electron diffraction
RBM .... random bond model
RIE .... reactive ion etching
RMM .... random mixture model

RMS .... root mean square
RTA .... rapid thermal annealing
c-Si .... single crystal silicon
SPE .... solid phase epitaxy
SEM .... scanning electron microscopy
SiO_x .... silicon suboxide
SIMS .... secondary ion mass spectrometry
SL .... superlattice
SQUID .... superconducting quantum interference device
STEM .... scanning transmission electron microscopy
STM .... scanning tunneling microscopy
Θ_B .... Bragg angle
TEM .... transmission electron microscopy
TOF-MS .... time of flight mass spectrometer
UHV .... ultra high vacuum
XRD .... x-ray diffraction
XRR .... x-ray reflectivity
XPS .... x-ray photoelectron spectroscopy

Chapter 1

Introduction

Most modern computer technology is based on silicon and its oxide (silicon dioxide). Almost none of the technology that surrounds us today could have been realized without integrated circuits based on silicon. Furthermore, silicon is the second most abundant element in the Earth's crust and therefore a price increase based on material shortage is hardly imaginable. Because of that, semiconductor grade silicon is widely available and cheap compared with other semiconductors. Unfortunately, silicon has disadvantages that are not so easy to overcome, for example silicon has no natural wide gap alloy and silicon exhibits a non magnetic behavior. To eliminate these disadvantages, the combination of materials with the desired properties and silicon has been attempted.

Combination of materials with different properties—and especially different crystallographic properties—is a difficult task. The mismatch in lattice constant or different crystallographic orientations often leads to crystal defects, polycrystalline or amorphous growth. Chemical growth methods are not fit to produce the required material combinations, whereas with vacuum deposition techniques some of these problems can be solved. When it comes to very high crystalline quality of single-crystal thin films, molecular beam epitaxy (MBE) has become a fundamental tool for crystal growth. Although expensive and not yet established for mass production in industry, the advantages (e.g.: precise thickness control and abrupt material interfaces) of MBE for research cannot be matched by any other method for thin film growth.

Manganese silicide is an intermetallic compound of the class of weak itinerant-electron magnets that exhibits helimagnetism and has become a highly interesting material for research. There are several unusual properties; some have already led to interesting studies and are predicted to enable new insights into physics. For example, there is a magnetic phase with a transition temperature approaching zero when the pressure reaches $\sim$1.4 GPa [TFL89]. This has raised interest in the material, because it opens the possibility of observing quantum critical phenomena [Sti07]. Further investigations revealed a deviation from the Fermi-liquid behavior in the paramagnetic phase [PJL01; DL03], as well as several anomalies in the properties of MnSi in the vicinity of the magnetic phase transition. For example, the resistivity shows an anomaly around the phase transition

[The95]. Furthermore, Pfleiderer et al. found partial ordering of the spin states in the paramagnetic phase [Pfl04]. During further investigations of the helical magnetic phase of MnSi, Pfleiderer's group made a very surprising discovery. By mistake they observed a skyrmion phase in MnSi below the Curie temperature in an applied magnetic field [Day09]. "The skyrmion lattice in the chiral magnet MnSi reported here represents an example where an electronic liquid forms a spin crystal made from topologically nontrivial entities." [Mue09]. Skyrmions are stable topological, vortex like, magnetic structures [PR10]. Figure 1.1 shows the magnetic phase diagram for MnSi, developed by Mühlbauer et al. In further

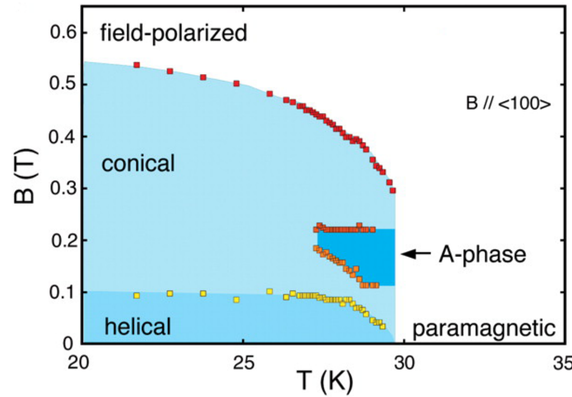

Figure 1.1: Magnetic phase diagram of MnSi. With no external magnetic field the helimagnetic order appears below $T_C = 29.5\,K$. In the conical phase the helical order is aligned along the external field. In small magnetic fields, below T_C the skyrmion lattice stabilizes (A-phase). Figure taken from [Mue09].

investigations, Jonietz et al. observed spin transfer torques in the skyrmion lattice phase of MnSi, and they identify chiral magnets with non-trivial topological properties as an ideal system to enhance the general understanding of spin transfer torques [Jon10].

Apart from fundamental research, MnSi has good prospects to be a valuable material for applied physics. In the field of spin electronics ("spintronics"), the injection of spin-polarized currents from a metal into a semiconductor is a key technological process. The first achievements in this field were made by Ohno et al. and Fiederling et al. in 1999 [Ohn99; Fie99]. Both groups used gallium-arsenide as substrate material. On silicon the problem is that most ferromagnetic metals, such as cobalt or ion, form non-magnetic silicides on the silicon surface. The randomly oriented magnetic moments of the silicide layer cause low spin injection into the silicon. Recently, Huang et al. avoided this problem by separating the ferromagnetic metal and the silicon surface [Hua07]. However, MnSi has the prospect to form an epitaxial, magnetic layer on silicon that can be used for spin injection. In a density functional theory study from Hortamani et al. it was shown that MnSi has large magnetic moments at the Mn atom near the surface and interface [HKS07]. Furthermore, the spin polarization at the Fermi level is predicted to be $\sim$50% for thin films of MnSi [ZL11]. All these properties make MnSi a highly interesting material for

silicon based spintronics, especially for the injection of spin-polarized currents into silicon.

In an additional study the growth, structure and properties of silicon suboxide are investigated. The transition layer from silicon (Si) to silicon dioxide (SiO_2) is called silicon suboxide (SiO_x) layer. Within this layer the silicon atoms have varying numbers of oxygen neighbors [DM00]. In the literature the SiO_x layer thickness varies between 3–10 Å[Hol87; Kei99]. Studying this transition layer is difficult not only because it is very thin but it is always covered by a SiO_2 layer. Several models for the Si/SiO_2 interface region exist that include the existence of a SiO_x layer [Fuo88; CF90]. They are based upon the assumption that the first layers of SiO_2 on Si are crystallographically ordered. The SiO_x layer, its structure, properties and formation are still controversial. Understanding the processes that lead to the formation of SiO_x could lead to a more complete understanding of the Si/SiO_2 interface and therefore could be beneficial to semiconductor technologies.

The field of thermoelectric research has increased in the last ten years, mostly driven by the need of the automobile industry to lower the carbon dioxide output by converting waste heat into electrical energy. The effectiveness of a thermoelectric material is expressed in the figure of merit ZT. Bulk thermoelectric materials were created over four decades ago. Their ZT ranges typically from 0.8 to 1.0 [Ban10]. At the end of the last century, nano-scale geometry was introduced to the field of thermoelectrics. The nano-structures are small enough to disrupt the mean free path of phonons; with that the thermal conductivity is lowered and the ZT increased. Venkatasubramanian et al. reported in 2001 a $ZT > 2$ using a superlattice of Bi_2Te_3/Sb_2Te_3 [Ven01]. In the following years even higher values of ZT were reported for nano-structured materials [Har05]. Most of these high ZT materials have the disadvantage that they operate only at rather low temperatures ($<400°C$), because they are not stable at high temperatures. Here, silicon comes into play. SiGe alloys have been used as thermoelectric material in space flight, to power space probes that too far from the sun to use solar cells. But the low ZT of SiGe alloys ($0.5<ZT<0.9$) has rendered them uninteresting for wide industrial application, because other materials, such as BiTe or Heusler compounds, have $ZT>1.0$. But with nano-structured silicon, silicon suboxide and silicon-germanium layers the high temperature range could be opened to thermoelectric materials with high ZT.

Chapter 2 of this thesis introduces the material systems studied. Chapter 3 describes the molecular beam apparatus and the measurement techniques used for analysis. Chapter 4 concerns the growth method for MnSi on Si and the identification of the grown silicide phase. The last chapter, Chapter 5, deals with the possibility of growing silicon suboxide layers and overgrowing them with single crystalline silicon. By repeating the suboxide layer, a superlattice is created and the properties are analyzed.

Chapter 2

Silicon Based Material Systems

This chapter presents an overview of the theoretical foundations and material properties needed for the comprehension of the techniques, analysis and results. This work concerns silicon-based epitaxy—more precisely molecular beam epitaxy of silicon and silicon-based materials. Silicon is used as substrate and is an important constituent of all structures produced and measured. Because the topic of epitaxy is a very extensive one, only especially important issues are addressed. For wider and detailed literature on the subjects the references given in this chapter provide ample information on epitaxy in general, silicon, silicon oxide and silicides.

2.1 Silicon Epitaxy

Silicon is an elemental semiconductor crystallizing in diamond structure, which belongs to the space group $Fd\overline{3}m$. The diamond structure has a face centered cubic (fcc) lattice with a two atomic basis ((0,0,0),($\frac{1}{4}$,$\frac{1}{4}$,$\frac{1}{4}$,)) and a lattice constant of $a_{Si} = 5.43102\,\text{Å}$. Silicon forms covalent bonds, as is common for the group four elements, with an angle of 109.5° between the bonds. Bonding in the silicon lattice is very strong, but silicon is not a closed packed lattice: only about 34% of the volume is occupied [Kit05]. For a detailed review on the state of the art of the properties of silicon, see Robert Hull: *Crystalline Silicon* [HI99].

Heteroepitaxy refers to the deposition of a mono-crystalline layer on a substrate, where the orientation of layer and substrate are identical. In heteroepitaxy the layer has a different lattice constant than the substrate. When the layer starts to grow, it grows pseudomorph, meaning that it adopts the lateral lattice constant from the substrate. In order to compensate for the new, forced lateral lattice constant, the unit cell of the layer is stretched or compressed vertically, because the lateral and vertical lattice constants are linked by the Poisson ratio (ν). Figure 2.1 illustrates the pseudomorph layer growth on a substrate. Here, the intrinsic layer lattice constant is larger than the substrate lattice constant; this results in compressive strain on the layer and therefore the vertical lattice

constant is enlarged. With increasing layer thickness, the energy stored in the elastic strain increases until it is large enough to relax the strain by means of lattice faults. The larger the difference between the two lattice constants, the lower is the maximum pseudomorph layer thickness that can be deposited [JHC97].

The difference of the lattice constants of two lattices is called misfit (f_m) and can be calculated by the following equation:

$$f_m = \frac{a_{layer,intrinsic} - a_{substrate}}{a_{substrate}} \tag{2.1}$$

with $a_{layer,intrinsic}$ as the intrinsic lattice constant of the layer and $a_{substrate}$ as the substrate layer constant. The biaxial strain of an epitaxial layer ε is calculated from the difference of the actual lateral lattice constant of the layer ($a_{\parallel}$) and the intrinsic lattice constant ($a_{layer,intrinsic}$), divided by the lattice constant of the substrate ($a_{substrate}$).

$$\varepsilon = \frac{a_{\parallel} - a_{layer,intrinsic}}{a_{substrate}} \tag{2.2}$$

As long as the layer grows pseudomorph, the strain ε is equal to $-f_m$.

If the substrate lattice constant is larger than that of the layer, the misfit f_m is negative and the strain dilates the lateral lattice constant of the layer (tensile strain). If the substrate lattice constant is smaller than that of the layer, the lateral lattice constant of the layer is compressed (compressive strain). The vertical lattice constant of the layer accommodates for the dilation or compression that is forced by the substrate. The magnitude of the change in vertical lattice constant is related to the Poisson ratio (ν), which depends on the elastic constants of the crystal. This means that the Poisson ratio expresses the

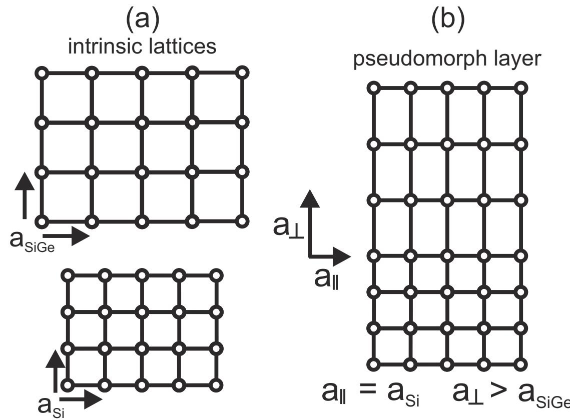

Figure 2.1: Illustration of the strain resulting from pseudomorph layer growth. In (a) both lattices are shown with their intrinsic lattice constants. The strain resulting from pseudomorph growth is shown in (b).

quantitative correlation for uniaxial strain of the lateral and vertical lattice constant of the layer. The lateral layer dilation ($\varepsilon_{\|}$) depends on the difference of $a_{substrate}$ and the actual lateral layer lattice constant divided by the intrinsic layer lattice constant. The vertical dilation ($\varepsilon_{\perp}$) depends on the parallel layer dilation and the Poisson ratio of the crystal.

$$\varepsilon_{\|} = \frac{a_{substrate} - a_{\|,layer}}{a_{layer,intrinsic}} \tag{2.3}$$

$$\varepsilon_{\perp} = \frac{-2\nu}{1-\nu}\varepsilon_{\|} \tag{2.4}$$

2.2 Manganese Silicide

Manganese silicides are a class of materials with different stoichiometry of manganese and silicon. The silicides can be split into three classes; the manganese rich silicide Mn_5Si_3, the stoichiometric mono-manganese silicide MnSi, and the higher manganese silicides (HMS), which consist of several compounds with a stoichiometry of approximately $MnSi_{\sim 1.7}$. In this work, the terms silicide and manganese silicide refer to mono-manganese silicide unless otherwise indicated.

MnSi single-crystals have been realized since the 1970's with bulk growth methods, such as the Czochralski growth process. MnSi crystallizes in a cubic B20 structure belonging to the space group $P2_13$, which is non-centro-symmetric and includes chirality, meaning a right-handed and left-handed form of the crystal. The lattice constant is $a_{MnSi} = 4.560$ Å and the unit cell contains four Mn atoms and four Si atoms, as depicted in Figure 2.2(a). The positions are given by $(u,u,u), (\frac{1}{2}+u, \frac{1}{2}-u, -u), (-u, \frac{1}{2}+u, \frac{1}{2}-u), (\frac{1}{2}-u, -u, \frac{1}{2}+u)$ with $u_{Mn} = 0.138$ for manganese and $u_{Si} = 0.846$ for silicon positions [Bor33]. These positions represent the crystal in its right-handed form. For the left-handed form, the positions are $(u,u,u), (\frac{1}{2}-u, \frac{1}{2}+u, -u), (\frac{1}{2}+u, -u, \frac{1}{2}-u), (-u, \frac{1}{2}-u, \frac{1}{2}+u)$ [Ish85]. A mirror operation with respect to a $(1\bar{1}0)$ plane transforms one chirality into the other [Ish85].

Generally, epitaxial growth of MnSi can be achieved on Si(100) and Si(111), but Hortamani et al. have shown by means of density-functional studies that growth on Si(111) is easier to realize, and in addition has the advantage that film growth is energetically favored over island growth [HKS07]. One of the reasons why Si(111) is well suited is the rather small lattice mismatch on the Si(111) surface, although the mismatch of the cubic unit cells of both materials is -16.0 %. The MnSi(111)-1×1 surface lattice can be nearly matched to the $(\sqrt{3}\times\sqrt{3})$R30° lattice of the Si(111) surface [ZL11]. In Figure 2.2(b) the 30° rotation of the surfaces is visible and the Si surface unit cell is depicted in green. The Si(111) surface has a six-fold symmetry and the position of least lattice misfit can be achieved by 30° clockwise or anti-clockwise rotation of the MnSi crystal structure. The lattice mismatch

between the Si(111) surface unit cell and the MnSi(111)-1×1 surface unit cell can be calculated following equation 2.1 and the following (111)-surface lattice constants:

$$a_{Si(111)} = 2 \cdot \frac{a_{Si}}{\sqrt{2}} \cdot \cos(30°) \quad (2.5)$$

$$a_{MnSi(111)} = \sqrt{2} \cdot a_{MnSi} \quad (2.6)$$

The resulting mismatch is $f_m = -3.0\,\%$ for the surface unit cells.

With selected area electron diffraction Zhang et al. have found the crystallographic orientation to be Si(111)‖MnSi(111) and $[\bar{1}01]_{\mathrm{MnSi}} \parallel [\bar{1}2\bar{1}]_{\mathrm{Si}}$ [Zha02], shown in Figure 2.2(b). The stacking order of MnSi in [111] direction consists of three quadruple layers with the stacking sequence ABCABC... [HKS07]. A single quadruple layer consists of a sparse Mn layer, a sparse Si layer, a dense Mn layer, and a dense Si layer [HKT09]. The dense layers have three atoms per 1×1 unit cell, the sparse layers have one [HKS07]. The stacking order is shown in Figure 2.2(c).

2.2.1 MnSi Thin Film Growth on Si(111)

The most common growth method for MnSi thin films to date, is deposition of Mn on a Si(111)-7×7 reconstructed surface at room temperature, with subsequent annealing at elevated temperatures. Deposition of less than 4 ML of Mn at room temperature results in islands of Mn on a bare Si surface [Shi97]. When the samples are annealed surface reconstructions are formed, the Mn islands exhibit a $\sqrt{3} \times \sqrt{3}$ reconstruction, whereas the Si exhibits the stable 7×7 reconstruction. Coverages above 4 ML lead to almost completely covered surfaces [EGN96]. Different growth parameters and influence of surfactants, such as silver or bismuth, have been studied by several groups [Nag99; Shi97; Cti02].

Zou et al. describe the MnSi formation when a deposited Mn layer is annealed at temperatures between room temperature and 300°C. The amorphous Mn layer starts reacting with the Si surface, forming MnSi islands, at defects such as pits and edges. After MnSi has nucleated, more Mn and Si attach to the nucleus and the MnSi islands grow in lateral direction. The reaction begins at room temperature, but is only completed at elevated temperatures. In addition, Zou et al. observe a dependence of the lateral growth on the annealing temperature [ZL11].

Layers produced with this solid phase process exhibit a homogeneous crystallization front. The layers are predominantly flat except for some holes and craters. The origin of those has been investigated by Higashi et al. They found that the Si necessary for the MnSi formation is supplied from the Si substrate, thereby creating the holes and craters. Additional supply of Si, from a Si source, during the Mn deposition, referred to as co-deposition, reduces the amount of holes and craters, thus creating a smoother surface [HKT09]. Furthermore, Zou et al. state that the holes and craters can be caused by the diffusion of Si from the

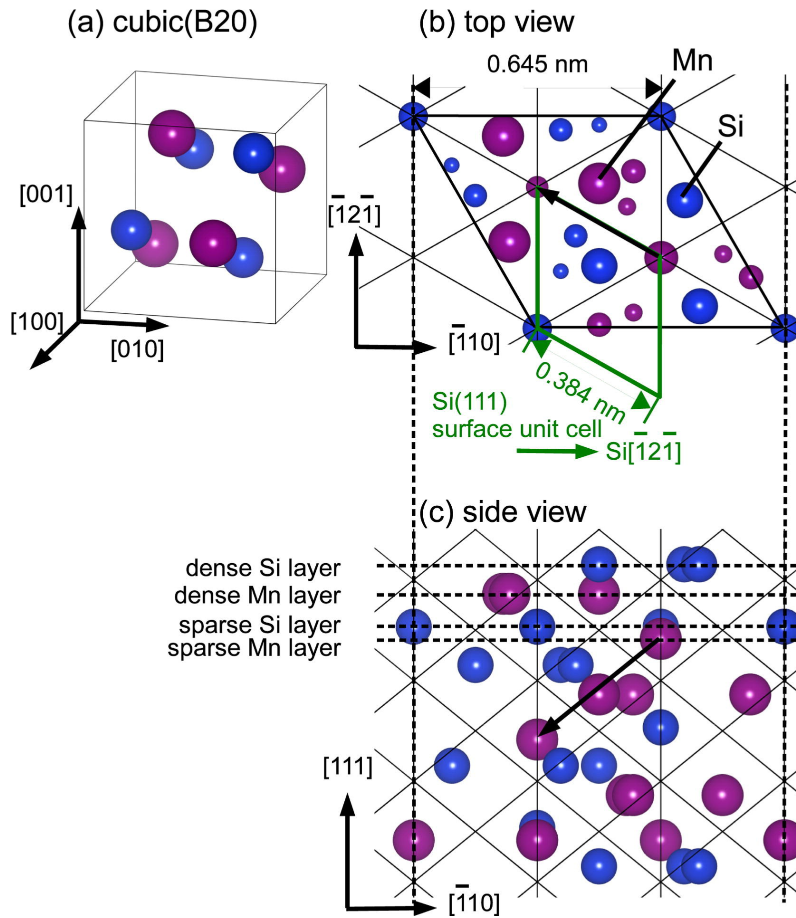

Figure 2.2: (a) Model of the MnSi cubic unit cell in the right-handed form. Mn atoms are purple and Si atoms blue. (b) Top view of the MnSi(111) surface with the Si surface unit cell depicted in green. The 30° rotation between both crystals is visible. (c) Side view of MnSi(111) with the stacking order of the sparse and dense layers visible. The arrow in (b) and (c) is the primitive translation vector of MnSi. Figure taken from Suto et al. [Sut09].

substrate to supply for the MnSi layer. Fractal-like growth or strain relief are further possibilities for the cause of the holes and craters [ZL11].

The growth mode and formation of MnSi is controversial. It is suggested that MnSi grows quadruple layer after quadruple layer. But conclusive data on the interfacial reaction of Mn and Si and the growth mechanism of MnSi are not yet available [ZL11].

Thicker films of MnSi have the additional problem of strain relief. Kumar et al. observe a hexagonal pattern with STM, which they identify as a long range dislocation network, caused by the strain [Kum04]. Ex-situ AFM measurements of Suto et al. show protrusions on the MnSi surface that might form to reduce the surface energy. These protrusions act

as pinning sites for steps of MnSi [Sut09]. Nonetheless, Hortamani et al. calculated that a Si cap layer stabilizes all types of MnSi films [HKS07].

2.2.2 Properties of MnSi

MnSi is a weak itinerant-electron magnet with a helical spin structure [SP11]. The ordered magnetic phase has been found, by Wernick et al. in 1972, below 30K [WWS72]. In 1976, Ishikawa et al. found the helical spin structure along the [111] direction. The period of the spin structure was determined to 18 nm [Ish76]. The lack of inversion symmetry allows the helical magnetic structure in MnSi. The relation between the structural chirality and the magnetic chirality is not yet completely understood [Ish85; Tan85].

Together with Mn_5Si_3, MnSi is the only known manganese silicide which is metallic in nature [Kum04]. Band structure calculations predict that the paramagnetic phase of MnSi has a band gap of ∼0.6 eV above the Fermi level, and the ferromagnetic phase spin polarized minority bands only ∼150 meV above the Fermi energy [JP04]. Unfortunately, not much literature exists on transport and magneto-transport properties of MnSi, especially thin films. The existing articles explain only small parts of the properties [Neu09], but the full picture is still missing.

2.3 Silicon Suboxide

Silicon suboxide (SiO_x) is a form of silicon oxide between the limits $x = 0$ and $x = 2$. Where $x = 0$ represents silicon, $x = 2$ silicon (di-)oxide and $x = 1$ silicon monoxide. Silicon suboxide is not an independently stable material but rather an anomaly of SiO_2 encountered on the interface between silicon and silicon oxide. In the 1970s, investigations on SiO_x had already been performed and the first models developed [Phi71]. However, it was only after the semiconductor industry came into existence and made silicon their most important material, accompanied by silicon dioxide as a matching insulator, that researchers began to focus on the Si/SiO_2 interface. With the shrinking of the structure sizes of semiconductor devices, it became more and more important to investigate the microstructure of the Si/SiO_2 interfaces, because almost nothing was known about the microstructure of the interface. For instance, what is the nature of the transition from crystalline silicon to amorphous silicon oxide, is there strain at the interface, is the interface stable at high temperatures or what happens with the band structure near the interface? Some of these questions have been answered in the past but some are still open and heavily discussed.

2.3.1 Theoretical Models

For the description of silicon suboxides, two basic models exist: the random mixture model (RMM) and the random bond model (RBM). Both have been around since the 1970s, but they represent very different opinions on the nature of non-stoichiometric silicon oxides. The following prerequisites proposed by Temkin [Tem75] form the basis for both:

- every Si atom is bound to four atoms
- every O atom is bound to two atoms
- O atoms do not bond with each other
- average bond angle for O is 144°
- average bond angle for Si is the tetrahedron angle 109.5°
- average Si–O bond length is 1.62Å
- average Si–Si bond length is 2.35Å

From these prerequisites, five possible bonding configurations for a central Si atom can be deduced. In silicon the central Si atom is surrounded by another four Si atoms. Replacing one or more of the surrounding Si atoms by O leads to different bonding configurations, until finally the central Si atom is surrounded by four oxygen atoms; this corresponds to SiO_2. All possibilities are depicted in Figure 2.3.

The most important difference between the two models is that, in the RMM, only $Si–Si_4$ and $Si–O_4$ configurations are allowed. Therefore SiO consists of a mixture of Si and SiO_2 with a ratio of 1:1. A suboxide SiO_x consists, according to this model, of $1 - \frac{x}{2}$ parts of Si and $\frac{x}{2}$ parts of SiO_2. In Figure 2.4b the probabilities of the occurrence of the bonding configurations is plotted against the stoichiometric parameter x.

The RBM, on the other hand, is based on a statistical distribution of all five bonding configurations for a given stoichiometric parameter x. The occurrence probabilities of this model are plotted in Figure 2.4a. It is obvious that the occurrence probabilities of $Si–Si_4$ and $Si–O_4$ for suboxides are notably smaller compared with the RMM. However, suboxides with $0.5 < x < 1.5$ consist of all five bonding configurations. Both models represent very extreme points of view, but they show how different the opinions were on the nature of the Si/SiO_2 interface, and still are. A compromise between both models could be that the RMM is complemented with the RBM for all interfaces between Si and SiO_2 regions.

2.3.2 Growth Processes at the Si/SiO_2 interface

Adsorption

On the way to growing oxide structures under MBE conditions, the first step is the adsorption of oxygen on the silicon surface. Several groups have investigated the adsorption

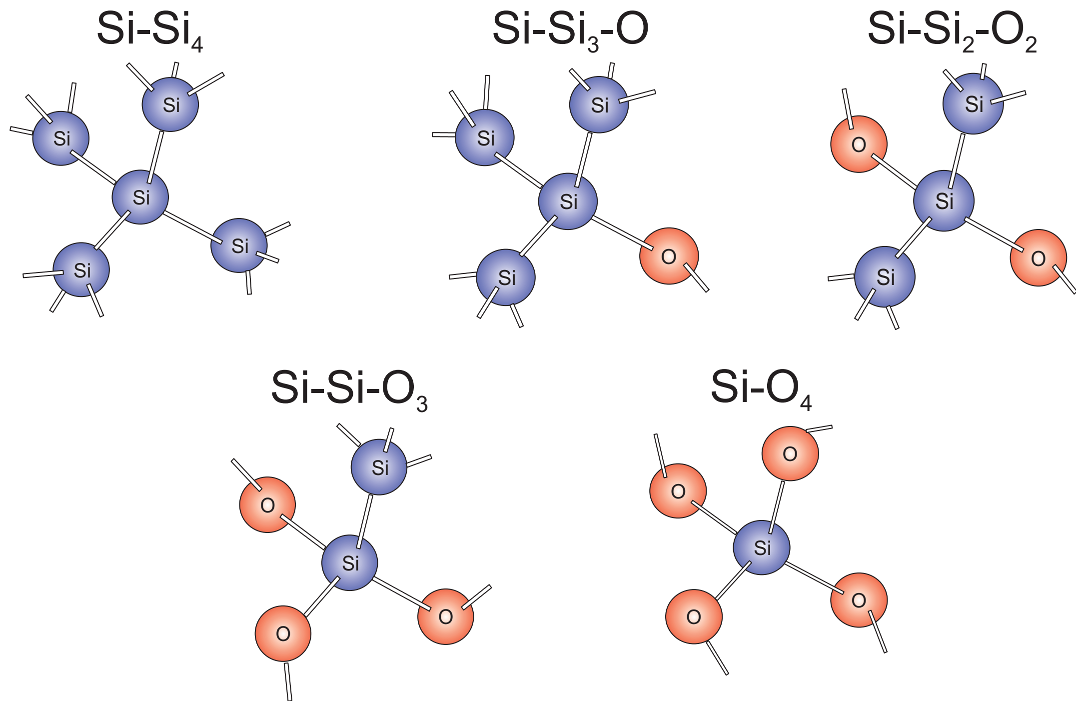

Figure 2.3: Possible bonding configurations for a Si atom in the random bond model. In all five configurations the central Si atom is bound in a tetrahedron. Adopted from [Kah01].

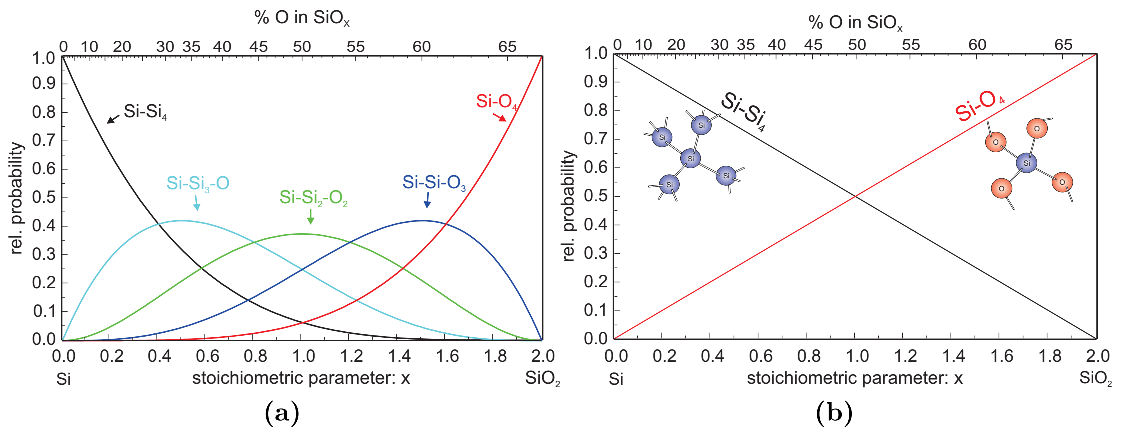

Figure 2.4: Composition of SiO_x according to the RBM (a) and the RMM (b). In both figures the relative probability P_i is plotted against the stoichiometric parameter x. The relative probability refers to the different bonding configurations from Figure 2.3. Figures adopted from [Kah01]

of oxygen on the silicon surface, and almost all agree that the initially adsorbed atoms are not distributed uniformly on the surface. Moreover, the nucleation sites enhance the probability for subsequent adsorption on a neighboring site, thus creating clusters of adsorbed oxygen [ALB91].

Studies have shown that, on a Si surface, O_2 is adsorbed at first at an on-top site forming a Si–O, and then moves into a bridge site, between the Si dimers, forming Si–O–Si [Tok90]. This leads to opening up the surface, and more O_2 can penetrate and insert between Si–Si bonds in Si layers beneath the surface. Structural changes are forced by this insertion and surface stress occurs.

The sticking coefficient for molecular oxygen on the Si surface is temperature independent below 300°C. Above that, D'Evelyn [DNE87] reports an increase of the sticking coefficient with temperature. The sticking coefficient is of the order 10^{-2} under the conditions discussed in this work. Adsorption of O_2 on the Si surface can lead to the formation of ultrathin oxide films.

Formation of Ultrathin Oxide Films

Formation of stable SiO_2 is called passive oxidation, in contrast to active oxidation (see page 14). Ultrathin oxide films (5Å) have been studied by Himpsel et al. with x-ray photoelectron spectroscopy (XPS). The core level spectra have shown four separate, chemically-shifted peaks which can be assigned to Si atoms with different oxidation states (suboxide states), as described in section 2.3.1. This corresponds to Si atoms with 1–4 O atoms as neighbors [Him88]. The results are in agreement with studies of other groups that report the same findings [HH83; Gru87; HH84]. Measurements in correlation with the oxide layer thickness have shown these peaks to be independent of the oxide layer thickness. This indicates that the signals of Si in four oxidation states originates at the interface. Furthermore, Himpsel et al. have proved that the suboxide states are only present at the Si/SiO_2 interface and not at the SiO_2 /vacuum interface [Him88]. From the average energy shift of the XPS measurements, the average oxidation state can be determined in dependence on the oxygen coverage. For increasing oxygen coverage, the average oxidation states approaches Si^{+4}. Engstrom et al. have shown that for 600°C the average oxidation state of Si^{+4} is reached for a coverage of ∼5Å [EBE92].

The oxygen of thin oxide films occupies bridge bonds on the silicon surface for coverage up to 1 mono layer (ML) [Inc87]. The mismatch between SiO_2 and Si leads to tensile stress at the interface. Sander and Ibach have determined a linear correlation between this stress and the oxygen coverage, for coverage up to 1 ML [SI91]. Incorporation of O into the Si–Si bonds, in a bridging configuration between the first and second Si layer, can explain the stress.

Concerning the orientation of the oxide film, under special circumstances, the interface exhibits a clear ordering, as shown by Renaud et al. with gracing incident x-ray diffraction [Ren91]. In their studies they determined the interface thickness to be less than 5Å. Additionally, they determined a high level of positional and substitutional disorder, which made an analysis of the atomic positions impossible. Another gracing incident x-ray diffraction study of room temperature oxide films, from Rabedeau et al., found an ordered interface, but the signal originated from only about 10% of the surface [Rab91]. Therefore, an ordered interface is not commonly observed but can be prepared with special procedures.

Decomposition of SiO_2 films

The formation of oxide on silicon under vacuum conditions is accompanied by simultaneous thermal decomposition of SiO_2. Decomposition and the following desorption is caused by disproportionation of SiO_2 into SiO by the reaction:

$$\mathrm{SiO_2} + \mathrm{Si} \rightarrow 2\mathrm{SiO}.$$

Decomposition of SiO_2 depends not only on the temperature but also on the oxygen coverage. At a higher coverage, a higher temperature is needed for the decomposition of SiO_2. On the surface the decomposition creates circular voids in the oxide film [LLR87; Rub90]. Further decomposition takes place at the void perimeter, while the remaining oxide film thickness is not thinned. In the center of the voids, a clean Si 2×1 surface can be observed [SBE91]. The mechanics of decomposition by void formation are operative for 0.27 ML to 10 ML of oxygen coverage, as observed by Sun et al. [SBE91]. Further studies by Johnson et al. have shown the voids to be randomly distributed throughout the oxide film [JE92]. The depth of the voids can be up to several Si layers deep, although only 1 ML of oxygen is desorbed. Therefore, the thermal decomposition of oxide layers and desorption of SiO causes substantial roughening of the surface.

Processes at High-Temperatures

At higher temperatures exposure of a Si surface to O_2 leads to the formation of SiO. Because SiO is volatile and therefore removes material, this process is called etching or active oxidation. For temperatures above 600°C, and low O_2 pressure, SiO is formed at the surface. The kinetics and mechanism of this process have been studied, and D'Evelyn et al. have described the kinetics as a two-step sequential mechanism [DNE87]:

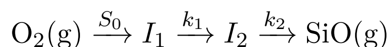

$$\mathrm{O_2(g)} \xrightarrow{S_0} I_1 \xrightarrow{k_1} I_2 \xrightarrow{k_2} \mathrm{SiO(g)}$$

Here, S_0 is the sticking coefficient, k_1 and k_2 are rate-constants and I_1 and I_2 are reaction intermediates. The desorption of the SiO from the surface roughens the surface; for long exposures to O_2 at higher temperatures, the Si surface is roughened on micron scale [Ohk92].

Oxidation Phase Diagram

The active and passive oxidation processes have been shown to depend on temperature and oxygen pressure. Combining the studies above, with several others, a phase diagram for the oxidation of a Si surface can be created. An example is shown in Figure 2.5. Various phase diagrams exist in the literature. Depending on the data sources used and the interpretation of the authors, the transition region varies in extension a little, but the general conclusions are the same. At low temperatures and high oxygen pressure, SiO_2 is formed at the surface (passive oxidation regime). At high temperatures and low oxygen pressure active oxidation (etching) occurs at the surface, the oxidation causing SiO desorption decreases with increasing SiO_2 coverage of the surface. But the bare Si parts of the surface continue to be etched, and thus keep parts of the surface oxide free. The transition from the active regime to the passive regime is driven by the increase of thermal stability with local oxygen coverage [Eng93]. If islands with higher oxygen coverage can form locally, they are resistant to thermal decomposition and grow continuously [DNE87].

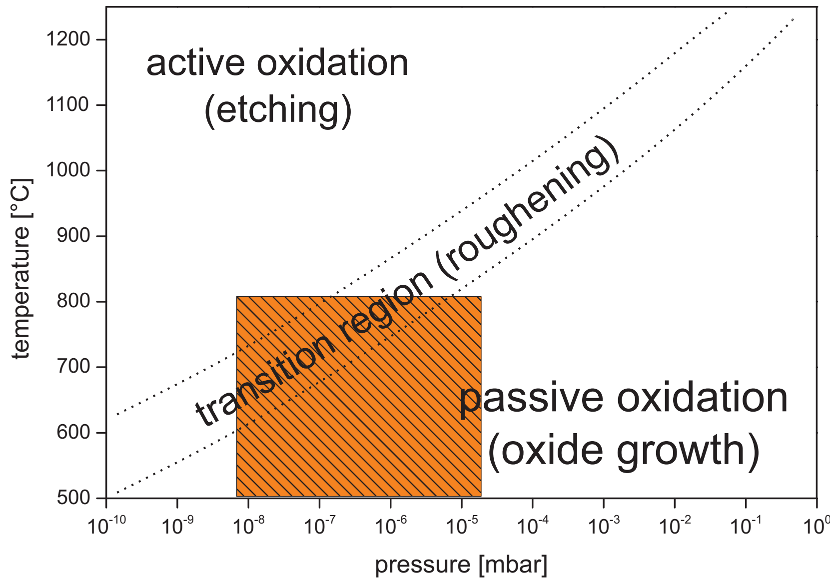

Figure 2.5: Silicon surface oxidation regimes depending on oxygen pressure and substrate temperature, based on graphic from [DM00]. The marked region represents the part of the phase diagram used in this work.

With data from diverse studies a model has been developed to describe the rate of the active and passive regime. From that it can be evaluated that the processes of the active and passive oxidation have the same rate (for low O_2 coverage) at about 700°C [Eng91].

In the early stages of oxide growth the oxide formation is non-uniform in both regimes. In the transition region, both the active and passive oxidation are competing with each other, causing highly uniform oxide formation with very strong surface roughening. According to Seiple et al. and Smith et al. the roughening is caused by the nucleation of oxide clusters, while the clean Si surface is etched down [SP95; SG82].

2.3.3 Properties of SiO_x

Only a few studies focus on the properties of the suboxide layer at the interface. Therefore little is known about the suboxide layer itself, such as strain, electrical properties or long range order. The structure of the suboxide layer is still a controversial matter for discussion. Ourmazd et al. propose a 5Å, totally ordered tridymite structure, with huge strain, as a transition from c-Si to a-SiO_2 [Our87]. Rochet et al. detect no short range order and propose an "O-decorated dimerized interface model" for the suboxide layer at the interface of Si/SiO_2 [Roc97]. Groups using simulations to determine the SiO_x structure offer even more possibilities for the SiO_x structure. A study by Tu et al. uses Monte Carlo simulations and proposes an ordered Si/SiO_2 interface based on Si–O–Si bridge bonds, with approximately 1-2 ML of Si atoms with oxidation states other than Si^{+4} [TT00]. In other studies, simulations are used to determine the electrical properties of the suboxide layer. In investigations by Kaneta et al. (by first principle calculations) on structure and electronic properties of the Si/SiO_2 interface, purely crystallite SiO_2 models were used. They reported the large change of the band structure between Si and SiO_2 in the region between 1-4 Å of the interface [Kan99]. Kang et al. found, by means of first principle calculations, that roughness or defects have only little influence on the tunneling through a SiO_2 layer. But a network of O vacancies composed of Si–Si bonds increases the tunneling current drastically [Kan08]. These studies present results which could also be applicable to SiO_x layer. Because of the numerous presumptions made in these studies, the results can not be generalized.

Chapter 3

Experimental Techniques

In this chapter the sample preparation and procedures to calibrate the growth process are described. Mode of operation of the MBE and the MBE setup are explained in considerable detail. A description of the analysis techniques that are used to characterize the MBE samples is given. The challenges that the methods pose with respect to thin film analysis will be discussed.

3.1 Sample Preparation

Silicon wafers, (100) and (111), are used as substrates for the sample preparation in the Si MBE. The wafers are boron-doped, with either low (<0.02 Ωcm) or high (>8000 Ωcm) resistivity. Oxide removal is realized either by a thermal de-oxidation step before growth or a wet chemical process. The latter proved more reliable with respect to reproducibility. Some wafers that were thermally de-oxidized (T_{sub}= 970°C for 15 minutes) revealed a gray-blue surface—sometimes over the complete wafer, sometimes only the outside part. Analysis confirms that the oxide layer has not been completely removed. Wet etching the wafers before growth resolves this problem. The following process is used to remove the oxide and passivate the surface against re-oxidization. Wafers are dipped in 50% hydrofluoric acid (HF) for 30 seconds and rinsed in de-ionized water. This step is repeated and a final 30 second dip in HF is carried out to create a hydrogen passivated surface [Cha89] that is loaded immediately into the vacuum chamber.

3.2 Molecular Beam Epitaxy

Molecular beam epitaxy (MBE) is a technique to grow single crystals. Several other techniques exist to produce single crystal materials: chemical vapor deposition (CVD), ultra high vacuum CVD, rapid thermal CVD, plasma enhanced CVD, metal organic CVD or liquid phase epitaxy (LPE). Invented in the late 1960s [Cho70], MBE has been

developed to become a highly sophisticated method for manufacturing semiconductor devices [Cho99]. In contrast to the afore mentioned methods, MBE does not need any chemical processes.

3.2.1 Technology and Set-Up of MBE

The laboratory and the silicon MBE have been completely rebuilt for this project. Figure 3.1 shows a sketch of the ultra-high vacuum (UHV) system and MBE chamber. The SiGe MBE is not part of the MBE-UHV cluster of the Experimentelle Physik III, because the SiGe MBE is a three inch wafer chamber and transport through the UHV system that is built for two inch wafer is not possible.

Ultra high vacuum[1] is absolutely necessary for MBE to allow the atoms or molecules from the evaporation sources to reach the substrate without interaction with any residual gas, and to prevent the deposition of contaminants on to the substrate. This condition is met when the mean free path is much larger than the distance source to substrate. The mean free path λ_{mfp} is given by:

$$\lambda_{mfp} = \frac{k_B T}{\sqrt{2}\pi d^2 p} \tag{3.1}$$

Where k_B is the Boltzmann constant, T is the temperature, p is pressure and d is the diameter of the gas particles. For ultra-high vacuum λ_{mfp} is in the order of kilometers. High vacuum conditions [2] would already suffice for the molecules to reach their target undisturbed, but the recoverage time (time until a clean surface is covered by a mono-atomic layer) in high vacuum is only in the order of seconds. High defect density and unintended doping levels would be the consequence. Under ultra-high vacuum conditions the recoverage time increases to the order of days. This enables crystal growth of high purity materials.

To achieve the desired pressure level the MBE is equipped with a cryo pump, turbomolecular pump, Ti sublimation pump and a liquid nitrogen (LN_2) cooling shroud. This pump setup enables a background pressure lower than 3×10^{-11} mbar. In the transfer system, an ion pump with integrated Ti sublimation pump provides the UHV (lower than 6×10^{-11} mbar). Heating station and load lock are pumped with a turbomolecular pump. Heating of the samples is necessary due to a water film caused by water vapor in the air.

In order to have a precise and reproducible growth process, the MBE is controlled by a computer running specially designed software (Shiva 4.5). General parameters for the MBE system, as well as the parameters for the process about to run, are loaded into the

1 ultra high vacuum: 10^{-7} mBar $< p < 10^{-12}$ mbar
2 high vacuum: 10^{-3} mbar $< p < 10^{-7}$ mbar

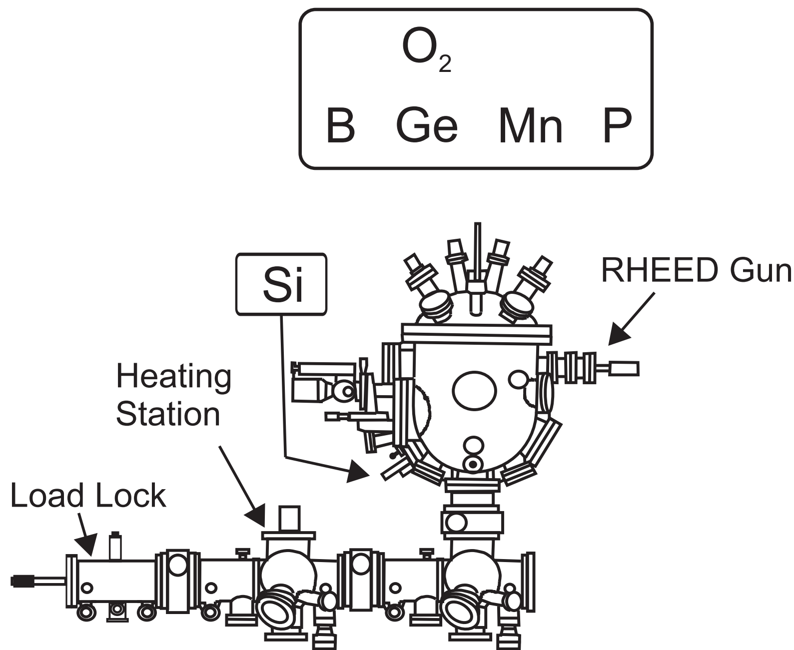

Figure 3.1: Si MBE laboratory consisting of the MBE chamber equipped with Si in an electron beam evaporator and Ge, Mn and B in Knudsen-type effusion cells. The P cell is a sublimation source cell type (SUSI) and O_2 is provided through a leak valve.

program and checked for incoherencies. Thus, the computer is able to identify dangerous program steps and can prevent damage to the components.

The molecular beams can be interrupted with shutters that are mounted in front of the effusion cells, thus enabling abrupt changes of the material composition. For the oxygen gas source a shutter is not necessary because the leak valve functions as a shutter.

Over the course of this work, the setup of the leak valve has been changed to improve the performance. The original setup consisted of a Riber plasma source mounted at a cell port with a manually operated leak valve at the inlet flange and a Linde MiniCan (purity 4.5N) for oxygen supply. Linde MiniCan vessels have a very small volume (1 l) a low pressure (12 bar) and no level indicator. The disadvantage of a manually-operated valve is the time it takes to open and close, and thereby the low reproducibility. The plasma source and manual valve were dismantled and a pneumatic leak valve from VSE Vacuum Technology was installed. The opening and closing time of this valve is less than one second; hence the reproducibility is significantly improved. Oxygen supply has been changed to a 10 l/200 bar tank from Air Liquide with a purity of 5.5 N. To reduce the tank pressure to an acceptable level for the leak valve, a Linde reducing regulator for oxygen is used.

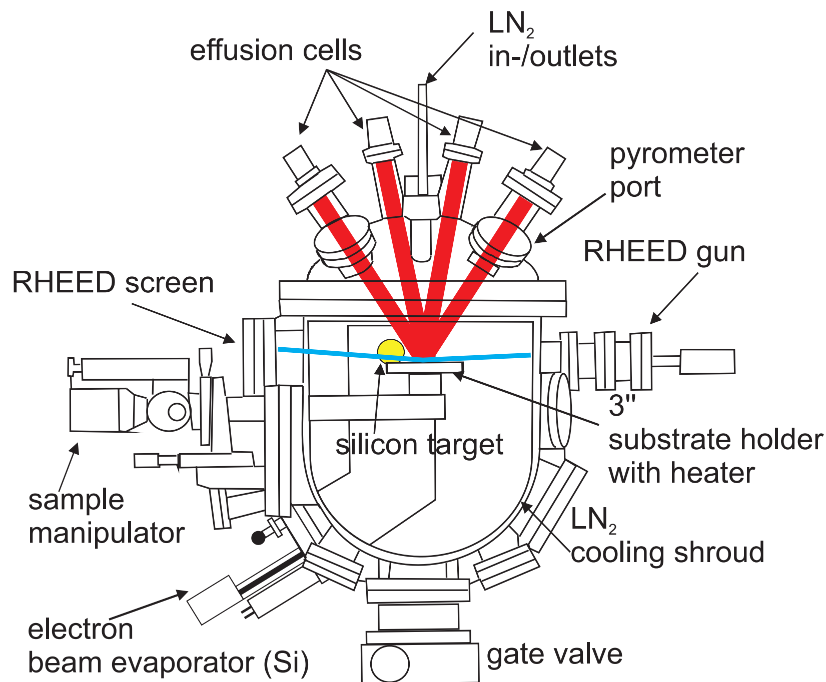

Figure 3.2: Detailed drawing of the SiGe MBE (top view of horizontal cross section). The electron beam evaporator built into the Riber 32 design creates a challenge for the optimum growth position.

Figure 3.2 presents a detailed top view of the MBE chamber. The original layout from Riber for this chamber includes only effusion cells as sources. Including an electron beam evaporator (EBE) as Si source is only possible from the bottom of the MBE reactor. The drawback of this geometry is an unfavorable growth position that is a compromise between the optimum for the effusion cells and the optimum for the EBE. In addition, the position has to be chosen in a way that the reflection high energy electron diffraction (RHEED) can be used. Figure 3.3 displays the problem of the growth position. The original position (the black substrate holder) presents only a small effective surface of the wafer towards the EBE. This would result in very low growth rates and inhomogeneous layers. Rotating the substrate holder down improves the performance of the EBE but simultaneously decreases the performance of the effusion cells, especially of the upper row of cells. Thus all effusion cells are mounted on the lower row. Only the oxygen gas inlet is mounted on the top row, because for a gas source the difference in the angle is negligible.

After the preparation of the wafer, described in section 3.1, the wafers are loaded into the load lock. To remove the water vapor film due to exposure to air, the samples are heated on the heating station. Wafers without wet chemical preparation are heated to 400°C for 75 minutes. Hydrogen-passivated wafers are heated to 150°C for 20 minutes in order to

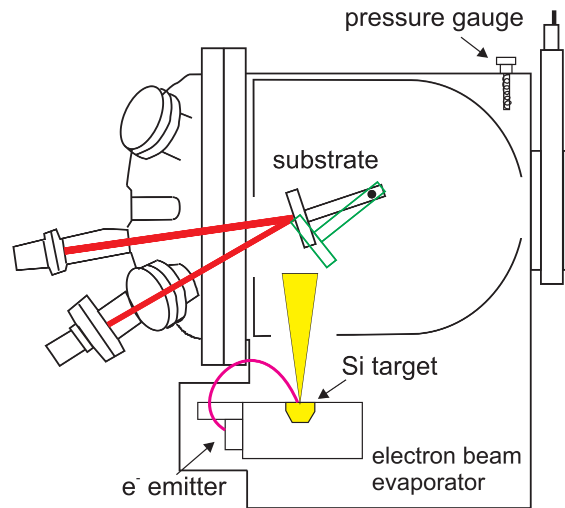

Figure 3.3: The problem of the growth position is illustrated. Optimum positions for effusion cells and EBE have a large difference in the phi rotation axis. The position indicated by the green substrate holder represents the compromise for the growth position.

preserve the H-passivated surface.

For MBE growth the substrate temperature plays a key role. The substrate holder is equipped with a tantalum heater sandwiched by PBN discs to provide homogeneous heat distribution. Temperature is controlled with a feedback control system which detects the actual temperature with a thermocouple in the vacuum system. Unfortunately, for technical reasons, the thermocouple is placed behind the substrate heater, away from the substrate. This causes an offset between the measured temperature and the actual wafer temperature. The measurements can not be used to determine the absolute temperature during growth, but the system is sufficient to control the growth parameter, as these are usually relative values.

Electron Beam Evaporator

As already mentioned, the Si molecular beam is provided by an electron beam evaporator. An EBE is not a typical source for MBE and has special requirements. The flux from an EBE is usually not only nonlinear but also a non-reproducible function of the control parameter, power [GDB87]. In order to provide a constant flux, the EBE needs a feedback loop that measures the actual molecular flux. In standard metallization systems that use EBE the deposited layer thickness is measured with an oscillating crystals. These need to be close to the source and, because of the high temperatures of the source, water cooling is necessary. Usually these are reliable systems but the close proximity to the LN_2 shroud bears the risk of bursting cooling lines if the water flow is interrupted. Unfortunately the

Si MBE suffered such an accident. It has been cleaned and reconstructed but without an oscillating crystal. The information of the flux for the feedback loop is now solely provided by the electron impact emission spectroscopy (EIES) sensor [GDB87]. In this sensor, electrons with 180 eV ionize the atoms from the Si beam. Through a filter, a photomultiplier detects the light emitted from the atoms. The intensity measured by the photomultiplier is proportional to the flux of Si atoms. A sample with thickness determined with XRD is used to calibrate the signal. This method of flux control enables a high reproducibility of growth rate and thus of layer thickness and composition of alloy layers.

Calibration of Growth

Calibrating the flux rate is performed on SiGe alloy layers of 50 nm up to 100 nm thickness. A low Ge content is used to prevent strain relaxation. Thickness and Ge content is measured with HRXRD (see section 3.4.1) and from that result conclusions about the Si flux and Ge flux are made. To measure the deposition rate of materials that do not crystallize in a cubic structure a different method is adopted. The material (in this case manganese) is deposited in amorphous form on a Si wafer and the thickness is determined by XRR (see section 3.4.2). From that result the beam flux density in molecules per unit area and second can be calculated with the formula:

$$\text{flux density} = \frac{d_{layer} \cdot \rho \cdot N_A}{u \cdot t_{layer}} \left[\frac{1}{\text{cm}^2 \cdot \text{s}}\right] . \tag{3.2}$$

Here d_{layer} is the layer thickness, t_{layer} the growth time, N_A the Avogadro constant, ρ the density in gram per cm^3 and u the atomic weight of the material in gram per mole. The formula can be used to calculate the flux density of all sources. For effusion cells the evaporation temperature is linked to the evaporation rate by an Arrhenius relation of the form:

$$R = R_0 \exp(-\frac{\Delta H_{vap}}{k_B\, T}) . \tag{3.3}$$

Parameter R_0 is accounting for cell and chamber geometry, ΔH_{vap} is the enthalpy of vaporization, T is the cell temperature and k_B the Boltzmann constant. To obtain the desired flux ratio, the cell temperature or EBE power are adjusted according to the calculations.

For the oxygen gas source the flux is calculated from the pressure measured in the chamber with the following equation:

$$O_2 flux = \frac{p}{\sqrt{2\pi \cdot m_{O_2} \cdot k_B \cdot T}} . \tag{3.4}$$

Here p is the pressure measured with the ion gauge, m_{O_2} is the mass of the oxygen molecule and T the temperature of the oxygen. The measured pressure during oxygen inlet can be regarded as the oxygen partial pressure because the residual gas pressure in the chamber is two orders of magnitude smaller than the oxygen pressure. Because of the position of the ion gauge (shown in Figure 3.3) behind the LN_2 cooling shroud, the calculated flux is only a rough estimate of the actual O_2 flux at the wafer surface.

3.2.2 MBE Growth Process and Growth Modes

MBE is a non-equilibrium process in which ultra-pure source material is evaporated to form molecular or atomic beams aimed at the substrate. The gaseous elements condense on the substrate where they are physisorbed before they are incorporated (chemisorbed) into the crystal. Figure 3.4 shows the different processes on the substrate surface during growth. The impinging atomic beam is characterized by the flux of the arriving species which gives the number of atoms arriving per time and area. The energy distribution of the arriving atoms corresponds to the temperature of their source. Usually the substrate temperature is lower than the temperature of the sources. Until the atoms are in thermodynamic equilibrium with the substrate, they exchange energy with the atoms of the substrate. These interactions include diffusion, interdiffusion, nucleation and even re-evaporation (desorption) if the energy is sufficient. Most important is the possibility of diffusion along the surface until the atom reaches a step edge at which it is incorporated into the crystal.

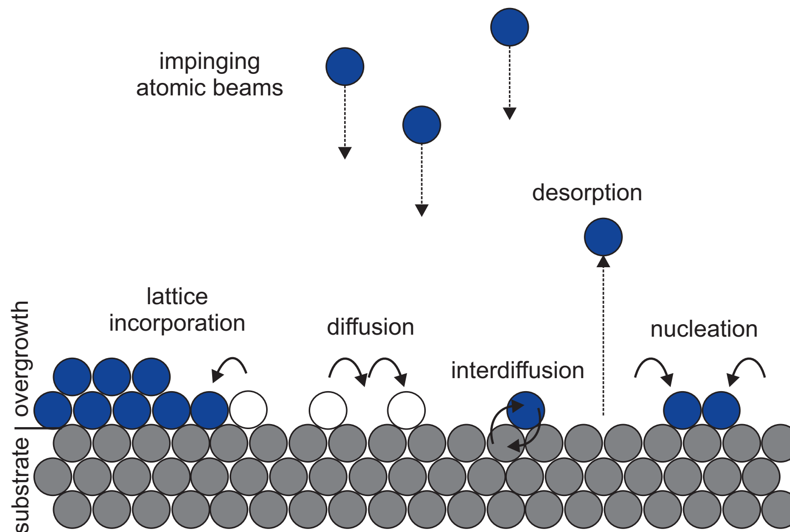

Figure 3.4: Illustration of the growth processes occurring on the substrate surface during MBE growth.

This process enables a growth mode in which the crystal grows one layer at a time until it is complete and only then the next layer starts to form.

This is known as the Frank van der Merwe or layer-by-layer growth mode. Other growth modes are Volmer-Weber and Stranski-Krastanov. The first describes the growth from three-dimensional nucleation (island growth) and the second is a mixture of layer-by-layer and island growth. In Figure 3.5 all three growth modes are illustrated. Although these growth modes are simplifications not accounting for the growth kinetics, and therefore not suitable to describe all known growth phenomena [Mah07], they are sufficient to describe the layer growth of silicon and silicon alloys [Kas82]. When the surface atoms have enough energy so that their diffusion length is larger than the distance between the step edges, the atoms are incorporated at the energetically-favored step edge. This is called step flow growth and is a type of layer-by-layer growth. The surface steps for commercially available wafer originate from the slight misorientation of the wafer against a low index plane [Kas82]. The substrates used here have a misorientation $< 0.5°$ and therefore the terrace width is > 155 Å.

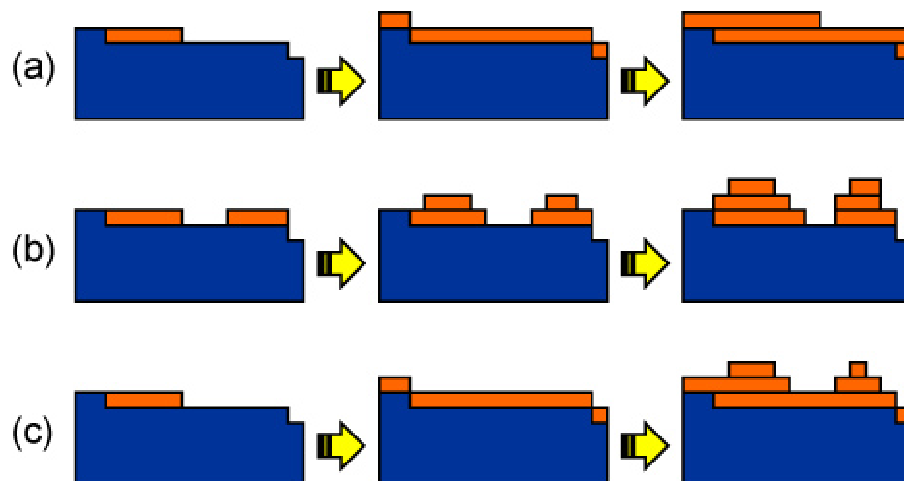

Figure 3.5: Illustration of the growth modes (a) Frank van der Merwe (b) Volmer-Weber and (c) Stranski-Krastanov.

3.3 RHEED

Reflection high energy electron diffraction (RHEED) is a technique used to analyze crystal growth in situ without interfering with the growth process. It provides information on the nature of epitaxy and surface morphology. Technical requirements are an electron gun for a focused electron beam with an energy of usually 10 keV, and a fluorescent screen to watch the diffraction pattern. In addition a camera can be used to record the pattern. The electron beam is directed at the substrate at a glancing $\leqq 3°$ angle which limits the penetration of the primary electrons to the top few monolayers. In Figure 3.2 on page 20 the positions of gun and screen on the MBE are indicated.

The diffraction condition is given by

$$\vec{k_i} - \vec{k_d} = \vec{G} \tag{3.5}$$

where $\vec{k_i}$, $\vec{k_d}$ are the wave vectors of the incident-, diffracted-beam and $\vec{G}$ is the reciprocal lattice vector of the crystal. If $|\vec{k_i}| = |\vec{k_d}|$ than the diffraction condition can be described by the Ewald construction (see [IC04]). At an operating voltage of 10 kV the electron wavelength is 0.122 Å and thus $|\vec{k_i}| = 51.6\,\text{Å}^{-1}$. This is much larger than the reciprocal lattice unit of the crystal that is analyzed ($a_{Si} = 5.431$ Å, $\vec{G} = 2\,\pi/a = 1.16\,\text{Å}^{-1}$). Because of the size difference, the Ewald sphere cuts through several points of the reciprocal lattice. The reciprocal lattice points of a real-space two-dimensional lattice are one-dimensional rods normal to the surface. Because of the low penetration depth of the electron beam, the crystal can be considered a two-dimensional lattice. The resulting RHEED pattern of a smooth surface consisting of equidistant streaks is shown in Figure 3.6.

Figure 3.6: RHEED reconstruction pattern of a Si (001) wafer. The streaks are highlighted by lines for better recognition. Electron beam is along <110>-direction.

The streaks are a result of the intersection of the much larger Ewald sphere with the reciprocal rods. The finite thickness of the streaks in the RHEED pattern is caused by lattice imperfections and thermal vibration. It has to be noted that the Ewald sphere also has a finite thickness caused by electron energy spread and beam convergence.

In reality the surface of the sample is not a perfect two-dimensional lattice; thus the diffraction process is not true reflection. On rough surfaces transmission-reflection diffraction through surface asperities produces a spotty diffraction pattern. This difference in the diffraction pattern can be used to distinguish the current surface condition. Figure 3.7 depicts the difference between true reflection diffraction and transmission-reflection diffraction.

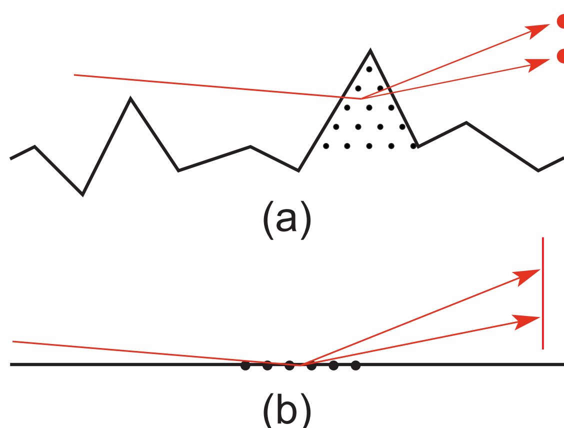

Figure 3.7: Schematic of (a) transmission-reflection diffraction and (b) true reflection diffraction.

3.4 X-Ray Techniques

In this section, the x-ray analysis methods and their evaluation are described. A brief overview of the equipment used for analysis is given. X-ray analysis techniques are non-destructive methods to gain information about crystallographic structure and chemical composition.

3.4.1 High Resolution X-Ray Diffraction

X-rays are scattered by the periodic electron distribution in a crystal. Diffraction of x-rays occurs when the scattered radiation is coherent, thus producing constructive interference at specific angles. Two rays scattered on different lattice planes have a phase relation that

depends on the difference of path length. Figure 3.8 shows the scattering of two beams from different lattice planes.

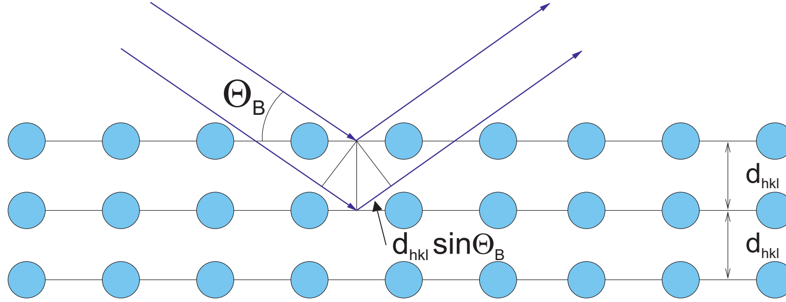

Figure 3.8: Diffraction condition for x-ray diffraction. The phase of two rays depends on the difference of path length that, in turn, depends on the angle of incidence and the distance of the lattice planes.

The scattering condition is described by Bragg's law:

$$2d_{hkl} \sin \Theta_B = \lambda \tag{3.6}$$

where Θ_B is the angle of incidence and d_{hkl} the distance between the lattice planes with the indices h,k and l, for cubic lattices d_{hkl} can be written as:

$$d_{hkl}^2 = \frac{a^2}{h^2 + k^2 + l^2} \ . \tag{3.7}$$

From the Bragg equation some boundary conditions for x-ray diffraction can be devised. Since $\sin \varTheta$ is at maximum one, λ must be smaller than $2d_{hkl}$. In general, the distance of lattice planes is of the order of 3 Å or less thus λ must not exceed 6 Å [HS96]. However, $\varTheta$ becomes too small for easy measurement if λ is much smaller than d_{hkl}. The copper $K_{\alpha 1}$ radiation is widely used as an x-ray source because the wavelength is $\lambda_{Cu_{K\alpha 1}} = 1.54056$ Å and thermal properties of copper make it a suitable material for the anode.

Analysis of the samples has been performed with a Philips X'Pert diffractometer. The x-ray source has a copper anode and a germanium four bounce monochromator from which the x-rays reach the sample stage. The sample stage consists of a Euler cradle that can independently operate the variables. On the diffracted beam side, two proportional detectors are mounted, one with a slit (rocking curve optics) and the other with an analyzer crystal (triple axis optics). The experimental setup is shown in figure 3.9.

The standard measuring method is the Omega-2Theta (ω-2$\varTheta$) scan. Usually aligned for a symmetric reflection like (004 for a (001)-Substrate), this scan is able to give information about the thickness composition and the vertical lattice constant $a_\perp$ of an epitaxial layer. An epitaxial layer produces a peak in an ω-2$\varTheta$-scan that is separated from the substrate

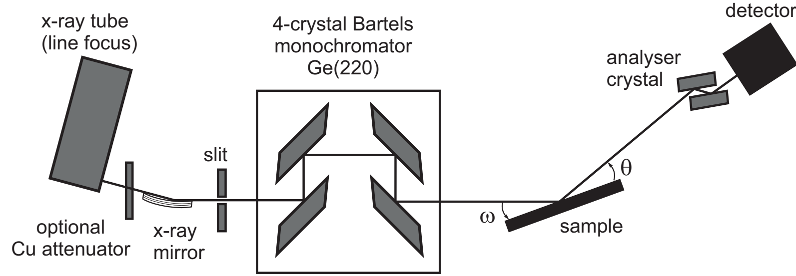

Figure 3.9: Schematic of the setup for x-ray diffraction and reflectivity. For XRR the Cu attenuator must be in place to scan through the direct x-ray beam which otherwise would damage the detector.

peak because of the difference in the vertical lattice constant between layer and substrate. The vertical lattice constant of the layer can be calculated from the scan using Bragg's equation (3.6). Thickness oscillations, called fringes, can be used to determine the thickness of the layer. The oscillations are a result of the diffraction on a finite number of lattice planes and can be regarded similar to the diffraction pattern of a single slit. For oscillations close to the Bragg peak the layer thickness can be calculated with the formula:

$$t = \frac{\lambda}{\Delta\Theta \cdot 2\cos\Theta} \; . \tag{3.8}$$

Here, $\Delta\Theta$ is the angular distance between two neighboring oscillation peaks and Θ is the Bragg angle. Formula 3.4.1 can be used to evaluate the period of a superlattice from the superlattice oscillations, too.

If the layer consists of an alloy of two materials (A and B) the composition can be determined from the peak position of the layer using Vegard's law [Veg21]. The lattice constant of the alloy is a linear interpolation between the lattice constants of the two alloy constituents:

$$a_{A_{1-x}B_x} = a_A \cdot (1-x) + a_B \cdot x. \tag{3.9}$$

Deviation from Vegard's law are known for some alloys, such as $Si_{1-x}Ge_x$ or $Al_{1-x}Ga_xAs$. For SiGe alloy the deviation was measured by Dismukes et al. and later a quadratic approximation of the deviation is reported by Herzog [DEP64; Her95].

In order to measure the vertical and lateral (in plane) lattice constant of the layer an asymmetric reflection has to be measured. Two measurement geometries are possible for asymmetric reflections, the coplanar and non-coplanar geometry. In the coplanar geometry the normal vector of the lattice planes [hkl] that are measured lies in the plane of the x-ray beam. To achieve this geometry the sample rotation φ is rotated, so that [hkl] is in the beam plane and the inclination angle between the surface normal and [hkl] is added or

subtracted to ω. For some reflections the resulting ω angle is negative or too large to be measured in this geometry. In the non-coplanar geometry the independent variation of all four angles (ω, Θ, φ and ψ) is used to align the lattice planes to the x-ray beam. Here, ω and 2Θ maintain the relation $\omega = \Theta$. The orientation of the lattice planes towards the x-ray beam is performed by adjusting ψ and φ. In this geometry all reflections that lie above the sample surface and for which the incident and emergent angle are positive can be measured. With Bragg's law (3.6) and the following relation:

$$\frac{1}{d_{hkl}^2} = \frac{h^2}{a^2} + \frac{k^2}{b^2} + \frac{l^2}{c^2} \tag{3.10}$$

the lateral lattice constant can be calculated from asymmetric reflections. The relation 3.10 is valid for lattices with cubic lattice vectors a, b and c and the angles $\alpha = \beta = \gamma = 90°$. In the case of a cubic lattice under biaxial strain the vectors a equals b, but c is different. Vector c represents $a_\perp$ and can therefore be determined with a ω-2Θ-scan of a symmetric reflection.

In the case of in-plane strain in the (111)-plane all cubic lattice vectors and the angles are influenced by the strain; the cubic unit cell is distorted rhombohedrally. The in-plane strain can be determined more easily in reciprocal space rather than in the cubic real space system. The geometry for a reciprocal lattice point *hkl* in reciprocal space is shown in Figure 3.10. The scattering vector $\vec{H}_{hkl}$ can be segmented into $q_\perp$ and $q_\|$. Where $q_\perp$ is perpendicular to the crystal surface, i.e. in [111]-direction and $q_\|$ is in a direction perpendicular to [111]. The angle ϕ between the [111]-direction and $\vec{H}_{hkl}$ is equal to the inclination between the (111) and (hkl) lattice planes. From Figure 3.10 the following relation can be deduced:

$$q_\| = \vec{H}_{hkl} \sin\phi \ . \tag{3.11}$$

Together with the general relation $d_{hkl} = \frac{1}{|\vec{H}_{hkl}|}$ [War69] and the Bragg equation (equation 3.6) a formula for $q_\|$ can be formed:

$$q_\| = \sin\phi \cdot \frac{2\sin\Theta}{\lambda} \ . \tag{3.12}$$

For a detailed description of reciprocal space, x-ray diffraction and the derivation of the formulas connecting reciprocal to real space B.E. Warrens book *X-ray Diffraction* is advised [War69].

Very thin epitaxial layers do not have enough scattering volume to produce a peak in x-ray diffraction. But the phase difference between the neighboring Si layers can be used to analyze the thin layer and the embedding layers. This technique is described by Tapfer and Ploog and was named x-ray interference in ultrathin epitaxial layers [TP89].

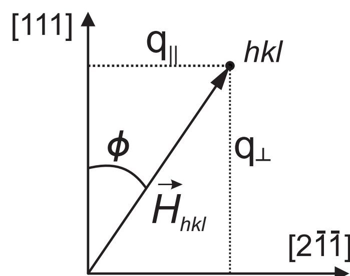

Figure 3.10: Illustration for the geometry of the of a lattice point hkl in reciprocal space. The scattering vector $\vec{H}_{hkl}$ can be segmented in two components: $q_\perp$ perpendicular to the surface and $q_{||}$ in the surface plane.

3.4.2 X-Ray Reflectivity

X-ray reflectivity is a fairly easy-to-realize method of analysis for thin films. It is not restricted to certain materials and can be used on single layer or multilayer structures, crystalline or amorphous. For x-rays the optical properties depend mainly on the electron density, and only the electrons of single atoms need to be considered. In solid bodies, x-rays have a refraction index $n < 1$, whereas in air the refraction index is $n = 1$. So the solid body is the optically thinner material and for small angles (usually $< 1°$) total reflection occurs.

X-ray reflectivity measurements are performed on the same x-ray machine as the Omega-2Theta scans. Variations of the setup shown in Figure 3.9 are needed to perform a x-ray reflectivity scan. These include exchanging the analyzer crystal for the slit and inserting the Cu attenuator to protect the detector from the direct x-ray beam. In a scan, Omega is changed continuously and the detector angle 2Theta is changed accordingly so that the incident angle equals the emergent angle. Omega has an offset that allows for corrections due to uneven samples or a not perfectly aligned sample mounting.

Layer thickness, layer roughness, and layer density can be evaluated from the measurement. From the critical angle at which total reflection occurs, the layer density can be calculated. For good results, a knife edge above the sample is necessary for a unique incident angle; this is not included in the Philips X'Pert x-ray machine. With a larger Omega angle, the intensity of the reflected x-rays decreases very fast and thus usually the scan has a logarithmic scale. The decreasing intensity is modified by oscillations that are caused by the interference of reflected x-rays from the upper and lower side of the layer and are used to determine the layer thickness. Interface roughness of the layer correlates to the steepness of the decreasing intensity and the depths of the minima.

The measurements are evaluated by fitting a theoretical reflectivity curve to the measurements data. Parameters for the fit are density, layer thickness and roughness for each layer and the substrate density. Philips software Epitaxy is not capable of fitting x-ray

reflection data, so the online database *CXRO X-Ray Interactions With Matter*[3] has been used. The measured data has been loaded into a Mathematica file that included a script to receive the fitting data directly from the above mentioned source.

3.5 Atomic Force Microscopy

Atomic force microscopy (AFM) is a very powerful tool for surface analysis. Consisting of a cantilever with a fine tip, a laser beam, piezo elements, a detector and controller the AFM setup is rather small; however, atomic resolution in z-direction can be achieved. In Figure 3.11 the setup of AFM is presented. AFM has two different working modes; the DC mode, in which the cantilever touches the surface and the force is held constant, and the AC mode. The latter is the standard mode and is the only one used in this work; it works with a cantilever that is excited, permanently, with its resonance frequency. In close proximity to the surface, the oscillation of the cantilever will be damped and these changes are registered by the detector. The computer processes the data from the detector into a false color image of the sample surface. With piezo elements the cantilever is moved across the surface in x and y direction. In combination with the measured height of the sample, a three dimensional false color image of the surface is formed. In order to focus

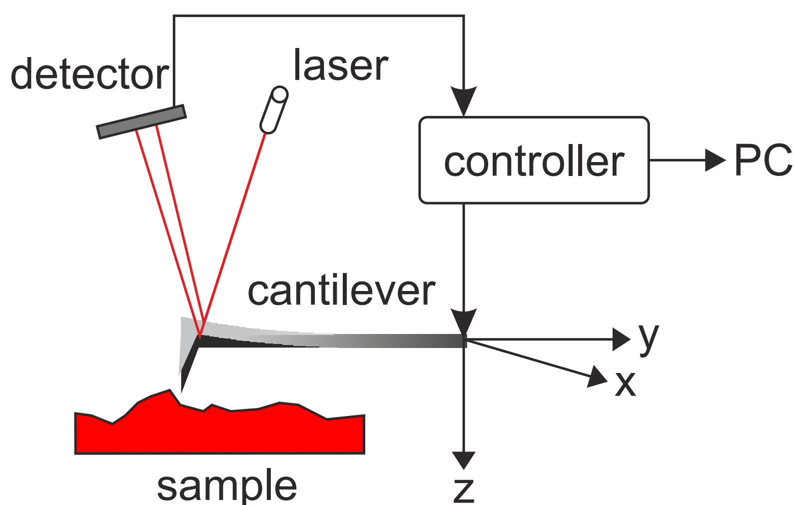

Figure 3.11: Setup for atomic force microscopy. In AC mode the tip does not touch the sample surface. The tip is excited at a frequency close to its resonance frequency. When the tip is brought close to the surface, damping occurs. The change in frequency can be detected.

3 http://henke.lbl.gov/optical_constants/

the image, the distance between sensor head and sample can be adjusted with micrometer screws. A CCD camera is installed in the sensor head to simplify the focusing process.

A limiting factor to the measurements is the tip of the cantilever. When new, the tip radius is specified to be below 10 nm and thus can resolve holes and valleys that are larger than 20 nm in diameter. In z-direction the AFM is able to resolve mono-atomic steps. The x and y resolution is limited by the effective tip size and the accuracy of the piezo elements and the positioning after a line scan for the next line.

The measurements in this work are performed on a DME DualScope™ DS 95-50/200, and the appendant software is used for the processing and data analysis[4]. For the characterization and comparison of surfaces the root mean square (RMS) is used. Calculation is performed with the AFM software for a manually selected area following the equation:

$$\mathrm{RMS} = \sqrt{\sum_{n=1}^{N} \frac{(Z_n - \bar{Z})^2}{N}} \tag{3.13}$$

Where n is a single data point, Z_n the z-value of that point and $\bar{Z}$ the average of all z-values of the selected area [DME08]. RMS is a measure for the roughness of the area but it depends only on the value of each data point, it does not account for the surroundings of the data point. Therefore, the RMS can-not distinguish different types of topography and, because the square of the data is used, larger values have a larger impact on the RMS. Thus a couple of very high values can make a large difference in the RMS. Using the RMS to evaluate and compare surface roughness demands that the samples chosen have comparable topography and that runaway values are excluded from calculation. Furthermore, scan speed and size of scan area are indirect factors for RMS, as they influence the measurement and therefore samples should have the same scan parameters.

3.6 Transmission Electron Microscopy

With MBE the manipulation of crystals on a very small scale is possible and therefore techniques are necessary to observe the changes on that scale. Transmission electron microscopy (TEM) is one technique to analyze materials on the atomic scale. Because of the technical requirements and the need for the sample to allow for electron transmission, TEM is very expensive and time consuming.

For the sample preparation there are several methods available, but most are very invasive and can destroy delicate sample features, especially while preparing a so called lamella for a side view TEM. This means that the view is not along the sample surface normal,

4 DualScope™/Rasterscope™ SPM Ver. 2.3.0.6

instead it is parallel to the surface. With a focused ion beam (FIB), the lamella is cut out of the sample and thinned down in several steps. For TEM with very high resolution the requirements on the sample preparation are especially high; the sample needs to be thinned down as much as possible. The lamella needs to be thinner than 100 nm, but, for high resolution, 50 nm is still very big and lamellas with 20 nm or less are ideal. Overall, the preparation takes six to eight hours, depending on the experience of the operator.

The TEM used allows for acceleration voltages up to 300 keV und thus an electron wavelength of 0.022 Å (non relativistic calculation). Because of the spherical aberration, the resolution is limited to 0.2 nm instead of the theoretically possible resolution of less than 0.02 Å.

The TEM can operate in different modes; these are conventional TEM for bright- and dark-field images, electron diffraction, high resolution TEM (HRTEM) and scanning TEM (STEM). Detailed description of TEM, its various modes and their analysis, can be found in Williams and Carter: *Transmission Electron Microscopy* and Scott and Love: *Quantitative Electron Probe Microanalysis* [WC96; SL83].

In this work, all TEM images are the result of a cooperation with the Röntgen-Center for Complex Materials. For the preparation, a FEI Helios Nanolab dual-beam system is available and the images are taken with a FEI Titan 80-300 TEM.

3.7 Secondary Ion Mass Spectrometry

Secondary ion mass spectrometry (SIMS) is a very powerful tool for chemical analysis of surfaces and thin films. Concentrations of trace elements lower than one part per million can be detected. For thin films, the capacity to measure depth profiles of concentrations is of particular interest as it enables very accurate calibration of doping or intentional cooperation of trace elements. The capabilities of SIMS to measure the composition of alloys, on the other hand, is rather limited by the so called matrix effect.

With a focused ion beam (primary beam), energy is transferred to the surface atoms so that these can leave the surface (secondary beam) and then be detected by a mass spectrometer. The ion current density of the primary beam is critical for the operation mode of SIMS. At low current densities the mode is called static SIMS because the surface atoms are removed very slowly, compared with the measurement time, and can be regarded as unaltered during the measurement. In this mode the lateral distribution of the chemical elements can be analyzed by scanning the primary beam over the surface. At higher ion current densities the surface atoms are removed continuously and a depth profile of the sample is measured; this mode is called dynamic SIMS.

SIMS measurements for this project have been performed by Dr. Breuer at the Forschungszentrum Jülich on a *ToF-SIMS IV* from ION-TOF. In this setup, a time of flight mass

spectrometer (TOF-MS) is used to analyze the secondary ion beam. This detector separates the different masses of the ions by the arrival time, although this only works when there is a defined time at which the ions are released from the surface. A pulsed analyzation beam of Bi_3^+ is generated and defines the start time for the detector. In analogy to static SIMS, the pulsed beam has a low current density (pulse length 1 ns; energy 25 keV) to remove only the surface atoms. A Cs^+ beam with 2 keV energy is generated to sputter the sample. Alternating both beams results in a depth profile with a very high resolution and for all ions with the right polarity. Mass resolution and mass range are determined by pulse length and time between two pulses, respectively. The utilization of a reflectron as mass spectrometer allows for a mass resolution as high as $\frac{M}{\Delta M} \approx 9000$.

In SIMS only a fraction (less than 1%) of the removed atoms are ionized and can thus be detected. Secondary ion yield varies, depending on atom species, by several orders of magnitude, and even a single atomic species has different secondary ion yields depending on its chemical environment. The above-mentioned matrix effect refers to the significant variation of ion yield of an element depending on its chemical environment in the analyzed material. As a result, for the interpretation of a SIMS signal of certain magnitude for a specific ion, a standard sample is necessary to evaluate absolute atomic concentrations from the signal. Standard samples should have the same structure, bonding configuration and impurity concentration in the same order of magnitude as the sample to be analyzed to avoid the matrix effect.

Further details on SIMS, TOF-MS and secondary ion yields can be found in Grehl: *Improvement in TOF-SIMS Instrumentation for Analytical Application and Fundamental Research*, Benninghoven et al.: *Secondary Ion Mass Spectrometry*, Behrisch: *Sputtering by Particle Bombardment I* and Vickerman and Briggs: *ToF-SIMS: Surface Analysis by Mass Spectrometry* [Gre03; BRW87; Beh81; VB01].

Chapter 4

MnSi Film Growth and Characterization

The properties of MnSi described in the introduction (see Chapter 1 on page 1) make MnSi a promising material to realize a ferromagnetic-layer/silicon interface and thus a possible key material for silicon based Spintronics. In addition, high quality MnSi thin films offer large possibilities in fundamental research. To exploit these possibilities, MnSi thin films on Si(111) substrates must be grown in high crystal quality and the parameters that influence growth have to be explored further than they have been to date. Molecular beam epitaxy is the appropriate tool to meet these demands.

In this chapter, the development of growth procedures for MnSi films is described, as well as basic characterization of the films. To date only the group of Karhu et al. has reported MBE growth of MnSi. Their findings are used as a guideline to start the widely novel MBE growth of this material.

4.1 Preliminary Work

Growth of MnSi is performed on single side polished Si(111) wafers, bought from Si-Mat company. Specifications of the wafers are: Si<111>±0.5°; thickness: 380 µm ± 25 µm; resistivity: 8000 Ωcm-10000 Ωcm; and SEMI standard flats.

4.1.1 Manganese Flux Calculation

Determination of the flux rate can not be performed during, or immediately before, the growth process, because a flux measurement gauge is not yet installed. Therefore, Mn is evaporated on to a Si substrate at room temperature. With RHEED it is confirmed that the deposition is amorphous. After the wafer is taken out of the vacuum system, the thickness of the Mn film is determined with XRR. Figure 4.1 shows the XRR measurement, together with a simulation fitted to the data. The layer thickness can be determined from the oscillation period; the slope of the curve and the sharpness of the oscillations

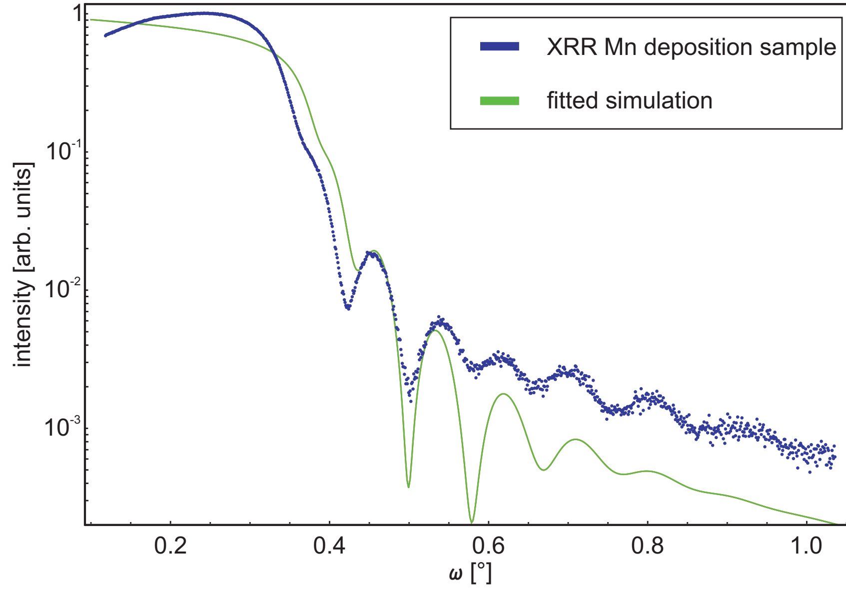

Figure 4.1: XRR measurement of Mn deposited on Si(111) wafer. The simulation is fitted to the measurement, and the layer thickness is determined to 39.0 nm.

contain information about the roughness of the interface and the surface. The deposited Mn layer is 39 nm thick, deposition duration is 1800 s and temperature of the manganese effusion cell is $T_{Mn} = 750°C$. From this the Mn flux is calculated with formula 3.2. In Table 4.1 the parameters for ρ and u that are used for all calculations are listed. From the

Table 4.1: Density and atomic mass data used for flux calculations.

	ρ [g/cm^3]	u [gram/mole]
Mn	7.430	54.938
Si	2.330	28.085
MnSi	5.820	83.023

calculation, the Mn flux, for the Mn effusion cell temperature $T_{Mn} = 750°C$, is determined to $1.76{\times}10^{14}$ cm^{-2}s^{-1}. The error of the calculation depends on the error of the thickness determination. Assuming an error of ±0.5 nm for d_{layer} leads to a relative error of 2.6% for the calculation. The change of flux with T_{Mn} is estimated from measurements of this effusion cell in another, identically built, chamber. The characteristic slope of the flux rate depending on T_{Mn} has almost no variation. Absolute flux values change with cell filling level and environment, but the slope is the same. In this case, all past measurements show a change of the flux of a factor $\frac{1}{2}$ or 2, with 20°C decrease or increase of T_{Mn}, respectively. Combining the slope and the flux determined for $T_{Mn} = 750°C$ enables determination of T_{Mn} for every flux desired.

The Si(111) wafers are prepared, prior to growth, in three steps. First, the native oxide is removed with HF etch following the description given in section 3.1. Next, the wafers are loaded into the vacuum chamber and heated to 150°C for 30 minutes. At last, prior to deposition, the H-passivated surface is thermally removed at T_{sub}= 970°C for 10 minutes and a Si(111)-7×7 surface is prepared. The RHEED pattern is shown in Figure 4.2. From the RHEED pattern it is concluded that the surface is flat and well ordered.

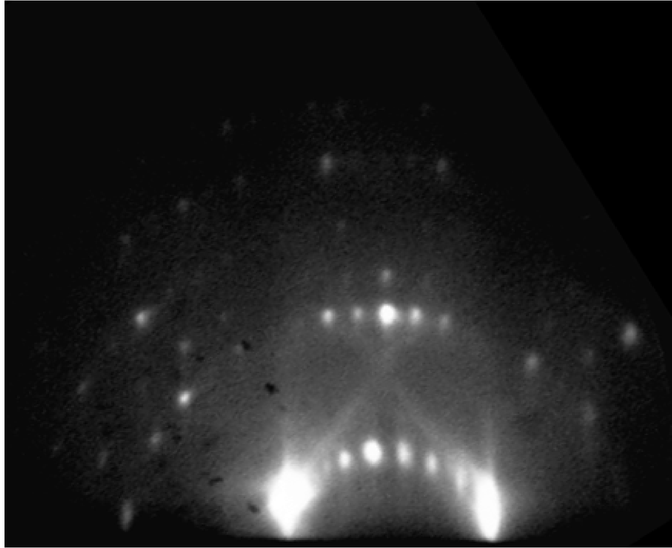

Figure 4.2: Si(111)-7×7 reconstruction prepared after the thermal removal of the H-passivation. The pattern indicates a flat, well-ordered surface.

4.1.2 Manganese Thin Film Annealing

All reported growth of MnSi starts with a thin Mn layer deposited at low substrate temperature, because MnSi does not form a wetting layer on Si, but rather grows in the Volmer-Weber mode [HKS07]. The deposited amount of Mn is crucial for the MnSi formation. The Mn amount deposited is given in mono layers (ML), one ML Mn is defined as one Mn atom per Si surface atom ($7.83\times10^{14}\,cm^{-2}$). If the amount is too small (<1 ML) islands will form, rather than a film [Kum04]. Although, the silicide reaction between Mn and Si starts at room temperature, transformation of all deposited Mn into a MnSi film, in a reasonable time, can only be achieved by annealing. To determine the right temperature for annealing, Mn is deposited on a Si(111)-7×7 surface. The RHEED pattern is now amorphous. The substrate temperature is raised to 275°C, then 300°C then 325°C and finally to 350°C. At each temperature, the sample is annealed for 1800 s. For the whole time the surface is monitored with RHEED. At 275°C and 300°C no changes in the amorphous RHEED pattern are observed, whereas at 325°C the RHEED pattern changes

and streaks become visible. Raising the temperature to 350°C enhances the features further. The streaks are more pronounced and fewer 3D features are visible. The pattern is identified as a Si(111)-$\sqrt{3} \times \sqrt{3}$ R30° pattern. With regard to the MBE layer growth, a higher substrate temperature (T_{sub} = 400°C) is tested, although no changes of the RHEED pattern could be observed at 400°C. Figure 4.3 shows the RHEED pattern of a sample after annealing at T_{sub} 400°C. The Mn amount deposited on this sample is 5.8 ML. The streaks are clearly visible in the figure, but broad; in addition Kikuchi-lines can be seen. The RHEED pattern indicates a well ordered, flat surface.

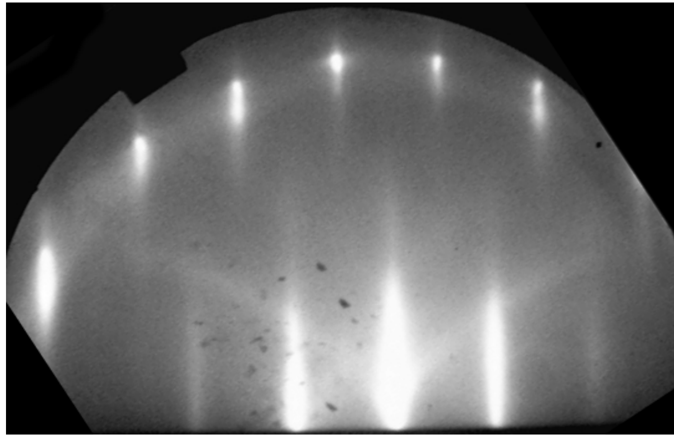

Figure 4.3: RHEED pattern of a Mn film annealed at 400°C. The MnSi(111) 1×1 pattern is visible, indicating that the surface is single crystalline.

4.1.3 Determining Film Material

After annealing, the samples are cooled down to room temperature and then taken out of the vacuum system. In order to determine what form of silicide is grown on the substrate, the samples are loaded into another vacuum system with an XPS chamber. XPS is a very handy tool to analyze surfaces and very thin films. The deposited Mn amount of ~2.25 ML results in a MnSi layer of approximately 2 quadruple layers [HKT09; Aza11]. This is well below the critical thickness for XPS, at which less than 5% of the created electrons reach the surface. Figure 4.4 shows two parts of the XPS scan of the sample with 2.25 ML Mn annealed at 350°C. The energy scale of the scan is calibrated with the O1s peak at 531.8 eV; the intensity is normalized with the Si2p3/2 peak. For identification of the peaks the *Handbook of X-ray Photoelectron Spectroscopy* is used [Wag79].

Figure 4.4a shows the scan from 45 eV to 185 eV binding energy. Most prominent features are the Si2p3/2 and the Si2s peaks. On the high energy side of the Si2p3/2 peak the Si2p1/2 and the SiO_2 2p peak can be seen. Manganese peaks – the Mn3s at 83 eV and Mn3p at 43 eV – have very low intensity and are very broad. Furthermore, the Si2p and

Si2s plasmon peaks and the Si2p x-ray satellite are visible. Figure 4.4b shows the binding energies from 500 eV to 775 eV. At 531 eV the O1s peak is visible; at 745 eV and 766 eV the O KLL Auger lines are visible. Between 610 eV and 670 eV several peaks are visible; only some of them can be identified unambiguously. The wide peak at 619 eV is identified as the Mn LMM Auger line; the small peak at 639 eV is the Mn2p3/2 peak. The two large peaks in the center of the spectra belong to Mn 2p. The left peak (Mn2p3/2) is at 642.1 eV; the gap to the right peak (Mn2p1/2) is 11.7 eV. These values fit exactly to the literature values for Mn bound to oxygen in Mn oxide.

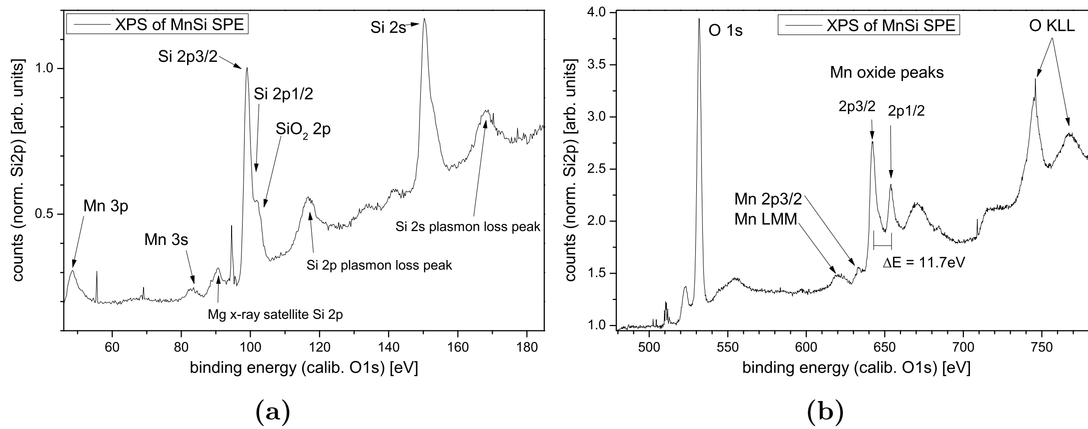

Figure 4.4: XPS spectra of a MnSi sample grown with solid phase epitaxy (SPE). 2.25 ML of Mn deposited and annealed at 350°C. The energy scale of both spectra is calibrated with the O1s peak. (a) Low energy spectra. Si photoelectron lines are the most prominent feature. SiO_2 peak is visible. Mn peaks are very weak. (b) High energy spectra of the sample. Mn lines are weak. Mn oxide peaks are prominent.

It is not possible from the data to distinguishing MnSi from pure Si and Mn or Mn oxide. The Si peaks are very strong and are generated from the substrate; the Mn peaks are rather weak because of the small amount of Mn on the surface. XPS studies of MnSi and oxidized MnSi have shown that the peaks generated by oxidation are the same as for the pure oxide of Si and Mn [Oht08]. Furthermore, the shifts in binding energy of MnSi in respect to pure Si and Mn are very small and have only been observed in bulk material or in-situ in thin films [Kum04]. The strong oxide peaks superimpose the small shifts and make an evaluation unfeasible. Therefore, the conclusion from the XPS data is that most of the Mn in the layer is oxidized.

The surface of the sample is analyzed with AFM. Figure 4.5 shows a $1 \times 1\,\mu m^2$ scan of the surface; beside that is a line profile taken along the arrow in the scan. The surface is very smooth; RMS is less than 400 pm. On the surface a couple of large islands can be seen. Their diameter is $<$200 nm, their height up to 3.0 nm. However, most of the surface is covered by small islands: diameter $<$50 nm, height $\sim$0.5 nm. These islands are likely

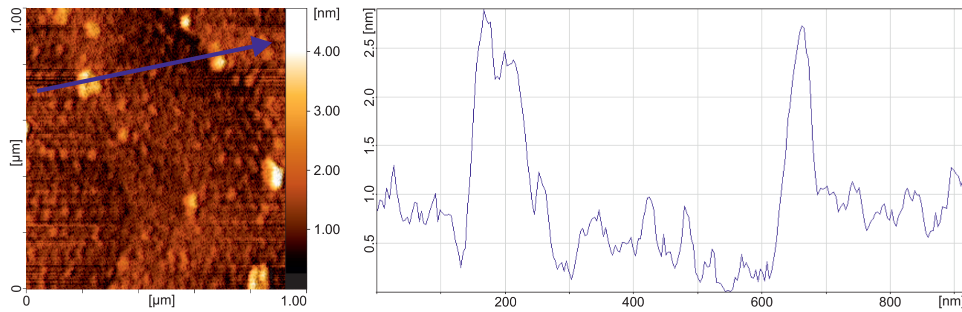

Figure 4.5: AFM scan of a sample with 2.6 ML Mn annealed at 350°C, exposed to air. The RMS is less than 400 pm.

formed during the oxidation of the surface when the samples are exposed to air.

4.1.4 Discussion

After the wafer preparation, the RHEED indicates a good Si(111)-7×7 surface. Annealing of an amorphous Mn layer above 325°C results in a reorganization of the surface. The visible RHEED pattern resembles the Si(111)-$\sqrt{3} \times \sqrt{3}$ R30° or the MnSi(111)-1×1 pattern. Both patterns are alike, only the spacing of the streaks differs by three percent because of the different surface lattice constants (see section 2.2). This difference is within the measurement error caused by the large streak width, therefore the pattern could not be clearly identified. However, the observations during film preparation indicate that the silicide reaction transforms most of the surface into an ordered state and the morphology is two-dimensional.

The XPS analysis shows that Mn is deposited on the surface and did not desorb at temperatures up to 400°C. Dominant features in the spectra are the Mn oxide peaks. The position of the Mn2p3/2 peak and the energy distance to Mn2p1/2 are the exact values reported in the literature. The presence of peaks of pure Mn indicates that there is Mn on the surface that has not been oxidized. This can be pure Mn or MnSi, because the energy shift of the two is too small to distinguish in the spectra. In the area of the Si2p peak a peak is visible that corresponds to Si bound in SiO_2 .

XPS analysis shows that the thin MnSi layer is oxidized when exposed to air. Supporting this is the AFM scan; here small islands are visible that could be connected to the oxide formation on the surface. In conclusion, the MnSi film needs to be protected from oxygen exposure. Therefore, the MnSi layer needs a stable capping layer, before the samples can be taken out of the vacuum.

4.2 Molecular Beam Epitaxy of MnSi

4.2.1 Growth of MnSi Thin Films

From the results of the preliminary work a procedure for MBE growth is deduced. Sample preparation, heating and removal of H-passivation are performed in the same manner as before. However, before the Mn is deposited a Si buffer layer is grown. Etching with HF roughens the surface and a buffer layer can reduce the surface roughness. Si growth is performed at T_{sub}= 750°C and monitored with RHEED. All buffer layers are ~ 32 nm thick and grown with a rate ~ 0.15 Å/s. Figure 4.6 shows a RHEED image of the surface with the Si(111)-7×7 reconstruction after buffer layer growth. The pattern is consistent with a smooth, two-dimensional, high quality surface.

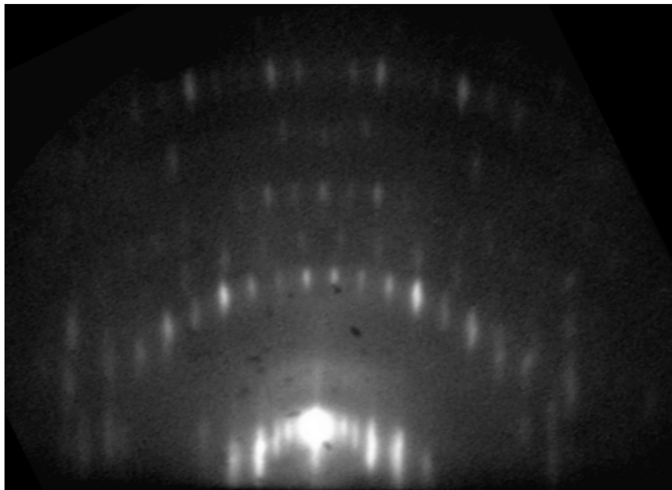

Figure 4.6: Si(111)-7×7 reconstruction after 32 nm of buffer layer. The pattern indicates high crystal quality.

After the buffer layer is grown at T_{sub}= 750°C the sample is cooled to room temperature at a rate < 0.2°C/s. As soon as the temperature is stable, Mn deposition is started. The wetting layers are between 2.8 ML and 5.8 ML of Mn thick. During the deposition the RHEED pattern changes from Si(111)-7×7 to amorphous. Directly after the deposition the substrate temperature is raised for annealing, with a rate < 0.35°C/s. The temperature ramp should not be too steep in order to heat the sample homogeneously. On the other hand, the adsorption of contaminants needs to be avoided. The rate of < 0.35°C/s is a compromise between the two factors. When T_{sub} exceeds 325°C the transformation of the surface is observed; T_{sub} is stabilized at the desired growth temperature. The different Mn content of the wetting layer has no observable effect on the RHEED pattern when annealed. Growth is started by simultaneously opening the Si and Mn shutter. Throughout the growth process the surface is monitored with RHEED to note changes, such as transition

to 3D growth mode or partial amorphous diffraction. Figure 4.7 shows the RHEED pattern during MnSi growth. In Figure 4.7a the electron beam is along the $[\bar{1}01]$ direction of Si and in 4.7b along the $[\bar{1}\bar{1}2]$. The pattern is a MnSi(111) 1×1 reconstruction; the long and narrow streaks indicate smooth, epitaxial growth of a single crystal layer.

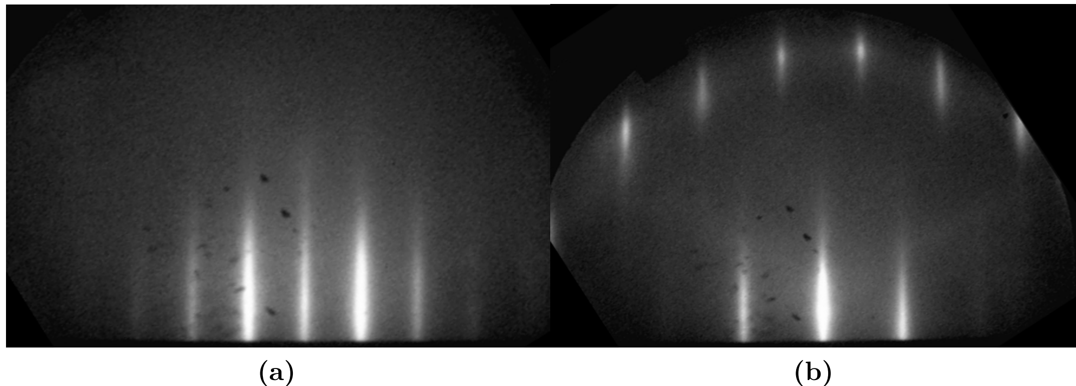

(a) **(b)**

Figure 4.7: MnSi(111) 1×1 RHEED pattern of MBE grown MnSi. (a) Electron beam along the Si-$[\bar{1}01]$ direction. (b) Electron beam along the Si-$[\bar{1}\bar{1}2]$ direction.

For MBE growth the atomic fluxes need to have the right stoichiometry in order to grow the desired material. A 1:1 stoichiometry such as MnSi is very sensitive to unbalanced flux ratios. Thus, prior to growth, the fluxes are calculated. The Mn flux is calculated as described in section 4.1.1. For the Si flux, either SiGe or SiO_x layers are grown to measure the growth rate (see chapter 5). The Si flux is calculated with equation 3.2 and the data from Table 4.1. To match both fluxes, the Mn cell temperature is adjusted, so that the Mn flux matches the Si flux.

The MnSi growth process is ended by closing both shutters simultaneously. Two types of cap layer can be grown—an amorphous and a single crystalline cap layer. For the former, the sample is cooled to 50°C at a rate <0.13°C/s, then a-Si is deposited. After approximately 30 s the RHEED reconstruction from MnSi vanishes and an amorphous RHEED is visible. For the c-Si cap layer the substrate temperature is not changed. The cap layer is started after a short interruption. For the first 4 ML no changes of the MnSi(111)-1×1 pattern are observed. With increasing Si thickness the streak pattern develops spots on the streaks (3D features), as shown in Figure 4.8. The 3D features are caused by partial transmission RHEED [Mah93] Throughout the cap layer growth of 5 nm the 3D features do not change; this indicates that the surface is not becoming rougher.

The analysis of the MnSi layers has shown that a A-Si cap layer, as well as a c-Si cap layer, protects the MnSi layer from oxidization. However, crystalline layers open the opportunity for further crystalline growth on top of the MnSi layer and better processing options.

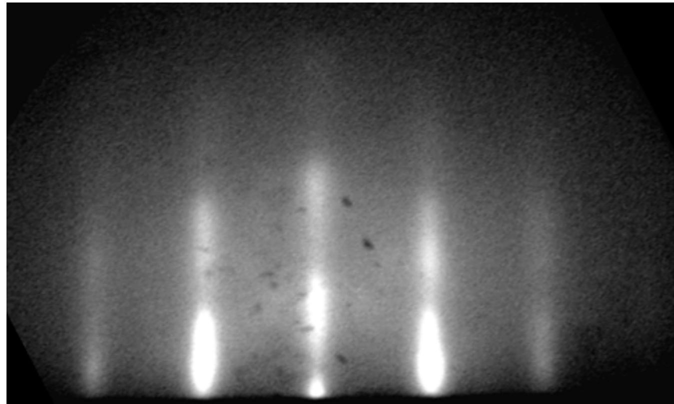

Figure 4.8: RHEED pattern during crystalline overgrowth of MnSi with Si. The pattern shows 3D features (caused by transmission reflection) but indicates epitaxial growth.

4.2.2 Characterization of MnSi Thin Films

XRR and XRD

XRR is used to determine the layers' thickness and the interface and surface roughness. The measurement of a MnSi sample and the associated fit are presented in Figure 4.9. To fit the measurements, a sample structure with two layers on a substrate is simulated. The simulation matches the XRR data well. Superposition of the oscillations from the cap layer and the MnSi layer can be observed. From the simulation the following parameters are extracted: $d_{MnSi} = 20.0\,\text{nm}$, $d_{Si\ cap} = 7.9\,\text{nm}$, interface roughness MnSi/Si cap = 0.1 nm and surface roughness = 0.1 nm. The XRR measurements indicate that the MnSi samples have a relatively homogeneous thickness and interface.

The MnSi layers are analyzed with x-ray diffraction. First, a wide ω-2Θ-scan is performed to identify the layer peaks, shown in Figure 4.10. In addition to the MnSi sample, a sample with stoichiometry Mn_5Si_3 is shown (in red); the different silicide phases are easy to distinguish with XRD. The Mn flux was not adjusted precisely enough, so that too much Mn reached the surface and the Mn rich phase formed. The Si peaks in the scan are easily identified as Si(111), Si(222) and Si(333). Calibration of the ω-axis is performed with the position and literature values of the Si(111) peak. In the scan of the MnSi sample, two more peaks are visible: the first at 17.088° and the second at 35.987°. These peaks are identified as MnSi(111) and MnSi(222), respectively. The position of the MnSi(111) peak translates (equation 3.6) into a vertical lattice plane spacing of 2.6215 Å; that is -0.43 % off the literature value for the (111) lattice plane spacing of bulk MnSi (2.6327 Å). The difference of the lattice spacing to the literature value of bulk MnSi could be caused by strain in the layer. Because the Si lattice constant is larger than that of MnSi, the strain is tensile and results in a reduced lattice spacing in [111]-direction. Although relaxation of

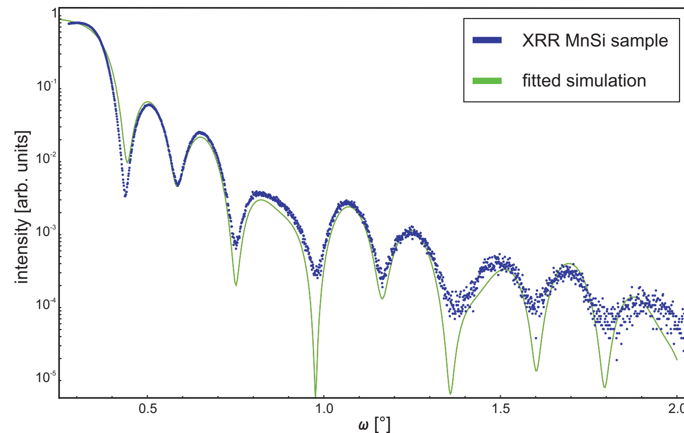

Figure 4.9: XRR measurement of a 20.0 nm MnSi sample. The fit matches the XRR data well. The superposition of the oscillations of the two layers (MnSi and a-Si cap) can be seen.

the MnSi layer starts almost immediately with layer growth, caused by misfit dislocations at the interface [Kar10], the layer could still contain some strain. This would explain the slightly reduced lattice spacing in [111]-direction.

For all samples grown, which exhibit MnSi peaks in ω-2Θ-scans, the (111) lattice spacing is determined. The average lattice spacing of five samples is 2.624 Å; that is -0.33 % off the literature value. The error of the measurement is ±0.02 %. With the Si(111) peak the sample is aligned and the axis calibrated, this allows for the small error of the measurement. Biaxial strain in the (111)-plane distorts the cubic MnSi unit cell (described in section 3.4), therefore the measured lattice spacing cannot be calculated into the cubic lattice constant following equation 3.7. Instead the elastic moduli of MnSi would be needed for an exact calculation but the elastic moduli of MnSi are not entirely determined. In the scans of the various samples there is no indication, that the Si cap-type influences the lattice constant of the layer.

A high resolution scan of the MnSi(111) peak is shown in Figure 4.11a. Thickness fringes are visible on both sides of the scan. Evaluation of the fringe period leads to a layer thickness of 20.6 nm. This is in good agreement with the XRR measurement (20.0 nm). The pseudo Voigt fit in the graph is used to determine the peak position and FWHM. For MnSi grown by MBE there is only one publication that presents XRD data, to which the results can be compared. The FWHM of the 20 nm MnSi layer is 0.20°. Karhu et al. show XRD data with a FWHM of ~0.21° for a layer with 26.7 nm [Kar12b]. Considering the broadening by a smaller layer thickness, the layer grown here has at least equal crystalline quality regarding the lattice spacing variation. In the ω-scan (Fig. 4.11b) of the MnSi(111) peak, slight broadening at the base is visible; the FWHM in this scan is 0.21°. In an ω-scan 2Θ is constant and the incident angle is varied; therefore the ω-scan is sensitive

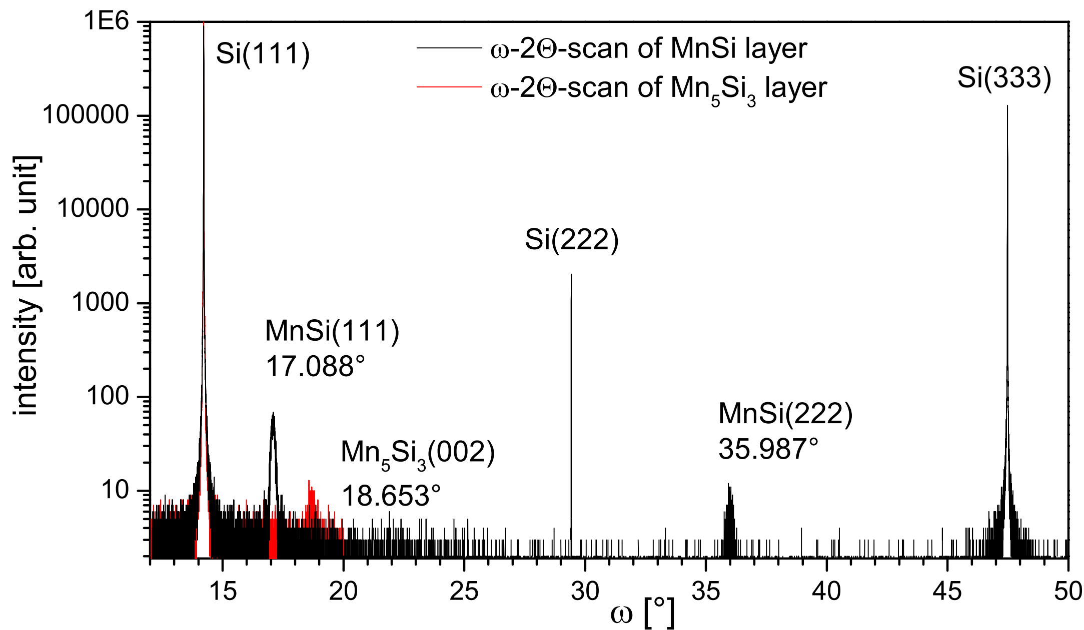

Figure 4.10: ω-2Θ-scans of a MnSi sample (black). For comparison a scan of a Mn_5Si_3 layer is shown (red). The ω axis is calibrated with the Si(111) peak. The positions of the peaks are extracted by fitting the peaks.

to angular variations of the lattice planes and further to finite crystallite size effect. The angular variations of the lattice planes can be caused by dislocations or mosaicity tilt. Dislocations are reported to form at the Si(111)/MnSi(111) interface [Kar10] and therefore are a likely explanation, although mosaicity tilt can not be eliminated as a cause based on the measurements.

Figure 4.12a shows a φ-scan of the asymmetric (210) reflection of MnSi. Six peaks are visible in the scan, three peaks have high intensity the other three peaks have low intensity. The peaks with the same intensity are 120° apart. In a simple cubic symmetry the (210) reflection is sixfold and all peaks are identical. Caused by the non-centro symmetry of MnSi the (210), (021) and (102) reflections have different intensities than the (120), (012) and (201) reflections. The calculated ratio of intensities of the reflections (210):(120) is 10:1 [Chi90]. In the measurement the ratio is (210):(120) $\approx 8 : 1$. Because of the low peak intensity the error is quite large. The measured intensity ratio is in agreement with the literature when the error of the measurement and the uncertainty of the alignment (due to the low peak intensity) are considered. Furthermore, the φ-scan of the (210) reflection shows broadening of the peaks of $\sim 1.0°$. Broadening in φ-direction corresponds to mosaicity twist.

Figure 4.12b shows the φ-scan of the asymmetric MnSi (211) reflection. The MnSi-(211)

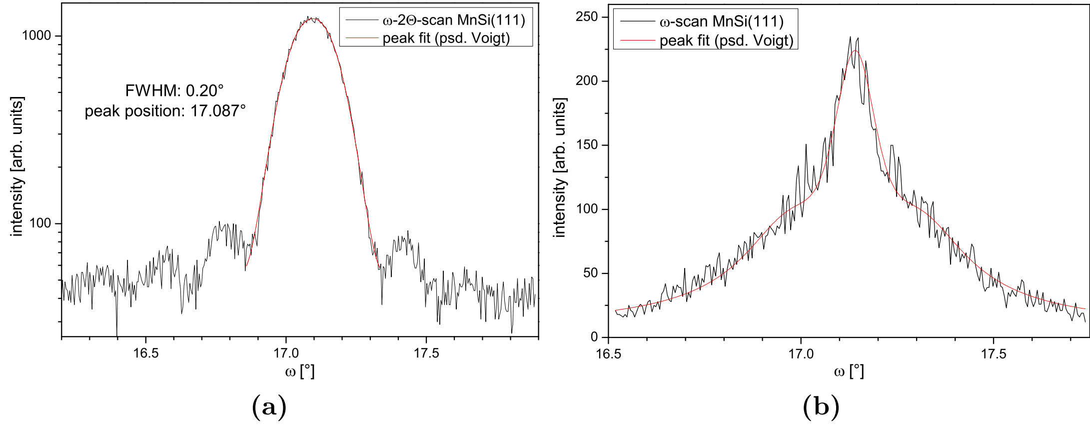

Figure 4.11: (a) ω-2Θ-scan with pseudo Voigt peak fit. On both sides of the peak fringes are observed. Their period corresponds to a layer thickness of 20.6 nm. (b) ω-scan with pseudo Voigt peak fit. Shoulders on both sides of the scan are visible.

reflection has a threefold symmetry, but six equidistant (60°) peaks can be measured with XRD. To every peak (211), (112) and (121) another peak is measured at $\Delta\varphi = 180°$. The additional observed peaks of the (211) reflections are likely caused by twinning on the $\{\bar{1}01\}$-plane, during the MnSi growth.

The MnSi(211) reflection is used to determine the in-plane strain. The relative change of the in-plane reciprocal lattice vector in direction $[2\bar{1}\bar{1}]$ corresponds to the in-plane strain. Following equation 3.12 the lattice vector is calculated from ω-2Θ-scans. The reference lattice vector is calculated for the same direction in the cubic unit cell of MnSi with $a_{MnSi} = 4.560$ Å. In a 20 nm MnSi layer the in-plane strain is determined to 0.28 %, that means the layer is very lightly tensile strained. This is in agreement with the measured out-of-plane strain, which is negative. The error of the in-plane measurement is ± 0.15 %. The reason for the large error is that no substrate peak is in the ω-2Θ-scan to calibrate the axis and align the sample. Further, the low count rate and wide FWHM of the (211) peak creates uncertainty in the evaluation of the peak position. The exact in-plane strain cannot be analyzed due to the large error of the measurement, but it is obvious that the MnSi film is not pseudomorph.

The position in ψ and φ of the MnSi (210) peak are evaluated with respect to the Si substrate. The Si substrate orientation is determined with the Si(004) reflection. From the inclination ψ and the rotation φ the following crystallographic relation has been identified:

$$[111]_{\mathrm{Si}} \parallel \{111\}_{\mathrm{MnSi}} \text{ and } [2\bar{1}\bar{1}]_{\mathrm{Si}} \parallel [10\bar{1}]_{\mathrm{MnSi}}. \tag{4.1}$$

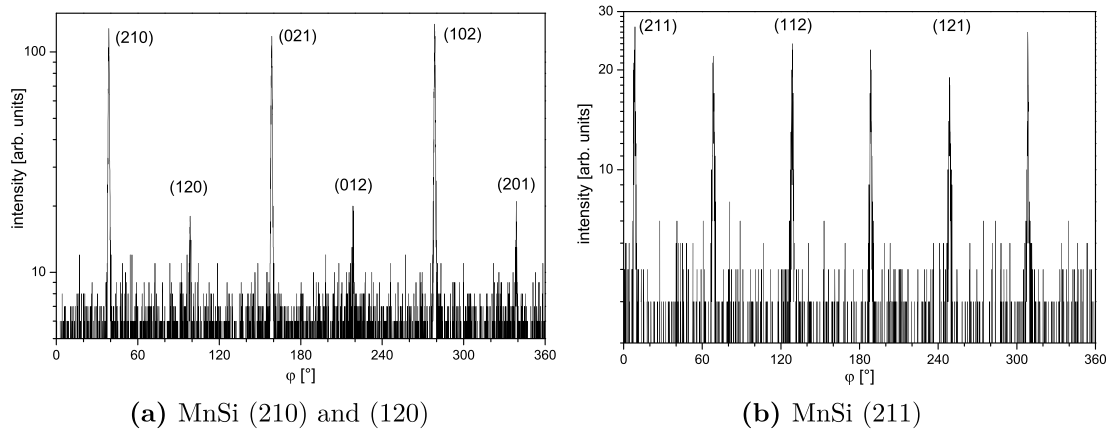

(a) MnSi (210) and (120)

(b) MnSi (211)

Figure 4.12: (a) φ-scan of MnSi (210) reflection. The intense peaks (corresponding to MnSi(210)) are 120° apart and small peaks (corresponding to MnSi (120)) are in between, 60° away. (b) φ-scan of MnSi (211) reflection. The peaks are equidistant, 60° apart.

The determined crystallographic relation is equivalent to the reported relations by Zhang et al. and Suto et al. [Zha02; Sut09].

Figure 4.13 shows an ω-2Θ-scan of MnSi (210). At high ω values a second peak is observed. It is identified as the Si (511) reflection. Although the inclination ψ of the MnSi (210) is 39.23° and for Si (511) it is 38.94°, the peak is observed due to the geometrical factors of the diffractometer that allow for several degrees of ψ to be observed. Therefore, the Si (511) and MnSi (210) planes are parallel, within the error of the inclination.

The x-ray analysis shows that the MnSi layers are, except for the twinning, homogeneous and single crystalline films. The MnSi layers exhibit mosaicity-tilt and mosaicity-twist in the order of 0.2° and 1°, respectively. The intensity ratio of the (210) and (120) reflections is in agreement with reported data for MnSi [Chi90]. Twinning on the $\{\bar{1}01\}$-plane is observed in the φ-scans of the (211) reflection. The twinning could be caused by the presence of right handed and left handed MnSi phases, because the transformation from one chirality to the other is a mirror operation with respect to a $(1\bar{1}0)$ plane. Usual diffraction methods cannot determine the right handed from the left handed crystal, other methods such as x-ray anomalous dispersion measurement could provide the information [Ish85].

The observed orientation between the MnSi (210) and the Si (004) reflection ($\Delta\psi = 15.51°$; $\Delta\varphi = 0.13°$) is equivalent to the reported crystallographic relation between MnSi(111) grown on Si(111) [Zha02; Sut09]. The broadening in ω of the MnSi(111) peak is probably not linked to a single cause; mosaicity tilt and mosaicity twist are observed. Furthermore, interface roughness and dislocations can contribute to the broadening in ω. In addition, it is possible that right-handed and left-handed phases of MnSi form some kind of grain boundary and therefore finite crystallite size effects could broaden the ω-scan, too.

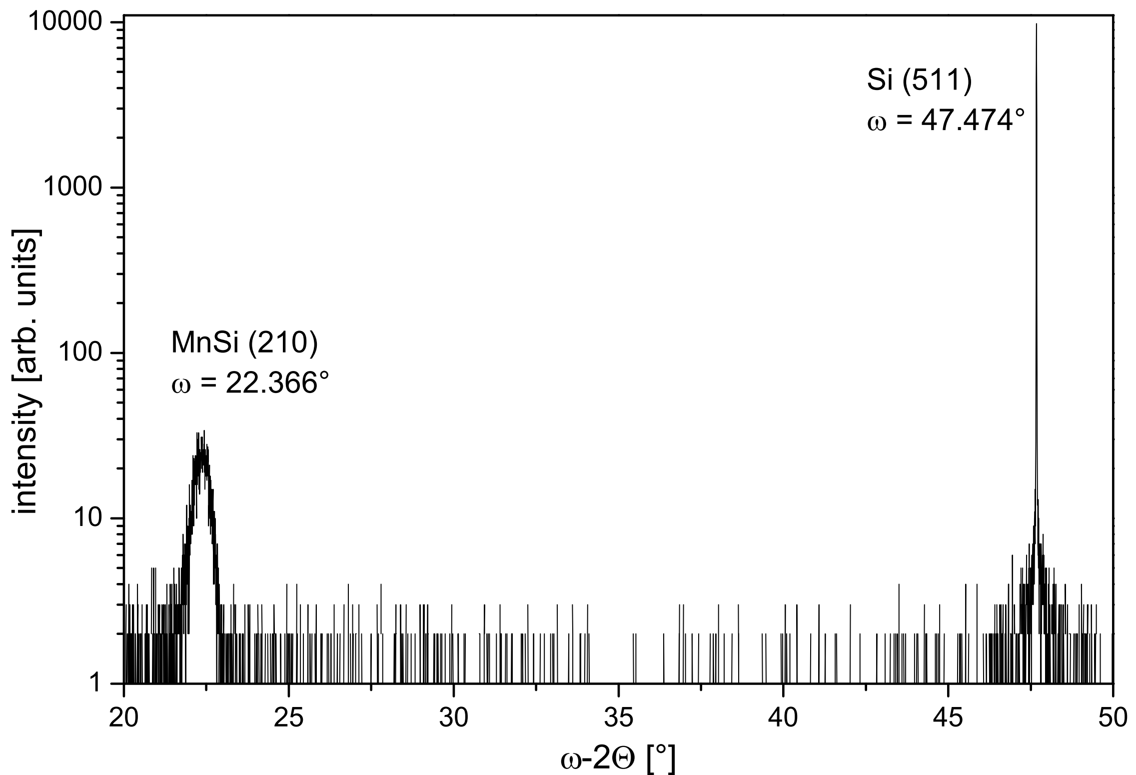

Figure 4.13: ω-2Θ-scan of MnSi (210) reflection. Under the same inclination ψ and rotation φ, but very different ω-2Θ, the Si(511) reflection is observed.

The measured out-of-plane lattice constant is -0.33 % smaller, and the in-plane lattice constant is 0.28 % larger than the literature value. The cause could be residual strain that is not completely relaxed, or the difference in thermal expansion coefficient of MnSi, and Si could induce strain into the layer after growth. The measured residual strain, in-plane and out-of-plane, is in the same order as reported by Karhu et al. for MnSi films grown by MBE [Kar12a]. Quantitative studies on the behavior of strain in thin film MnSi are rare and those existing have not found general principles of the behavior. Therefore, the analysis of the in-plane stress can not be done with confidence with XRD measurements only. Furthermore, the lattice constant of MnSi is not as precisely determined as the Si one; there are publications using various values, e.g. Schwinge et al. [Sch05]. Theoretical calculations even predict lattice constants about 1 % smaller than those experimentally observed [Hor06].

AFM

Surface analysis of the MnSi films is performed ex situ with AFM. Although only the oxidized Si surface can be observed, the morphological information can partially be traced back to the MnSi layer. The surface in Figure 4.14 shows a sample with 17.9 nm MnSi capped with 5 nm single crystalline silicon. The scan shows islands on the surface and five protrusions; three at the bottom, one in the upper right corner and one a little right of the center. These protrusions have a height of 5-7 nm above their surroundings. The islands are 2-3 nm above their surrounding area and are elliptical in form. The preferred orientation of the islands is remarkable. All elliptical islands are oriented approximately 30° off the $[\bar{1}10]$-direction; this is the $[\bar{1}2\bar{1}]$-direction. The latter coincides with the $[\bar{1}10]$-direction of MnSi(111) grown on Si(111) [Sut09].

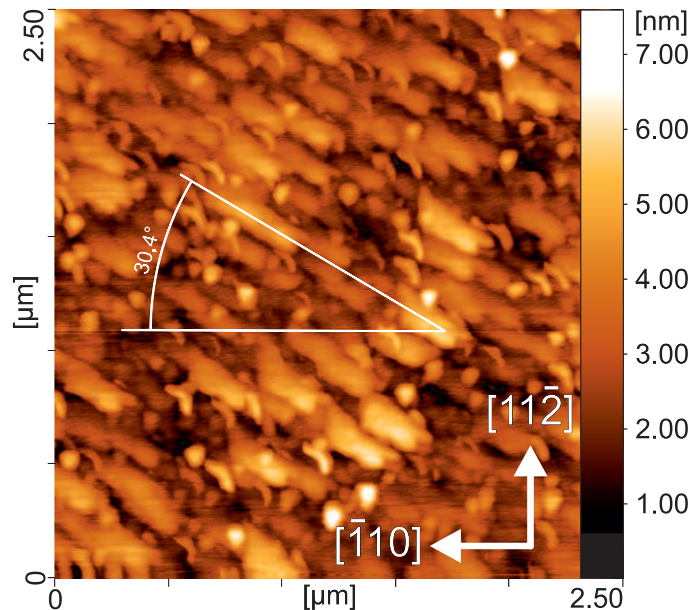

Figure 4.14: AFM scan of the surface of a 17.9 nm MnSi layer capped with c-Si. The orientation of the islands is striking. The direction is $[\bar{1}2\bar{1}]$.

Raman Spectroscopy

Raman spectroscopy is performed on selected samples of MBE grown MnSi. Franziska Fuchs from Experimentelle Physik 6 at the University of Wuerzburg carried out the Raman measurements. The objective is confirmation of the growth of single crystalline MnSi and to probe the different cap types, amorphous and single crystalline silicon. Setup of the measurement consists of a 532 nm, 100mW laser, a microscope with 50×magnification, a notch filter and a grating with 1800 groves per millimeter. On the sample surface the

laser power is focused on 1 µm^2, this results in an intensity of approximately $2 \times 10^6 \frac{\mathrm{W}}{\mathrm{cm}^2}$. Because of the metallic nature of MnSi the penetration depth is assumed to be very limited, but no references are available for MnSi thin films. Figure 4.15 and 4.16 show the Raman spectra of three samples, one with 20 nm MnSi and 8 nm a-Si cap, one with 60 nm MnSi and 7 nm a-Si cap, and another with 17 nm and a 5 nm c-Si cap. For these measurements the parameters are: 5 s exposition and 10 times accumulation. In Figure 4.15, between 100 cm^{-1} and 180 cm^{-1} several peaks are observed, these are caused by nitrogen rotational modes. This is common for Raman spectroscopy on air at high intensities [HSM85; Mar93].

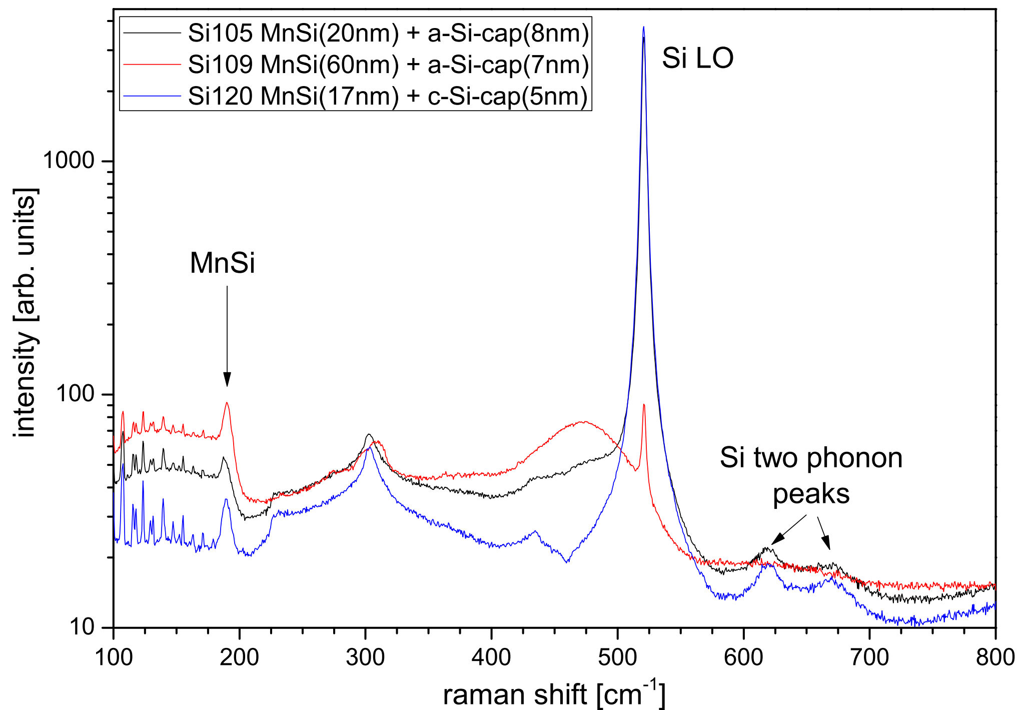

Figure 4.15: Raman spectra of MnSi films. All samples show the MnSi peak at 189 cm^{-1}. The samples with a thin MnSi layer exhibit a clear Si LO peak. For the thick sample the peak is orders of magnitude smaller.

At $\sim$ 189 cm^{-1} each sample exhibits a peak, which is similar in form and relative intensity for all samples. Tite et al. assign two modes of MnSi to this peak, with a shift of 1-2 cm^{-1} [Tit10]. Although the report is on bulk single crystalline MnSi in B20 structure, there is no indication that the Raman spectra for MnSi thin films are largely different. Therefore, this peak is identified as a MnSi peak, confirming the hitherto existing analysis.

In the spectrum in Figure 4.15 the Si one-phonon peak is the most prominent feature, at 521 cm^{-1}. The difference in intensity of that peak between the samples with a thin MnSi

layer and the one with a very thick layer is striking. For the thick sample (Si109) the MnSi layer is obviously thick enough, that almost none of the laser stimulation reaches the Si substrate and therefore the Si one phonon peak is weak. This is confirmed by the absence of the two Si two-phonon peaks at 621 cm^{-1} and 669 cm^{-1}. Another distinct c-Si feature, the drop of intensity at 231 cm^{-1} (Si-TA(L)), is not visible in the spectra. Furthermore, the amorphous-Si band between 420 cm^{-1} and 500 cm^{-1} is very prominent in this sample. Whereas, the Si105 sample shows only some features of a-Si and in the spectra of Si120 they are completely absent. The background intensity, below 200 cm^{-1}, caused by a-Si [Smi71] is not visible in Si120 but in the other two samples. The differences can be directly related to the cap type, Si105 has an amorphous cap, whereas Si120 a c-Si cap.

In Figure 4.16 the spectral range between 176 cm^{-1} and 550 cm^{-1} is presented in more detail. Here, it is obvious that the form of the spectra of Si120 resembles the spectra of c-Si (compare Figure 5.32b on page 102). At around 308 cm^{-1} all samples exhibit a clear peak, for Si105 and Si120 it is at the same position, for Si109 it is at higher values and consists of two peaks. Tite et al. have reported a MnSi peak at $\sim$ 310 cm^{-1} [Tit10] and Si has the peak of the 2TA(X) at 302 cm^{-1}. For sample Si109 both components are distinguishable and the MnSi peak is the dominant one, whereas for Si105 and Si120 both peaks could not be separated. This is most likely because the Si 2TA(X) mode is stronger in c-Si than in a-Si, so in these two samples the Si peak prevails.

In their report about Raman on bulk MnSi, Tite et al. observed that strong laser irradiation changes the sample and partially destroys the MnSi, and other manganese silicide phases form [Tit10]. The intensity of the setup used is in the same order of magnitude, but no changes in the spectra of the samples, after irradiation, are observed. This can be attributed to the Si cap which protects the MnSi not only from oxidation but, due to its high thermal conductivity, from the consequences of the irradiation as well.

The observed peak at $\sim$ 189 cm^{-1} is a clear indication for MnSi in cubic B20 structure, as reported by Tite et al. [Tit10]. At 310 cm^{-1} the MnSi peak is superimposed by the Si 2TA(X) mode (302 cm^{-1}). For all samples the Si 2TA(X) peak is shifted to higher values indicating the MnSi peak is present, but could not be resolved. The almost total absence of c-Si features in the spectra of Si109 leads to the conclusion that $\sim$ 60 nm of MnSi is enough, so that no signal from the c-Si substrate reaches the detector.

The Raman analysis shows that the single crystalline overgrowth of MnSi is successful. Features of a-Si are not present in the spectra of the sample with a c-Si cap, and the c-Si features are more pronounced than in both other samples.

Magneto-Transport and SQUID

As a first test of the material the transport group of EP3 fabricated a Hall-bar from a 20 nm MnSi layer, with optical lithography methods. Etching of the sample is done with

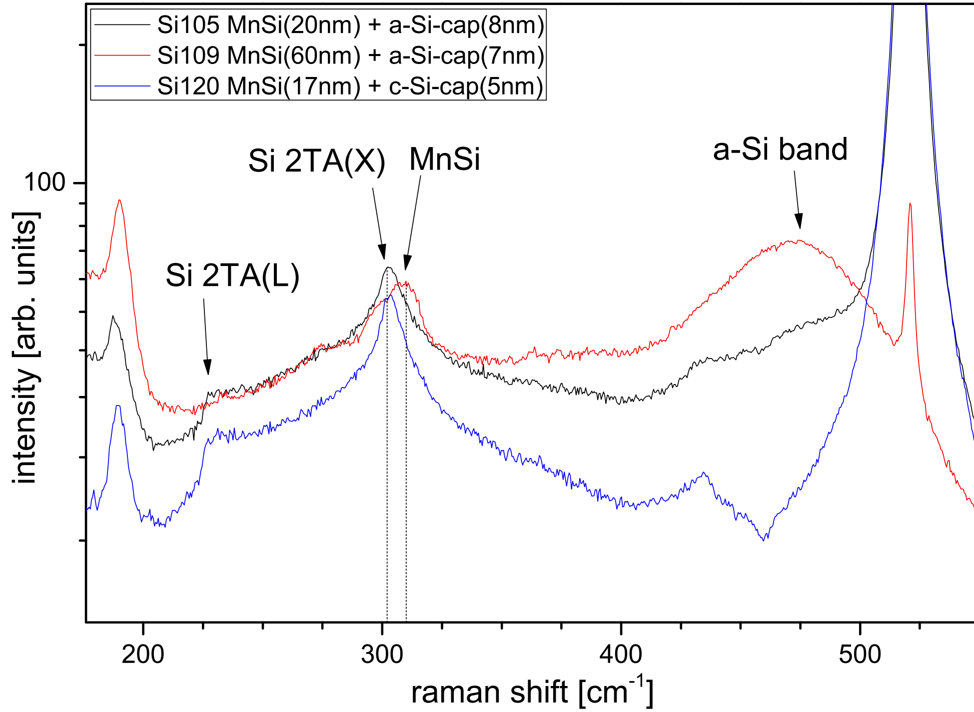

Figure 4.16: Detailed view of the MnSi Raman spectra. The peak between 300 $cm^{-1}$and 320 cm^{-1}consists of the Si 2TA(X) at 302 cm^{-1} and a MnSi peak at $\sim$ 310 cm^{-1}. The thin samples show the typical spectra of crystalline Si, the thick sample of amorphous Si.

chemically assisted ion beam etching. The fabricated structure is inserted in a cryostat and cooled with liquid helium. In order to measure the magneto-transport properties, the cryostat is equipped with a 300 mT vector magnet.

In Figure 4.17a the DC resistivity is plotted versus temperature, between 4 K and 120 K. Fitting of the data is performed following the evaluation of Mena et al. on MnSi [Men03]. At about 40 K the resistivity changes its dependence on temperature (gray colored area in Figure 4.17a). In the temperature regions below and above that area, different temperature dependence is observed. In the range above ~40 K the data is fitted with a parallel resistor formula [Wie77] $\rho_p(T) = [1/\rho_\infty + 1/(\rho' T)]^{-1}$, (green curve) from the fit $\rho_\infty = 565\,\mu\Omega$cm is determined. This indicates metallic behavior. In the range below 40 K, the temperature-dependent resistivity is fitted with the equation $\rho(T) = \rho(0) + AT^\mu$ (red curve). The extracted parameters are $\rho(0) = 83.1\,\mu\Omega$cm, $A = 0.11\,\mu\Omega\mathrm{cm\,K}^{-2}$ and $\mu = 2.0$. With the exponent $\mu = 2.0$, in this temperature region, the resistivity shows a T^2-dependence. According to Moriya, a helimagnetic phase should exhibit T^2-dependence, caused by coupling of the charge carriers to spin fluctuations [Mor85].

Figure 4.17b shows the magneto-resistance of the Hall-bar. The magnetic field was aligned

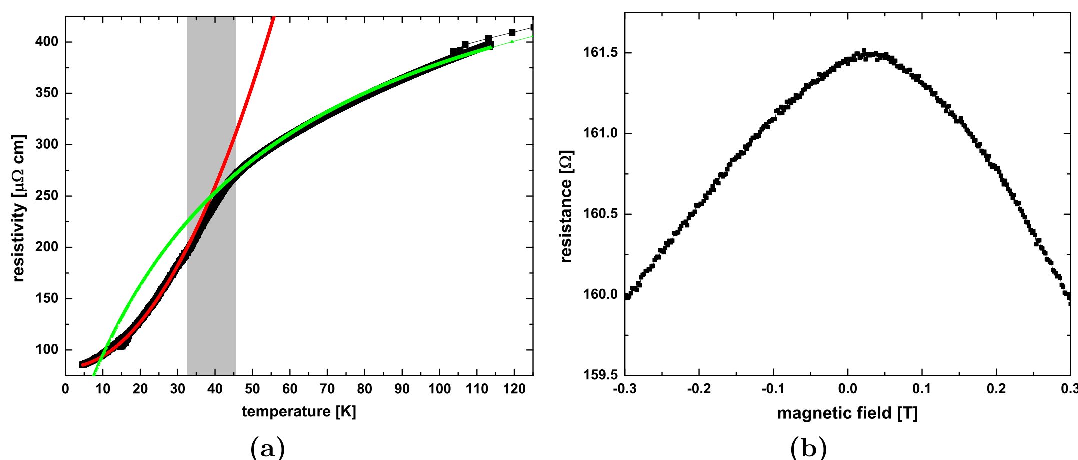

Figure 4.17: (a) DC resistivity as a function of temperature, between 4 K and 120 K. In the gray colored area, the resistance changes dependency on temperature. The red and green fitting curves are used following [Men03]. (b) Four terminal magneto-resistance curve for a fabricated Hall-bar. B-field is aligned ±10° along the $[\bar{1}10]$-direction of MnSi.

in plane, along the $[\bar{1}10]$-direction of MnSi; the error of the alignment is estimated to be less than ±10°. The magneto resistance of the device is 0.9% at 300 mT. This is rather large, even when compared to ferromagnetic metals.

Figure 4.18 shows the resistivity for a magnetic field sweep of $\phi = 0$ to 360°, with the rotation axis being parallel to [111]. The radial scale is the percentage difference of the minimal resistivity. The resistivity is measured in a four terminal geometry. Prior to the scan, the sample is saturated in the magnetic field for 30 minutes. For $\phi = 0°$ the magnetic field is aligned along $[\bar{2}\bar{1}3]$. This unusual alignment is caused by a 45° offset of the Hall-bar used for measurement. The total alignment error is ±10°, caused by the error during the lithography process and the alignment in the cryostat. For the red curve the sample was rotated a total of 1402° and for the black 628°. The measurement shows an anisotropic magnetoresistance for this sample. In the graph, the two dashed lines will be used as a guide for the eyes to identify the hard and easy axis. The easy axis in the measurement appears at a magnetic field rotation of about 20°. Considering the error in alignment of the sample, the easy axis appears to coincide with the $[\bar{1}01]$-direction. The hard axis appears at approximately 110°, which is close to the $[\bar{1}2\bar{1}]$-direction.

An unusual, memory-effect like, behavior at the start of the measurements is observed. The resistance is considerably higher at the beginning and does not reach these values during the measurement again. The measurement starting at 90° reaches the normal resistivity after approximately 90°, whereas the measurement starting at $\phi = 0°$ reaches normal after approximately 180°. Peculiarly, for both measurements the resistivity reaches

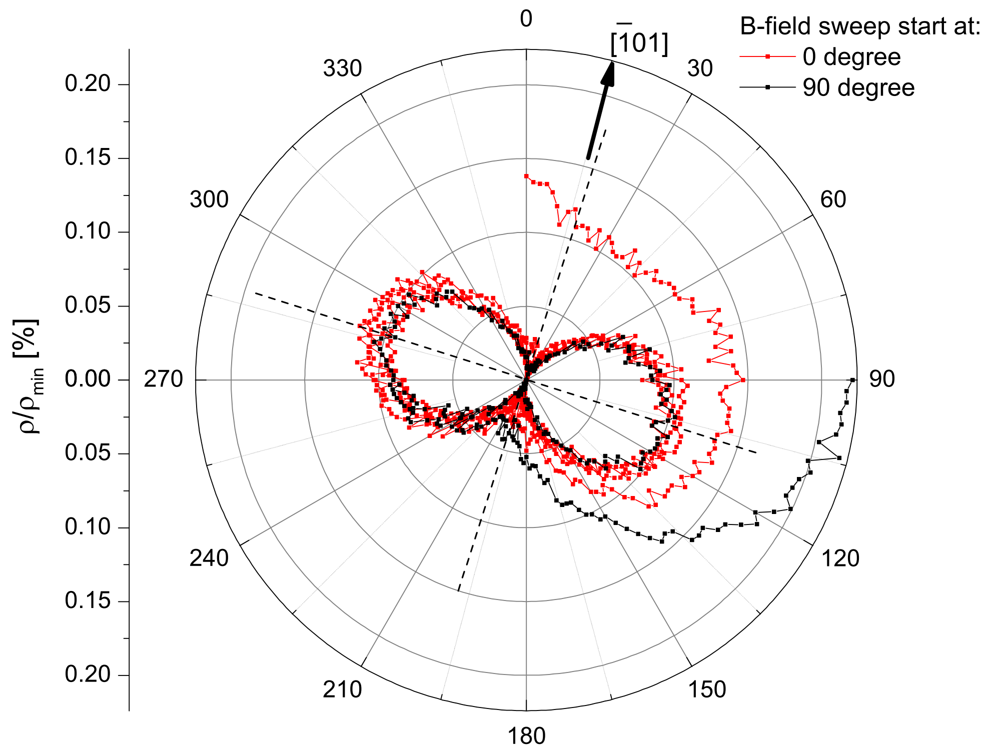

Figure 4.18: Resistance in dependence of an in-plane sweep of the B-field (300 mT). Prior to scan the sample is saturated for 30 minutes in the magnetic field. For $\phi = 0°$ the B-field is aligned along $[\overline{2}\overline{1}3]$.

the normal value for $190 < \phi < 210°$, very close to the $[10\bar{1}]$-direction. For now, there is no indication as to what is the reason for this effect.

Using a superconducting quantum interference device (SQUID) the magnetization of a MnSi film is measured on warming the sample in a magnetic field of 400 mT along $[1\bar{1}0]$-direction of MnSi. The magnetization shows a significant drop at temperatures above 30 K (Fig. 4.19b). For thinner MnSi films, the drop appears to be at higher temperatures. Karhu et al. assign a Curie temperature to this drop, but the direct relation to the Curie temperature is not generally established [Kar10; Kar12b]. However, the presented observations of the temperature-dependent magnetization behavior are in agreement with the data reported by Karhu et al. and Magnano et al. Both groups attribute the features in the measurement to the properties of MnSi thin films [Kar10; Mag10].

Figure 4.19a shows the hysteresis loops collected at 5 K, for two samples with 12 nm and 20 nm MnSi. For the 20 nm layer (black curve) the magnetization increases almost linearly from 0.025 T up to 0.42 T. Above that, the magnetization increases rapidly until

it saturates above $\sim 0.6\,\mathrm{T}$ (termed "first-order-like jump" by Karhu et al.). The hysteresis curve of the 12 nm sample shows a quite different behavior: the increase has no linear region and saturation is reached with a large curvature. This peculiar behavior is observed and reported by Karhu et al. for MnSi thin films. They propose a relation between the occurrence of the first-order-like jump and the layer thickness being in the order of the wavelength of the helimagnetic order ($2\pi/Q = 18\,\mathrm{nm}$).

Magnano et al. also observe the linear behavior of the magnetization. They assign the two transitions in behavior to the transitions from helical to conical phase, and from conical to ferromagnetic phase [Mag10].

Furthermore, at low fields an opening in the magnetization curve is observed (see inset in Figure 4.19a). The observed remnant magnetization and coercitive force of the sample are in the same order as the data reported by Karhu et al. and Magnano et al. [Kar10; Kar12a; Mag10]. The in-plane remnant magnetization can be explained by the uncompensated moments of the helimagnetic order when the film thickness is not an integer multiple of the helical wavelength [Kar12a].

The preliminary measurements of the transport and magnetic properties are in agreement with reported properties that are frequently assigned to thin film single crystal MnSi.

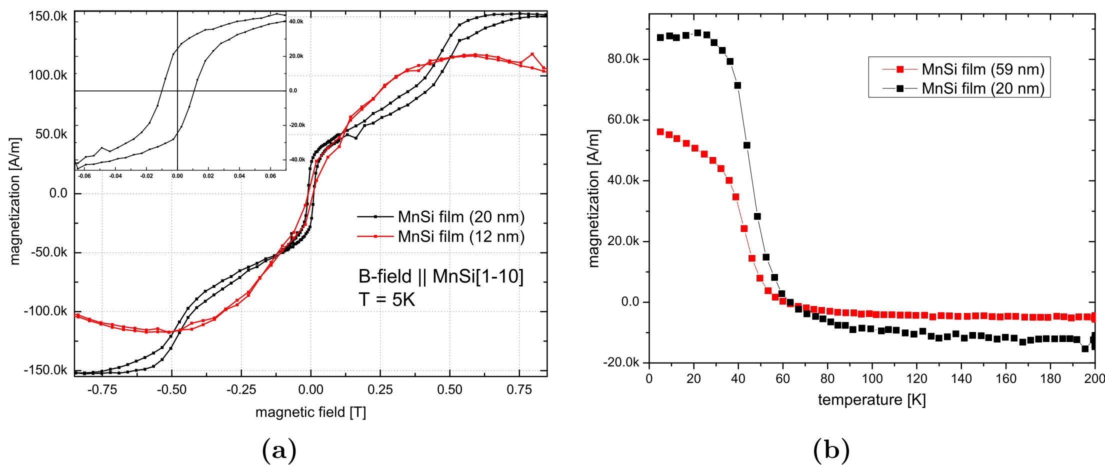

Figure 4.19: SQUID data of a 20 nm MnSi film. (a) Magnetization curve measured with B-field along $[1\bar{1}0]$-direction of MnSi at 5 K. The inset shows the magnetization curve between -0.07 T and 0.07 T. (b) Field-warmed magnetization curve with magnetic field of 400 mT along $[1\bar{1}0]$-direction of MnSi. Above 30 K a drop of the magnetization is observed.

4.2.3 Discussion

For MBE growth of MnSi on Si(111) the preparation of the wetting layer on the wafer is very important. Without the wetting layer or with a low quality wetting layer the growth is bound to transform into 3D or amorphous growth. With RHEED, no difference after annealing is observed for wetting layer coverage between 2.8 ML and 5.8 ML. Differences in the surface morphology depending on the coverage, reported by Kumar et al., are too small to be observed with RHEED [Kum04]. However, the transition from amorphous surface to ordered surface is clearly visible and indicates the lower limit of substrate temperature (T_{sub}= 330°C) for MnSi layer growth. In order to achieve MnSi film growth on the wetting layer the Mn and Si fluxes have to be equal at the substrate surface. If not, Mn rich or Si rich phases grow. Further improvements on the layer quality could be made by monitoring both fluxes in situ, to be able to adjust to changes. After film growth a cap layer has to be grown to be able to analyze the film ex situ or to process the film further. An amorphous cap layer provides sufficient protection against oxidation. However, further crystalline growth is not possible on amorphous Si; therefore a c-Si cap is grown over the MnSi layer. Observations with RHEED show epitaxial growth of Si on the MnSi film, although the growth mode is not a layer-by-layer mode. Three dimensional features observed with RHEED suggest some island formation after about 4 ML, but within the growth of 8 nm the features are stable and not getting stronger. This hints that under the right conditions the surface might be smoothed out, in analogy to the SiO_x layers presented in Chapter 5.

Determination of layer thickness is performed with XRR. The results are in good agreement with the thickness evaluated from the XRD ω-2Θ-scans. In the scans the MnSi peaks are identified and the corresponding lattice plane spacing is calculated. The results show a deviation of -0.32 % for out-of-plane and 0.28 % for in-plane from the literature value for bulk MnSi. The reason for that could be residual strain in the layers close to the interface. On the other hand, the discrepancy of the linear thermal expansion coefficient could cause stress in the layer when the sample is cooled down from growth temperature. The thermal expansion coefficient of MnSi is five times larger than that of Si, at these temperatures [ZS61]. Additionally, it should be noted that the reported variations of the literature value for MnSi would change the measured strain up to 18 % (from 0.32 % to 0.26 %).

The observed twinning of the layer could be caused by misorientation at the growth start, when the MnSi surface unit cell is turned 30° in respect to the Si surface unit cell to minimize lattice mismatch. Rotation of 30° in the opposite direction could cause the twinning. Apart from that, the twin boundary belongs to the same set of lattice planes as the mirror plane for the transformation from right handed to left handed chirality. This could be an indication that the twins are crystallites of different chirality. Furthermore, mosaicity twist is observed in the MnSi layer; this might also be caused by twinned crystal areas. The transition from one area to the other could cause misalignment, observed as

mosaicity twist.

Kumar et al. have shown that the strain relaxation causes a dislocation network at the interface [Kum04]. This is probably one reason for the observed shoulders in the ω-scan of the MnSi peak; other possibilities are interface roughness, mosaicity tilt and finite crystallite size. From the measurements it is not possible to conclude which mechanism causes the peak broadening.

The surface of the MnSi layer shows islands with a preferred direction along the $[\bar{1}2\bar{1}]$-direction for the Si in AFM. This coincides with the $[\bar{1}10]$-direction of MnSi [Sut09] because of the rotation of the surface unit cells to reduce the lattice mismatch. Suto et al. also observed protrusions on thick MnSi layers, similar to those observed here, and suggested the formation is related to the reduction of the surface energy. The formation of the islands could be caused by c-Si overgrowth or might stem from the MnSi growth. However, the MnSi growth showed no 3D features in RHEED, whereas the c-Si cap showed 3D features. Further investigations are necessary to determine in which layer the islands are formed.

4.3 Summary

MnSi is a material containing a great deal of promise for basic research as well as for the development of devices for spintronics. MnSi thin films have in general the same properties as bulk MnSi [Mag10], although slight deviations in the Curie temperature and the magnetic moments occur [Wu04; Hor08]. The crystallographic properties are the same as for bulk MnSi, except for the tensile strain induced by the mismatch to the substrate. Although the exact characteristics of the strain in the film have not yet been fully understood, most of the strain is released through dislocations at the interface [Kar10] within a few mono layers of MnSi [Kum04]. Fabrication of MnSi thin films is best performed with MBE, because the film thickness can be controlled precisely. Furthermore, to grow films without holes created by the silicide reaction, Mn and Si have to be provided [HKT09], temperature control for the annealing is very important and RHEED is required to observe the process. All the above is combined in MBE. The results presented show that the growth control achieved by MBE is superior to other techniques, such as SPE. With precise flux control, MnSi can be grown up to 60 nm thickness and further improvements, like permanent in situ flux measurement, could help to improve the samples even more. Analysis of the samples with XRD showed that the grown layers are MnSi(111) on Si(111); the crystalline quality is good. Broadening of the ω-scans is observed, but the exact cause could not be determined. Detailed examinations of the crystal structure, with TEM, are necessary to identify the cause and improve the growth process. With Raman measurements MnSi thin films can be probed and the material can be identified. But the influence on the spectra of different phases in the layer has not been studied, yet.

Preliminary magneto-resistance and SQUID measurements of the MnSi MBE samples have shown results that are in agreement with the published data for MnSi thin films.

Chapter 5

SiO_x Growth and Characterization

Silicon suboxide is present at Si/SiO_2 interfaces, and studies on SiO_x are mainly based on single interfaces between c-Si and a-SiO_2. The overgrowth of SiO_x with c-Si with MBE has been shown by Sticht et. al [Sti02a] but was restricted to a single SiO_x layer. This chapter starts with the growth methods and overgrowth parameters of single SiO_x layers and the conclusions that are drawn from the characterization. Thereafter comes the growth and characterization of SiO_x multilayer structures. This part includes the development of models to simulate the XRD of the multilayer structures. Furthermore the optimization of the growth parameters for the multilayer structures is described. The chapter finishes with a summary that includes the important findings, a discussion and future prospects for SiO_x growth.

5.1 Growth and Crystalline Overgrowth of Single SiO_x layer

Prior to growth, the wafers are prepared as described in section 3.1; a silicon buffer layer is grown to ensure identical conditions for all samples. During the silicon layer growth only silicon and optional doping source shutters are open. Transition to oxide layer growth is executed without interruptions. This means that the silicon and doping source shutters close the same moment the oxygen valve opens. In Figure 5.1 the development of the chamber pressure and shutter sequence for a SiO_x layer is shown. The ion gauge used to measure the chamber pressure is situated behind the LN_2 cooling shroud and thus is slow to react. At the substrate the O_2 pressure can be assumed to be abrupt and stable over time. Readings of the pressure gauge are taken 30 seconds after the opening of the valve (unless indicated otherwise) so that the readings can be compared and the pressure gauge has established a stable read-out. The measured pressure can be seen as the oxygen partial pressure because the background pressure before and after oxygen inlet is two orders of magnitude smaller.

After oxygen is let into the chamber, a ten-second break in the growth process is added. This is to make sure as little as possible residual oxygen remains in the growth chamber

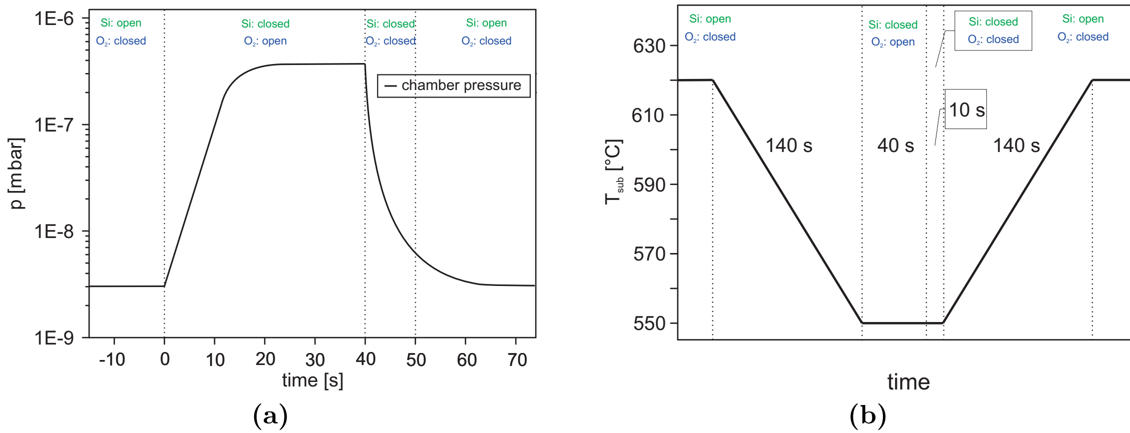

Figure 5.1: (a) Development of the chamber pressure during a SiO_x layer growth (oxide spike growth). The shutter status of silicon and oxygen source are indicated. Zero on the time axis is set to the oxygen valve opening. (b) Course of $T_{sub}$for one oxide spike. $T_{sub}$is lowered and stabilized before the spike and raised again after the ten-second pumping time.

when silicon growth resumes. Once silicon growth is resumed, the background pressure at this point is usually already lower than $1{\times}10^{-8}$ mbar, meaning that good conditions for crystal growth are established throughout the complete silicon layer growth time. This growth method is referred to as "spike" growth in contrast to "co-deposition", in which silicon growth is continued while the oxygen source is open.

5.1.1 RHEED Observations

RHEED observations of the growth process are of particular interest to develop a model for the growth of SiO_x layer. Starting with the Si buffer layer, a 2×1 reconstruction of the silicon (001) surface is clearly visible and it is proof of monocrystalline two-dimensional growth of silicon (see Figure 5.2 (a) beam incident <011> and (b) 45° beam incident <010>). Picture 5.2 (c) is taken during the oxygen spike. The streaks of the 2×1 reconstruction are hardly visible anymore. If the oxygen exposure is long enough, the RHEED image resembles that from a silicon wafer with its native oxide. This suggests that the surface has lost its order. The pictures (d) to (f) are taken during overgrowth with silicon - 50 seconds, 85 seconds and 120 seconds, respectively, after the oxygen spike. They show the development of the surface to a three-dimensional growth mode after the oxygen spike.

In the process of Si layer growth the three-dimensional features become prominent in the first 120 s after the oxide spike. After that time, the RHEED pattern does not change recognizably for the next five to ten minutes (depending on the growth parameters). A

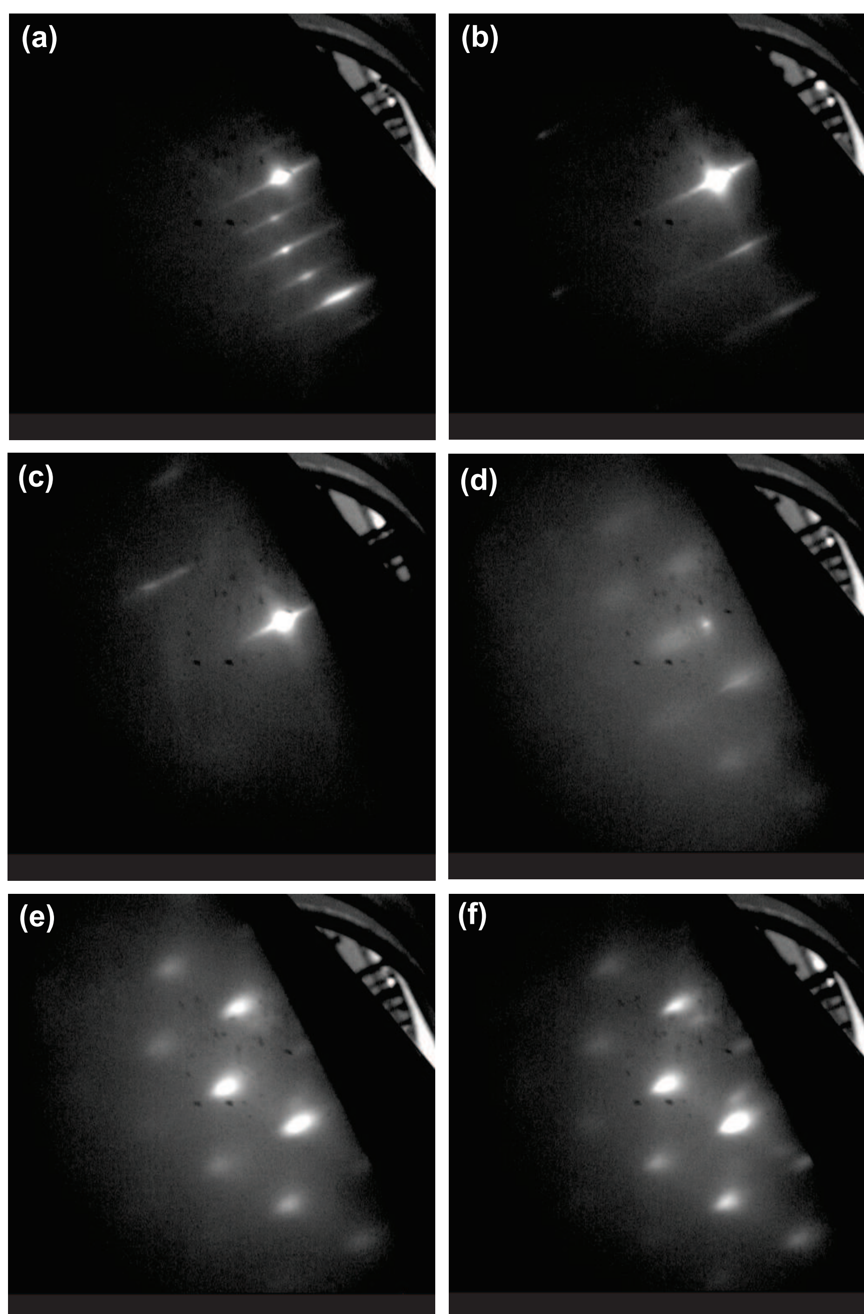

Figure 5.2: Photographs taken of the RHEED screen during a SiO_x spike growth. In (a) <011> direction the clean and flat 2×1 reconstruction of the silicon buffer layer is visible, (b) is in <010> direction. (c) During the SiO_x layer, the reconstruction is hardly visible anymore. The pictures (d), (e) and (f) were taken 50s, 85s and 120s, respectively, after the oxygen valve was closed.

smooth transition from the three-dimensional pattern towards a two-dimensional pattern makes it hard to determine the exact times. However, after some time very light streaks become visible on the three-dimensional RHEED pattern. This marks the start of the transition from 3D to 2D. After some time, the RHEED pattern is back to a perfect two-dimensional pattern, indicating a layer by layer growth of the Si layer. Figure 5.3 shows the surface reconstruction of the sample in Figure 5.2 after 40 nm silicon layer growth. Spotty features are replaced by streaks from a smooth 2×1 silicon reconstruction.

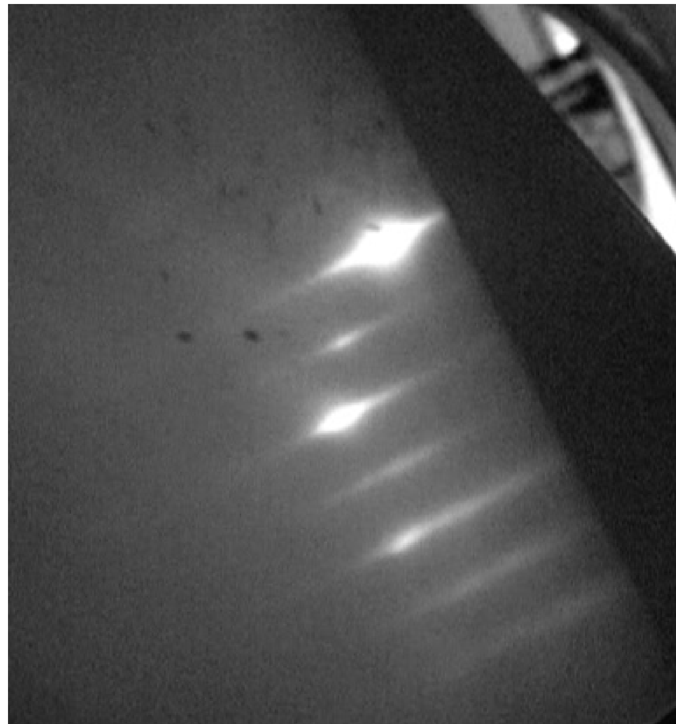

Figure 5.3: RHEED pattern of the same sample as in Figure 5.2. The Si layer over the SiO_x layer is now 40 nm thick. The surface shows a 2D 2×1 Si reconstruction.

5.1.2 Verification of Surface Roughness

RHEED images are very reliable in respect to the growth mode and the surface ordering, but to determine the real surface roughness further measurements are needed. Ideally, scanning tunneling microscopy or scanning electron microscopy would be used in situ to investigate the surface of the growing oxide spike. In situ STM or SEM facilities are not available at the MBE to measure the samples, so the samples have to be taken out of vacuum for measuring. Surface analysis is performed with atomic force microscopy. The

samples are analyzed directly after they are taken out of vacuum to avoid dust particles settling on the surface, interfering with the measurement.

Exposure to air causes the sample surface to oxidize, so the AFM image does not show the original, but the oxidized, surface. Nevertheless, it is possible to draw conclusions from the AFM analysis about the surface morphology. In particular, the comparison between the samples is a reliable source of information on the growth mechanism of silicon suboxide layers.

All layer growth starts with the buffer layer that is supposed to smooth the surface after deoxidation; hence, a wafer with a native oxide layer is compared with a sample with only a buffer layer grown Fig. 5.4.

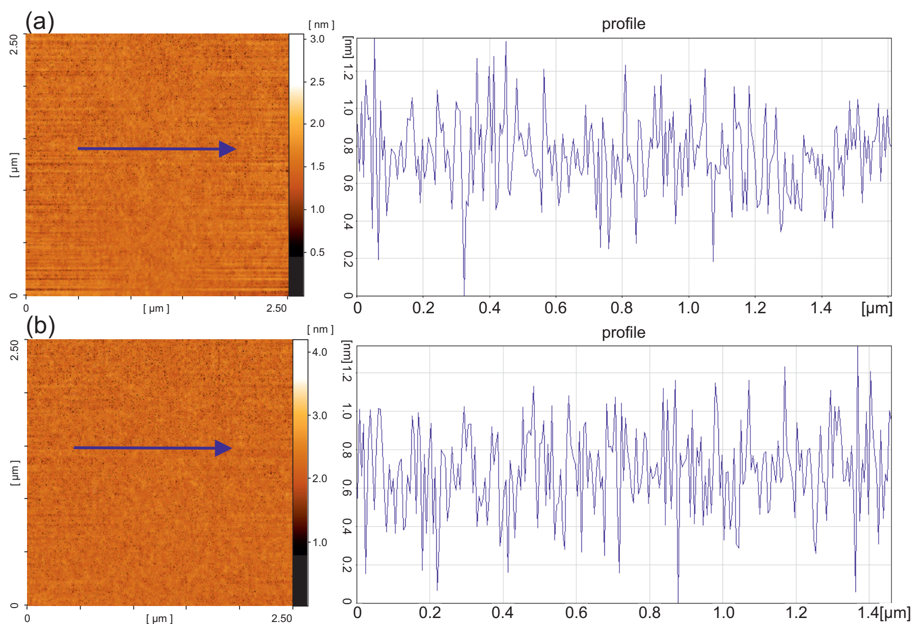

Figure 5.4: AFM scan (2.5 μm×2.5 μm) comparison of (a) a wafer with native oxide and (b) a MBE grown buffer layer oxidized on air. RMS of the oxidized buffer layer is slightly larger (128 pm) than that of the native oxide. The line scan shows no distinguishable features, as is expected for a naturally oxidized surface. The surfaces are practically identical.

The two surfaces—wafer with native oxide (a) and oxidized buffer layer (b)—are homogeneous and the RMS of the oxidized buffer layer is 128 pm larger than that of the native oxide. That difference can be explained with a few very high data points. Because in the RMS the square of the values is used, larger values have a larger impact (see section 3.5). When the low points of the profiles are compared, it is obvious that both surfaces are smooth as they lie in a narrow z-range. The buffer layer exhibits only a marginally less smooth surface than the native oxide of the wafer, and no growth defects are observed. For both samples the height distribution is Gaussian and symmetric, as is expected for an

amorphous, naturally oxidized surface. Surface roughness of both samples is calculated following equation 3.13. The native wafer has a RMS of 315 pm and the MBE grown buffer layer 443 pm. Still, a buffer layer needs to be grown to bury impurities that may remain from oxide removal and guarantee identical conditions for each SiO_x layer.

To verify the RHEED observations, several oxide spike samples are grown, but the growth process is aborted at different stages of growth. All samples of this series are grown with the same parameters: i.e. substrate temperature (T_{sub}) of 620°C for silicon and 550°C for the oxide layer, and oxygen pressure (p_{O_2}) is set to be 1.5×10^{-7} mbar $< p_{O_2} <$ 1.7×10^{-7} mbar. Scanning parameters were equally standardized to a 2.5 µm×2.5 µm scan area with 512×512 points resolution. Three samples are compared, all aborted during Si growth after the oxide layer: the first after 3.2 nm Si growth, the second after 24 nm and the third after 35 nm. When the first sample is aborted, 3D features are well established on the RHEED screen. While at the second sample the RHEED is still mostly 3D, the third sample has strong 2D features with residual 3D features. In Figure 5.5 the scans are shown together with a profile (line scan) of the surface to the right of each scan.

Figure 5.5(a) shows that the surface after 3.2 nm of silicon overgrowth is dominated by small hills separated by valleys of the same dimensions. The height difference between the hills and valleys is about 1 nm, their lateral dimension is about 30 nm and the RMS is calculated to be 465 pm. Subfigure (b) exhibits a different surface morphology: the roughness increased to 2240 pm. The height difference between hills and valleys has increased to 10 nm and the lateral dimension of the features has increased to ∼140 nm. Overgrowth changed the morphology to plateaus separated by valleys. Although hills developed into plateaus, the width of the valleys has not increased.

In Figure 5.5(c), after 35 nm of silicon layer, the hills are joined together into large plateaus. The valleys are still quite deep (up to 7 nm) but the hills have developed into plateaus that cover most of the surface. In this stage the RHEED image is dominated by streaks with a few spots, corresponding to a 2D surface but with some 3D features.

Due to an error in the electronics of the EBE, a multilayer sample was interrupted after the third SiO_x layer. Growth parameters are comparable to the ones from the series above: O_2 pressure is 3.8×10^{-7} and substrate temperature for the SiO_x layer is 550°C. Only the substrate temperature for the silicon growth is raised to 700°C. From the average growth rate of the sample, the thickness of the top silicon layer is determined to be 12.6 nm. Figure 5.6 presents a scan of the surface of this sample. Surface morphology and the line scan show many similarities with the sample in Figure 5.5(c) with 35 nm silicon layer, although the silicon layer is only half as thick. The reason for the enhanced smoothing is the higher substrate temperature for the silicon layer that allows for longer diffusion length of the Si atoms on the surface. The relation between substrate temperature and required layer thickness for overgrowth is the subject of section 5.2.2.

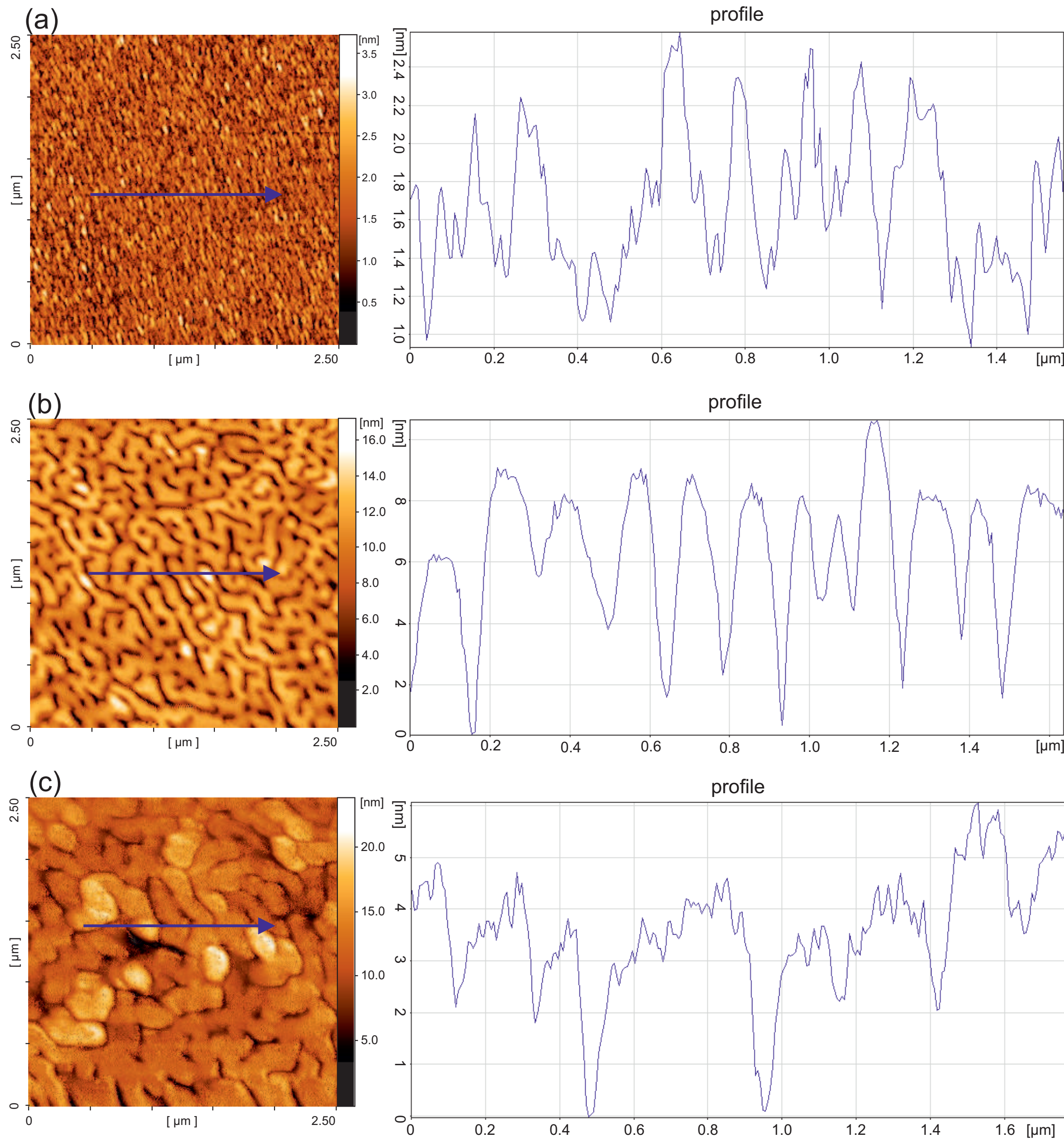

Figure 5.5: AFM scans of samples in different stages of overgrowth of a SiO_x layer. To the right of each scan is a profile, scanned along the red arrow in each scan. (a) has a 3.2 nm Si layer over the oxide spike, (b) has 24 nm of Si grown and (c) 35 nm.
The profiles clarify the overgrowth mechanism. Sparse oxygen regions continue to grow in vertical direction and only later fill the gaps to form a homogeneous layer.

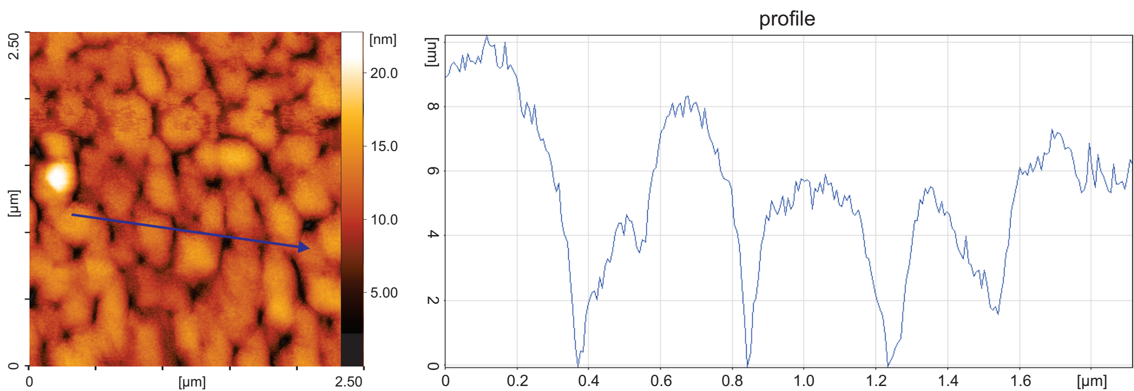

Figure 5.6: AFM image of a sample with 12.6 nm silicon layer grown on top of a SiO_x layer. The substrate temperature for Si is 700°C. RMS is 2570 pm, that is the same as the sample in 5.5(c). The higher T_{Sub} enhances the smoothening of the surfaces, and less overgrowth layer thickness is needed.

5.1.3 XRD and TEM of Single Layers

X-ray diffraction is a standard tool to characterize crystal structures, but analyzing very thin layers creates a problem, because very thin layers do not have sufficient volume to diffract enough x-rays to measure the layer directly. With the x-ray interference method [TP89], it is possible to probe even a single SiO_x layer.

The silicon top and bottom layer are spatially separated and, because of the SiO_x layer between them, the lattice planes of the top layer diffract with a defined phase shift to the lattice planes from the bottom layer. The phase shift of the diffracted waves, from the top and bottom Si layer, causes interference, which can be observed as intensity oscillations in the diffraction pattern. The phase shift depends on the product of strain and thickness of the SiO_x layer. The period of the intensity oscillations depends on the Si top layer thickness. Inhomogeneity of the SiO_x layer causes diffuse scattering, which is not coherent and therefore not capable of diffraction. That is why XRD may probes less oxygen than is actually incorporated in the SiO_x layer. In the diffraction pattern, the oscillations are symmetrical around their zero order. Because of strain in the SiO_x layer, the zero order of the oscillations does not coincide with the Si substrate peak; tensile strain causes a movement of the zero order to larger ω angles.

Figure 5.7 is a XRD ω-2Θ scan of a sample with one SiO_x layer, with a 121 nm Si cap layer on top. During the growth of the cap, the different stages of SiO_x overgrowth (see section 5.1.1) are observed with RHEED, and when growth is terminated, RHEED indicates a perfect two-dimensional surface. The existence of the interference oscillations shows that top and bottom Si layer lattice planes are parallel to each other. This confirms single crystalline overgrowth of SiO_x layer with silicon.

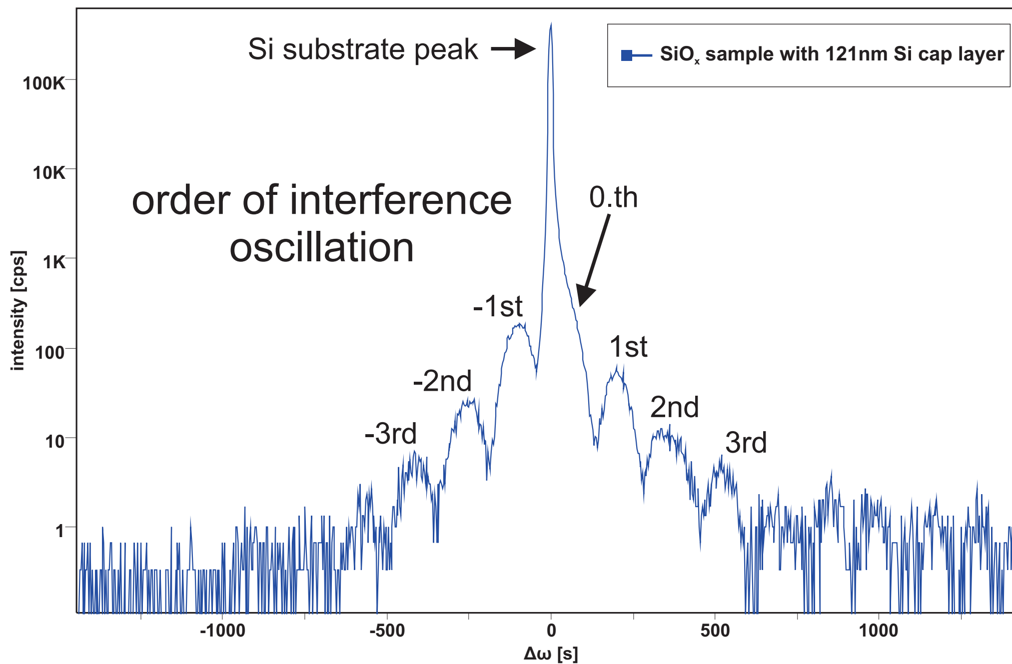

Figure 5.7: XRD ω-2Θ scan of a sample with a single SiO_x layer and a Si cap of 121 nm thickness. Interference oscillations are clearly visible on both sides of the Si(004) peak. The shoulder on the right side of the Si peak is the zero order of the oscillations.

For investigations on a microscopic scale of the Si/SiO_x interface and the crystalline cap layer, a sample has been prepared for transmission electron microscopy. Preparation of the lamella for TEM is performed on a dual beam SEM (FEI Helios Nanolab). The part to be investigated is protected with a Pt layer on the surface from the Ga ions used to mill the sample. This way a lamella with more than 1000 nm thickness is prepared. To enable TEM with high resolution the lamella needs to be thinned down to at least 100 nm, but preferably less than 50 nm. To thin the sample the ion beam is used in several steps, each using ions with less energy to minimize the damaged region of the sample. At the end of the process the lamella is ~42 nm thick. In Figure 5.8 SEM images throughout the preparation process are shown: on the left is the lamella after the first three thinning steps, on the right is the finished lamella with about 42 nm thickness (top view).

The sample used for the TEM images is grown with the following parameters: substrate temperature for the silicon layer is 620°C and for the oxide spike 550°C, oxygen pressure during the oxide spike is 2.0×10^{-7} mbar and duration is 45 seconds. Presented in Figure 5.9 are two STEM images along the $[1\bar{1}0]$-direction of an oxide spike layer. On the left is an overview image from which the average thickness of an oxide layer can be evaluated to about 1 nm. Uncertainty of about 0.5 nm remains because of the variation of the thickness and the not always easily distinguishable interface between silicon and oxide. The STEM

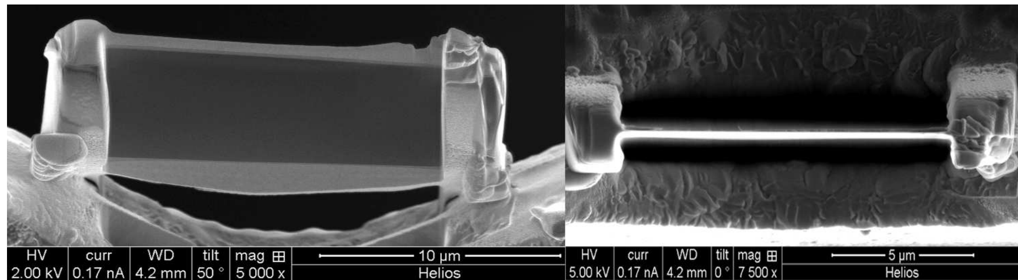

Figure 5.8: SEM images of the TEM lamella during processing. Left: Lamella attached to holding grid after the first thinning steps, thickness 271 nm. Right: End of processing. Lamella from the top, thickness ∼42 nm.

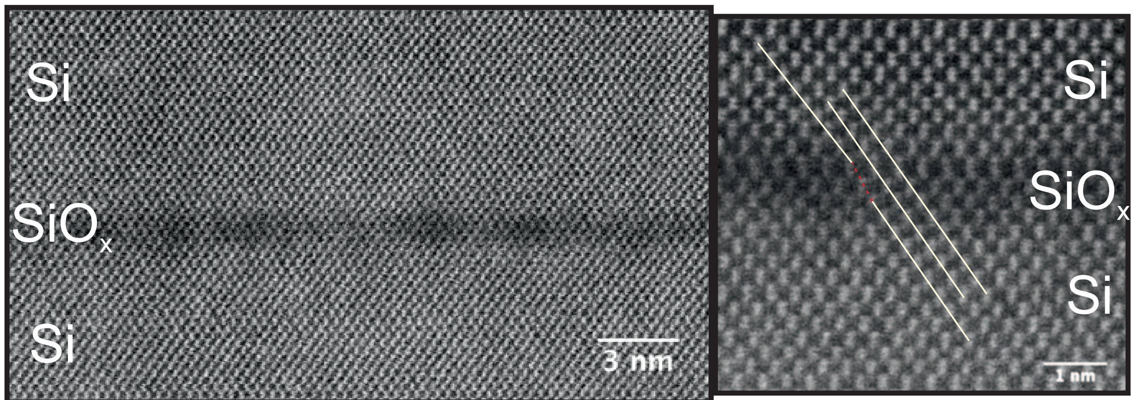

Figure 5.9: STEM images of a SiO_x sample. Left: Image of a SiO_x layer: the average thickness of the layer can be evaluated to ∼1 nm. Right: Detailed image of the SiO_x layer. In the Si rich environment of the SiO_x layer, the crystal information is seeded to the top layer.

images are taken in Z-contrast mode, so the image contains information on the atomic weight. The heavier an atom, the larger is the electron number Z, the stronger is the scattering and thus the brighter the image. In conclusion, the darker parts of the images represent areas with higher oxygen content: the brighter parts are silicon-rich areas. On the right side is a detailed image of the oxide layer. Here, as well as in the other image, it is visible that the brightness of the oxide layer changes in lateral direction. Areas with the same brightness only stretch out for two—or a maximum of three—nanometers, but most areas are smaller than that. This means that the variation in oxygen density is quite large and happens on a small length scale. Furthermore, it seems that the Si planes going through a Si rich area are perfect lattice planes, whereas individual planes going through oxygen-rich areas are slightly distorted. This indicates some kind of strain in the oxygen-rich areas. Nonetheless, the vast majority of lattice planes is undistorted and therefore single crystalline.

5.1.4 Qualitative Model of $Si/SiO_x/Si$ Growth

Based on the measurements presented in the sections above, the growth of SiO_x layer and their crystalline overgrowth can be explained. Formation of the oxide and the crystalline overgrowth has been under investigation by Wei et. al [WWS97] and their model will be used here. A key assumption for the model is that oxygen coverage on the wafer surface is not homogeneous. In section 2.3 the phase diagram (Fig 2.5) shows that the SiO_x growth, as it has been performed here, is at the line between etching and oxidation so that the two mechanisms are competing with each other. Oxide formation takes place preferentially on step edges and forms an oxide cap that shields the underlying silicon from etching [SG82; SEP96]. On the areas between the oxide islands, etching via SiO formation takes place and therefore the oxide islands seem to grow higher. These processes are the reason that the surface is not covered homogeneously with SiO_2. In Figure 5.9 the remnants of this oxygen distribution are visible as oxygen-rich and -depleted regions. The difference in electron scattering of the two elements creates the contrast in the images.

When the silicon top layer is started, the impinging Si atoms have two different environments: the oxygen-rich and the oxygen-depleted or free areas. Incorporation of Si on a pure Si surface is energetically favorable compared with the incorporation of excess Si into SiO_2 , because of the strong bonds in SiO and SiO_2. Breaking a Si dimer needs 0.3-0.8 eV[DM00], but breaking a SiO bond or even a SiO_2 bond takes more than 1 eV. This leads to the assumption that the growth starts on the surface after an oxide spike takes place in the areas with no, or low, oxygen concentration. These areas (Si growth islands) still have the crystal information of the substrate and act as a nucleation center for the growing Si layer. As the growth continues, the surface roughness increases, because the impinging Si is preferably incorporated on Si rich areas. Thus, overgrowth of large oxide islands is slow and creates deep valleys. Given enough time, those valleys are closed and the surface is two dimensional again, as it was before the oxide growth. This model describes very well the RHEED and AFM observations presented in sections 5.1.1 and 5.1.2. The flat surface of the buffer layer changes into an unordered state with oxide islands; that is why the RHEED streaks vanish. Because the overgrowth with Si starts locally on Si rich areas, a three-dimensional rough surface is formed, generating the 3D RHEED pattern. Most likely, when the surroundings of the SiO_2 islands change into a Si rich environment, the Si overgrowth of the SiO_2 slowly begins. Some SiO_2 bonds may be opened due to the changed chemical surroundings, the Si is reduced to Si^{3+}, Si^{2+} or Si^{1+}, and thereby the interface between SiO_2 and Si is softened. Furthermore, diffusion of excess Si through Si/SiO_2 interface, as reported by Uematsu et al. and Tsoukalas et al. [Uem04; TTN01], is capable of reducing the oxygen concentration gradient between the silicon-rich and oxygen-rich areas. This results in a SiO_x layer that consists of domains with higher and lower oxygen concentration, as can be seen in Figure 5.9. The interface between Si and SiO_2 is 5 Å thick [Him88], when both layers are sufficiently thick. In a layered system of Si/SiO_2 /Si, there are two interfaces, each 5 Å, separated by the SiO_2

layer. Hypothetically, if the SiO_2 layer could be removed and the interface regions would remain, the Si layer would be separated by a 1 nm layer, consisting of the interfaces. The SiO_x layer can be considered as such an interface layer, because the ordering of c-Si is preserved but oxygen is incorporated into the layer. In addition, the SiO_x layer thickness of ~1 nm deduced from STEM (Figure 5.9) fits perfectly to double the measured Si/SiO_2 interface thickness of ~ 5 Å. It has been shown that within this interface all oxidation states of silicon exist [Him88; Gru87]. Together with the STEM images, this leads to a model for the oxide layer in which SiO_2 clusters and Si clusters are present with transitions from one to the other.

In Figure 5.10 the growth cycle of one SiO_x layer and the overgrowth is illustrated, beginning with the Si surface that is exposed to oxygen so that oxide clusters emerge. Where the surface is oxide free it is etched by the oxygen. Overgrowth of the oxide layer starts on an inhomogeneous surface and is itself spatially inhomogeneous, called island growth (see Fig. 5.10(c)). With increasing Si layer thickness the islands are joined together and create Si plateaus (see Fig. 5.10(d,e)). The diffusivity of the Si atoms on the surface, which depends on the substrate temperature, plays the key role in this smoothing process. If the diffusion length is large enough for the Si atoms to reach the valleys, the layer growth will tend to smooth out the islands. If the substrate temperature is too low, the Si layer growth continues in a three-dimensional mode. High substrate temperature may cause increased decomposition of SiO_2 and thereby improving the overgrowth process. On a surface that showed a two dimensional reconstruction in RHEED after an oxide spike, AFM measurements have shown that still some holes exist. Most of the surface is flat and the flat areas have the same level, but are separated by small holes (see Fig. 5.10(f)). This means that RHEED observations can be taken as a lead if overgrowth parameters are right to smooth out the surface, but not for a final conclusion on the surface morphology.

To illustrate the temperature dependence of the overgrowth, two samples are compared, one with $T_{sub,Si} = 620°C$, the other with $T_{sub,Si} = 700°C$. The 720°C sample is shown in Figure 5.6 and has a Si layer of 12.6 nm. Compared with Figure 5.5(c)– a sample at 620°C that has a Si layer thickness of 35 nm – it is clearly visible that higher substrate temperatures promote the smoothing out of the valleys and holes in a shorter time.

In addition to the substrate temperature, the Si overgrowth depends on the oxygen dose, i.e. partial pressure and exposure time used for the oxide layer. A higher dose produces a higher oxide island density and larger islands [WWS97] and thus a rougher surface. Seeding centers for the Si layer are further apart, and consequently the time it takes to form a smooth layer increases. Quantitative measurements on this would require studies of the SiO_x layer without breaking the UHV, but all our observations are in agreement with the studies performed by Wei et al. and, Seiple and Pelz [WWS97; SP95].

To investigate SiO_x layers with XRD, the top layer needs to be thick enough so that XRD interference can be used. The fact that interference between top and bottom layer occurs proves that the top layer is single crystal Si (c-Si) with the same orientation as the bottom

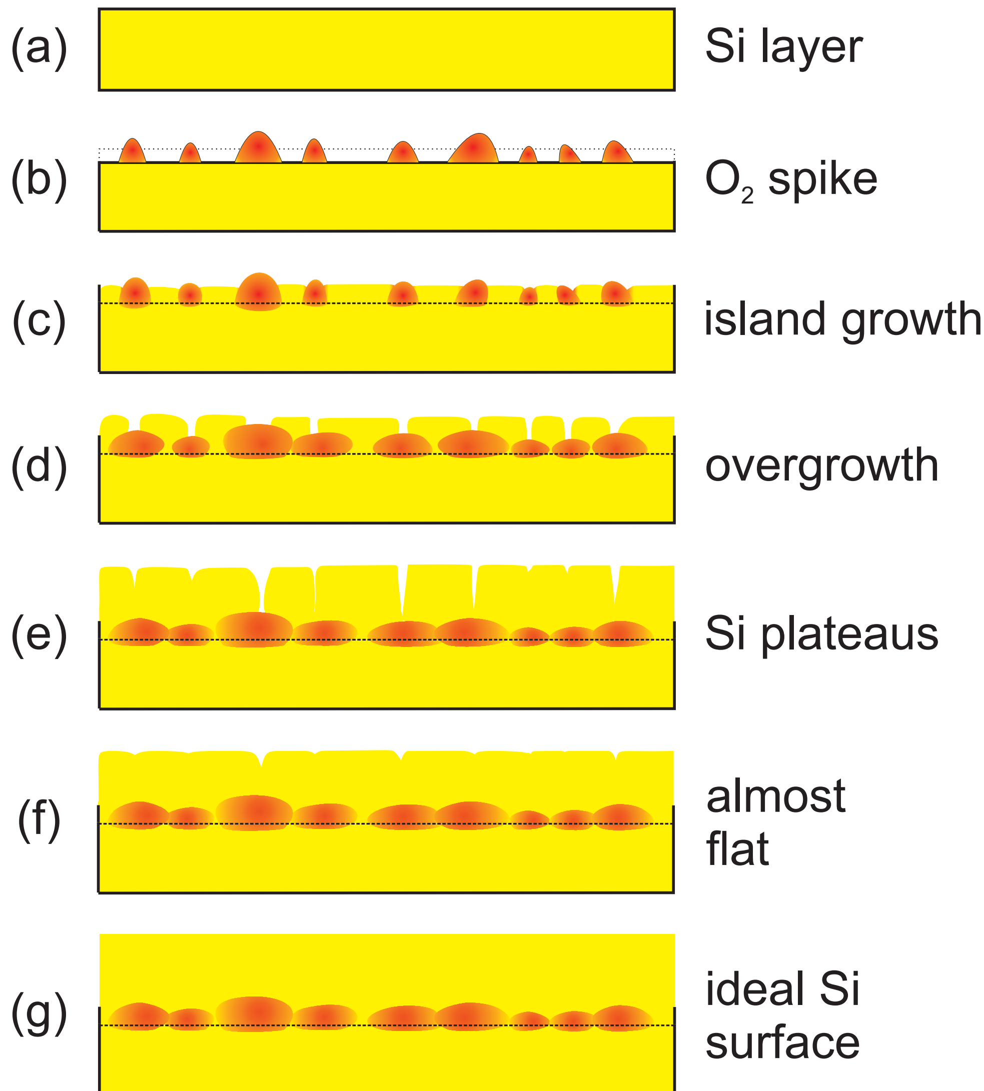

Figure 5.10: Diagram of the overgrowth mechanism, from top to bottom. Silicon is yellow, oxygen is red and SiO_x is depicted as a range of orange. On a flat Si surface (a), the O_2 spike forms oxide clusters and some parts of the Si are etched by the oxygen (b). When Si growth is resumed, Si starts in islands between the oxide clusters; this stage corresponds to a 3D RHEED (c). With increasing Si layer the smaller oxide clusters are overgrown and small Si plateaus develop; in RHEED, streaks start to appear (d). In the further Si overgrowth, plateaus grow larger and only isolated valleys, above large oxide clusters, remain (e). In the final stages the silicon surface recovers more and more (f) until it is an ideal 2D Si surface (g). The time and Si layer thickness needed for the overgrowth depends on the growth parameters.

layer, with only a spatial separation between them. Evaluation of the top layer thickness can be performed by analysis of the interference oscillation period. The thickness of the oxide layer is measured from STEM images, which also show that top and bottom layer are equally oriented c-Si. In the STEM images it looks as though the oxide layer has very much the same crystal structure as silicon, with possibly varying lattice constant caused by the incorporation of oxygen atoms on Si lattice sites or as interstitials. This is supported by the studies of Ourmazd et al. [Our87] and Renaud et al. [Ren91] that suggest a Si/SiO_2 interface with a crystalline oxide layer of about 5Å. The group of Tu et al. have performed Monte Carlo simulations on the structure of the Si/SiO_2 interface which suggest an ordered interface structure without it being an actual SiO_2 cubic crystal [TT00]. Until now, there is no final agreement on the exact structure of the Si/SiO_2 interface, but the measurements presented above do not contradict any of the current theories; moreover they are in agreement with most details of these theories.

5.2 SiO_x Multilayer Structures

As shown in the previous section, the analysis of single SiO_x layer is limited. Multilayer structures offer another approach to determine the structural changes with changing growth parameters. The overall volume of the sample and the amount of oxygen in the sample are increased. Although the measurements average over all SiO_x layers the influence of the interface of the layers on the measurements signal is increased. Multilayer Si/SiO_x structures are periodic repetitions of the single SiO_x layers with cap described in section 5.1. Figure 5.11 shows an example of a multilayer or superlattice structure with five SiO_x layers.

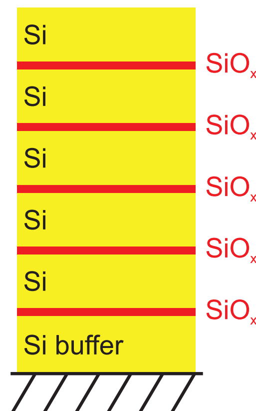

Figure 5.11: Schematic drawing of a five times superlattice Si/SiO_x structure. Silicon spacer layers are yellow and SiO_x layers are red. This sample structure is used for the reference sample Si098.

The oxide spikes are grown at a substrate temperature between 500°C and 620°C, with an oxygen pressure between 1.0×10^{-7} and 8×10^{-7}. As explained in section 5.1, the pressure is read after 30 s of the oxide spike. The oxygen pressure for a multilayer sample is the average of the value for every single oxide spike in that sample. Single spikes deviate up to ten per cent from the average of one sample. The cause of the large deviation is presumably the pressure gauge that is mounted behind the LN_2 shroud and not directly in the molecular beam, and thus is slow to react to the pressure change (see section 3.2.1).

Silicon spacer layers are grown at substrate temperatures between 500°C and 800°C. Temperature ramps between substrate temperature for silicon and for the oxide spike are kept constant. For $T_{Sub,Si} = 700\,°C$ two different ramping speeds are tested for their influence on the sample.

Si/SiO_x multilayer structures are primarily analyzed by XRD. Simulations are used for analysis and interpretation of the measurements. AFM and SIMS are used to complement the XRD data.

5.2.1 XRD Measurements and Simulations

XRD measurements are used to determine layer thickness and superlattice period of the samples. Chemical composition can be determined if the structural information of the layers is known. This is the case for Silicon, but for silicon suboxides it is not even determined whether it has a defined crystal structure. This complicates the evaluation of the measurements to a certain degree. Using simulations to analyze the XRD data opens the possibility of gathering new insights into the composition and structure of the ultra-thin SiO_x layer.

For the simulations the program "X'Pert Epitaxy" from PANalytical (from here on referred to as "Epitaxy") is used. It is a complementary function of the controlling software for the diffractometer and has a built-in database for all widely used elements and compounds. Silicon oxide or silicon suboxide is not common in single crystal diffractometry and hence there is no data in the database of the software nor is reliable data available anywhere for this purpose. Epitaxy can only work with compounds that have the same crystal structure as the substrate; because of that, our simulations are limited to silicon suboxide structures in diamond or zinc blende structure. But as discussed in section 5.1.4, the hypothesis of crystalline SiO_x structures in thin layers is justified.

The program uses the materials in the database to "build" the sample structure from the parameters given by the user. Materials not in the database can be added or existing data can be edited. Important parameters for the simulations are the crystal structure, lattice constants, layer thickness, Poisson number and composition, as well as the x-ray scattering factors and atomic form factor for the elements. The latter have been obtained, if not already in the database, from the *International Tables for Crystallography*,

Volume C [Pri04]. In order to eliminate one of the sample variables, the thickness of a SiO_x layer has been set to 1 nm according to the findings in section 5.1.

Epitaxy lacks features to include growth defects into the simulation such as anti-sites, vacancies or interstitials; only perfect crystals can be simulated. These crystals can include any kind of stress and any alloy composition, which is calculated from Vegard's Law. In order to simulate the ultra-thin SiO_x layers, creative approaches to Epitaxy have to be devised, as the SiO_x layer contains defects at the interface because of the large lattice constant difference. Nicolas Raab (master's student) has done extensive work on simulations with Epitaxy; detailed descriptions can be found in his thesis [Raa12].

With the limited capabilities, the SiO_x layers have been simulated in two categories: first, as homogeneous silicon-oxygen alloy with varying composition (alloy simulation); and second, as silicon layer with oxygen as interstitials with varying oxygen content (interstitial simulation). For the alloy simulation a virtual O crystal with diamond structure is entered in the database. Its lattice constant (a_O) is necessary for the program to be able to calculate the layer lattice constant with Vegard's law. The Poisson ratio for the Si–O alloy is assigned to the same value as Si ($\nu = 0.278$).

Both simulations, alloy and interstitial, were given the same lattice constant as silicon to determine the influence of the oxygen position on the simulation. Differences between these two materials and silicon are due to the different atomic form factor of oxygen and silicon. The XRD scan of the sample Si098 ($5\times(Si/SiO_x)$; see Fig 5.11) has been chosen as a reference due to its clear interference pattern, and the low oxygen partial pressure during the SiO_x growth. In Figure 5.12, the without-stress simulated diffraction patterns and the measured ω-2Θ-scan of the reference sample are compared. The difference between the simulated patterns is rather small and only manifests itself around the superlattice peaks; the interstitial simulation has more distinct maxima and minima. Compared to the reference sample, there are large differences that catch the eye. The simulation is symmetric to the Si(004) peak, especially with respect to the position of the ± 1. order peak and the neighboring intensity minima. The measurement is not symmetric relative to the substrate peak like the simulations, and the oscillations between the zeroth and first order are clearly visible. The substrate peak has a shoulder on the right side and a distinct minimum on the left. The superlattice reflexes result from the phase difference between the spacer layers. Because the simulated materials have the same lattice constant as silicon, the superlattice reflexes result only from the different electron distribution in the SiO_x layer due to the oxygen.

In the next step, influence of stress on the simulation of the SiO_x layers is studied. For this reason the SiO_x layers are represented in the simulation by a material identical with silicon except for the lattice constant. This means that the alloy simulation consists of two types of silicon layers with different lattice constant, and the interstitial simulation of a silicon layer and a silicon layer with silicon as interstitials. Best fit of simulation and reference sample measurement is achieved for a misfit of $f_m = -0.2859\,\%$. Both simulations, alloy

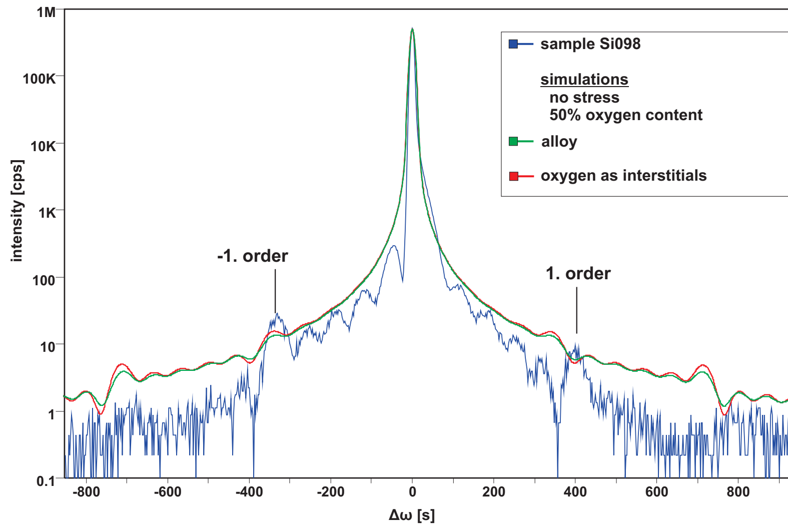

Figure 5.12: ω-2Θ-scan of reference sample Si098 shown with two simulations with no stress. Oxygen content of both simulations is 50% in the SiO_x layers. In red is the simulation of oxygen as interstitials and in green the silicon-oxygen alloy. Features of the simulations are flimsy. The simulations are symmetric relative to the substrate peak in contrast to the measurement.

and interstitial, are performed with these parameters and shown together with the reference sample measurement in Figure 5.13. Either of the simulations reproduces the asymmetry of the reference sample very nicely, although both simulations show larger intensities than the sample. The alloy simulation has higher intensities on the right side of the substrate, whereas the interstitial simulation has higher intensities on the left side. Both simulations have intensities about a factor of two too high compared with the reference sample. The attenuation of intensity is not as strong as in the measurement, at larger $\Delta\omega$ values the discrepancy between simulation and measurement increases. But compared to previous simulations, the position and form of maxima and minima fit the reference sample quite well.

In these simulations the misfit between silicon (substrate and spacer layers) and silicon suboxide layer is changed, and thus the distance between lattice planes changes, highly affecting the interference pattern. Because of the tensile strain and the Poisson ratio the vertical lattice constant is compressed and therefore the diffraction pattern is moved to larger angles (to the right) in relation to the substrate peak. Both versions of the simulations fit the measurements data very well; positions of the maxima are almost identical between the simulations and in very good agreement with the measurement. The difference of intensities of the simulations can be traced back to the interstitial atoms of the respective simulation; they create additional constructive and destructive contributions.

Combining the rather theoretical simulation models into one that combines the chemical

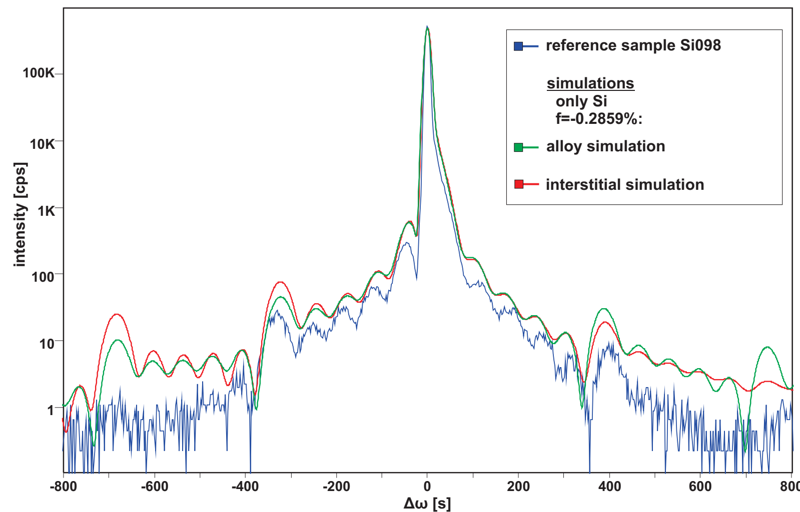

Figure 5.13: Reference sample measurement with simulations based only on strain. The alloy simulation incorporates a silicon layer with different lattice constant; the interstitial simulation incorporates a layer with Si atoms on interstitial sites. Although the intensities of the simulations are higher than the reference sample, position and form of the pattern fit the measurements well.

contrast and the stress is the final step. Both simulation methods now incorporate strain and chemical contrast from different atomic species. The interstitial model has oxygen atoms on interstitial sites in the SiO_x layer whereas in the alloy model oxygen is placed on random lattice sites. Figure 5.14 shows the simulations including stress and chemical contrast, together with the reference sample.

Both simulations are in good agreement with the reference sample; the positions of the maxima and minima and the shape of the peaks are almost identical to the measurement. The difference between the two models has shrunk to almost none. This can be attributed to the chemical contrast, because the interstitial model now only incorporates oxygen on interstitial sites and adds constructive and destructive contributions. But oxygen has less electrons than silicon and is a far less effective scatterer for x-rays than silicon and thus the effect of the interstitials is reduced a great amount. Stress in the SiO_x layer has the greatest influence on the diffraction pattern, because changing the distance of lattice planes of the 1 nm layer has a greater effect than changing the refraction index of the layer.

The XRD analysis of the Si/SiO_x multilayer structures offers the multilayer period, i.e. the thickness of Si spacer layer plus SiO_x layer, and the average vertical strain of the two layers. From TEM measurements the SiO_x layer thickness is roughly determined to 1 nm and therefore its the vertical strain can be calculated. In order to relate the vertical

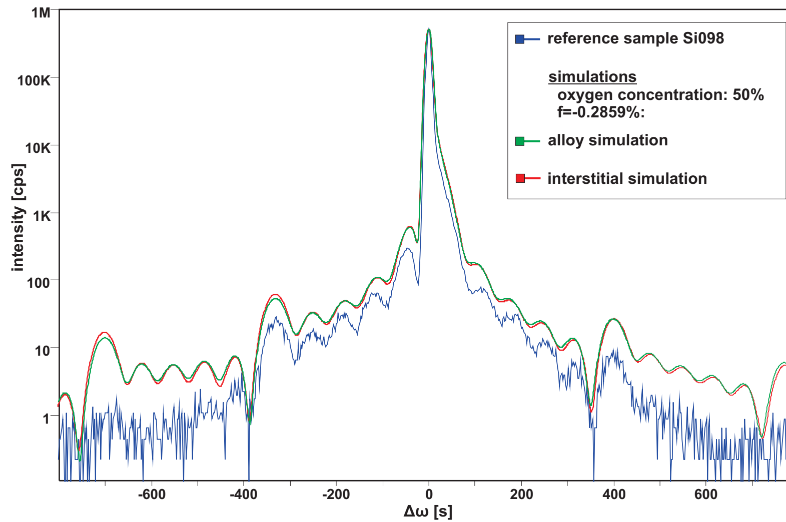

Figure 5.14: Simulations with chemical contrast and stress together with the ω-2Θ-scan of the reference sample. Oxygen concentration is set to 50% and the lattice mismatch is set to $f_m = 0.2859\%$. Both simulations are in good agreement with the measurement. Differences between the simulations are marginal.

strain in the SiO_x layer to the oxygen content of the SiO_x layer a calibration of the oxygen concentration is necessary. Nevertheless, the simulation models are sufficient to analyze the period of the double layers (Si spacer layer plus SiO_x layer).

The general discrepancy in intensities between the simulation models and the measurement can be caused by diffuse X-ray scattering that the models do not account for. Furthermore the incoherence of the superlattice period and the roughness of the SiO_x layer are possible sources that reduce the XRD intensity.

For the analysis of XRD measurements, the alloy model is used throughout the rest of this work because the differences are marginal and the alloy model is the simpler model. This decision is based on computational reasons only, because the physically relevant results are almost identical. The model does not make any statement about the actual incorporation mechanism of oxygen in SiO_x layers.

DISCUS Simulations

In order to circumvent some limitations of "Epitaxy" another simulation software is used. Prof. Neder (Universität Erlangen) and Prof. Profen (Los Alamos National Laboratory)

have developed the open source software DISCUS[5] (Diffuse Scattering and Structure Simulation), a very powerful tool for simulating crystal structures. This software is designed for any kind of crystal. The basic principle is to build the complete system from scratch, beginning with the symmetry of the object, which is then extended to a grid; only after that are atoms inserted. Once the crystal structure is created, changes can be applied—such as voids, interstitials, dislocations or any other kind of defect. Defects can be made at particular positions or randomly distributed over the crystal. The disadvantage of all the possibilities of DISCUS is the extremely time-consuming programming. All changes have to be implemented in the program code, for every grid point, with loops and queries. Creating complex structures such as superlattices needs further programming, even more so if the grid needs to be distorted to simulate strain in the structure. Detailed description of the program and its countless possibilities can be found in the manual [NP10] and the DISCUS cookbook [NP08]. After a simulation is run, the resulting ω-2Θ-scan data is corrected with the Lorentz factor and the atomic scattering polarization term (in short: Lp correction). The Lorentz factor corrects higher intensities at very low and high values of 2Θ, caused by trigonometrical factors of the ω-2Θ-scan. Combined with the polarization term, the complete Lp correction is of the form:

$$Lp\ corr.\ Intensity = Intensity \cdot \frac{1+\cos^2(2\Theta)}{2\cdot\sin(2\Theta)} \tag{5.1}$$

The first approach to the simulation is (analogous to Epitaxy) a silicon and oxygen alloy layer (100 unit cells thick). Therefore, oxygen atoms are inserted in the crystal with a certain probability, but the spatial distribution is random. The probability represents the oxygen content in the crystal. In Figure 5.15, simulated ω-2Θ-scans with varying oxygen concentrations are plotted. In addition, a ω-2Θ-scan of a pure silicon layer is plotted as a reference. It is obvious that the intensity of the ω-2Θ-scan peaks decreases with increasing oxygen content. For a hypothetical oxygen content of 100%, the intensity drops to 19.3%. The inset of Figure 5.15 shows the maximum intensity, normalized to pure silicon, as a function of the oxygen content. This result is not surprising, because the scattering factor for oxygen (5.3) is much smaller than that for silicon (9.4)[CS01].

Next, an interstitial model for SiO_x is created and simulated with DISCUS. An oxygen atom is placed in the silicon unit cell, at position $(\frac{1}{2},\frac{1}{2},z)$. One oxygen atom within the Si unit cell corresponds to an oxygen content of 11.1%, independent of position of course. Figure 5.16 depicts the Si unit cell with all Si atoms and the newly inserted oxygen. In order to study the influence of the interstitial position, the position is varied. As in Figure 5.16, depicted by arrows, the oxygen is moved along the c-axis, whereas positions on a- and b-axis remain constant. Simulation starts with $z = 0$ and ends at $z = 1$, z is given in orders of a_{Si}. On the positions $(\frac{1}{2},\frac{1}{2},0)$ and $(\frac{1}{2},\frac{1}{2},1)$ there are Si atoms in a silicon

5 Used in this work: DISCUS Version 3.6.2, available at sourceforge.net

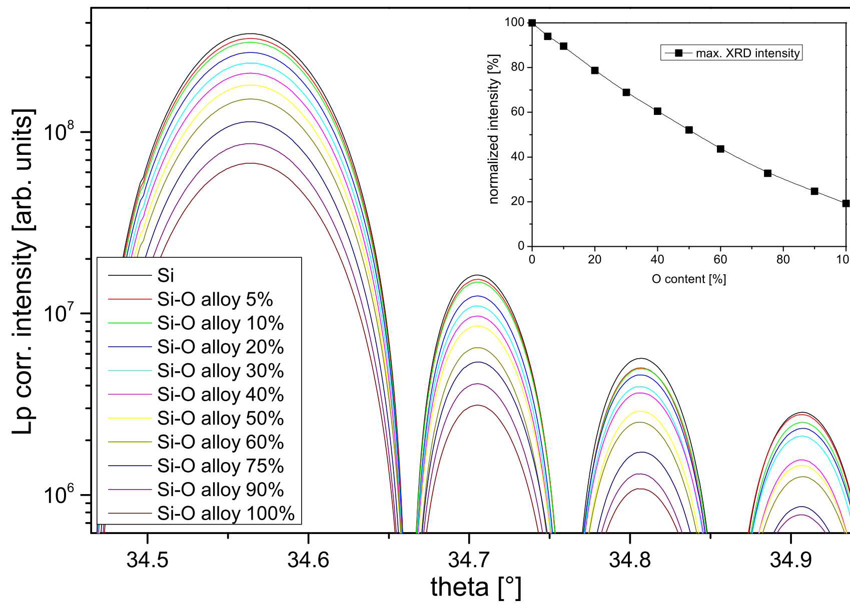

Figure 5.15: Simulated XRD intensity of Si-O alloy layers with different oxygen content. Maximum intensity falls with increasing oxygen content in the alloy. Simulation of pure Si is added as reference. Inset: Maximum peak intensity (normalized to pure Si) as a function of oxygen content.

crystal. When the oxygen atom is inserted at that lattice point, two atoms occupy the point simultaneously. For the simulation program this is no obstacle for the calculations; the scattering coefficient of that lattice point is simply that of Si plus that of O. The positions $z = 0$ and $z = 1$ are only theoretical and do not represent possible interstitial sites for oxygen.

In Figure 5.17a, the maximum 004 peak intensity is plotted against the z-position of the oxygen atom. The intensity is normalized to an ω-2Θ-scan of a pure silicon layer. Caused by the variation of the z-position, the intensity varies between maximal 111.3% and minimal 89.4%. The z-positions for which the maxima occur are $z = 0, \frac{1}{4}, \frac{1}{2}$ and $\frac{3}{4}$. The minima occur when the oxygen positions are $\frac{1}{8}, \frac{3}{8}, \frac{5}{8}$ and $\frac{7}{8}$. Intensity variations caused by the interstitial oxygen amount to a total variation of 21.9%. The maxima occur when the oxygen is placed in a lattice plane that contributes constructively to interference. In contrast, the minima occur when the oxygen is exactly in between those lattice planes. One interstitial atom per unit cell corresponds to 11.1% oxygen concentration. This lies close to the lower limit of oxygen concentration in the samples determined by XRD and SIMS; the maximum was three times that concentration. Furthermore, the oxygen atoms in the simulations contribute 100% to coherent scattering, whereas it is likely that in the SiO_x layer some of the oxygen causes non-coherent scattering. Therefore, the intensities

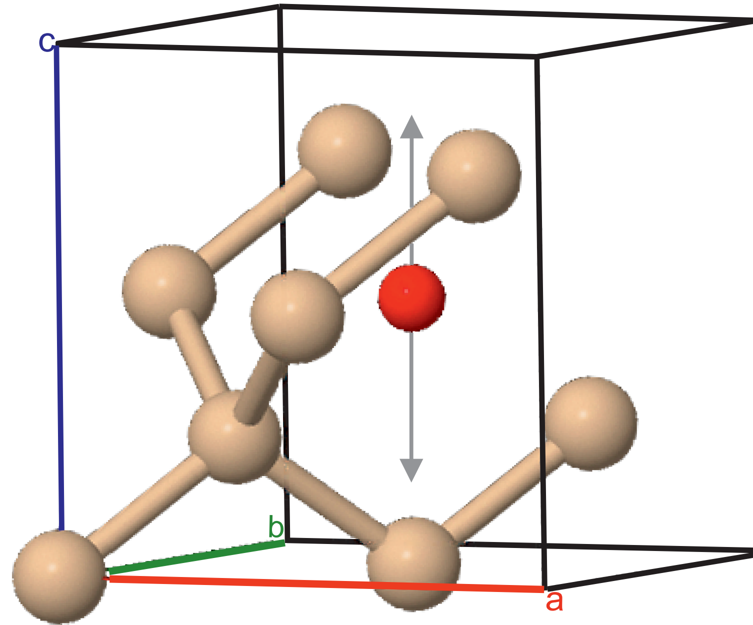

Figure 5.16: Silicon unit cell with interstitial oxygen atom at $(\frac{1}{2},\frac{1}{2},\frac{1}{2})$. Silicon atoms beige and oxygen red. In the simulations the z-position of the oxygen atom is changed, as indicated by the arrows.

of the simulations are not a good measurement for the oxygen concentration. The lattice mismatch caused by the oxygen, on the other hand, is because the incorporated oxygen causes distortion of the Si lattice planes regardless of its scattering type.

The complicated methods needed to simulate interstitials with Epitaxy made it necessary to check the reliability of those simulations. In Figure 5.17b the two simulation programs are compared. Simulated in the Figure is a sole SiO_x layer with a thickness of 100 unit cells, corresponding to 54.31 nm, with O at position $z = 0.5$. Both simulations generate diffraction patterns with the same peak width and fringe period. DISCUS simulates the main peak at exact 34.56347°, which corresponds to a lattice constant of a_{Si} =5.43102Å. This is expected as the simulation is fed with a_{Si} as starting parameter. The deviation of the Epitaxy simulation is small, but it shows the disadvantage of the program, because the peak position is at 34.56920° and therefore the corresponding lattice constant is 0.15‰ smaller than the input of the simulation. However, this extremely small difference is much smaller than the error of XRD measurements. In addition, the change of intensity with varying oxygen content is analyzed. Figure 5.18 shows Epitaxy simulations based on the

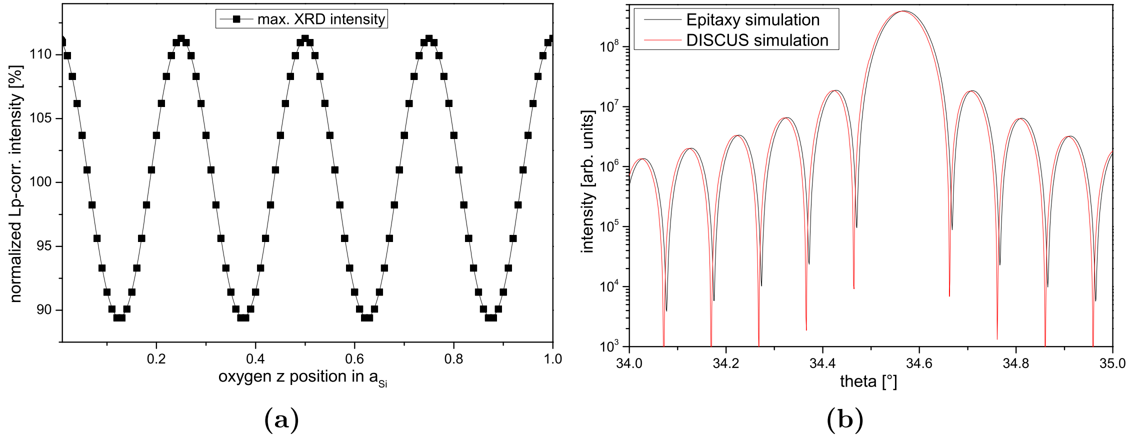

(a) **(b)**

Figure 5.17: (a) Maximum XRD 004 peak intensity as a function of the z position of the O atom within the silicon unit cell. XRD intensity is normalized and position is given in orders of a_{Si}. (b) Comparison between interstitial simulations performed with Epitaxy (black) and DISCUS (red). Peak width and fringe period are identical. A slight difference in the position of the maximum is observed, caused by the work-around needed for the interstitial simulation in Epitaxy.

interstitial model with varying oxygen content. This analysis is analog to Figure 5.15, where DISCUS alloy simulations are shown. The maximum peak intensity of the Epitaxy simulation decreases with increasing oxygen content. The Inset of Figure 5.18 shows the decrease of the maximum peak intensity normalized to a layer without oxygen. For oxygen contents up to 30 % the interstitial Epitaxy simulations are consistent with the DISCUS alloy simulations. The difference between the two simulation programs could be caused by different methods of calculating the atomic scattering factors or different weighing of multiple scattering probabilities. Furthermore, comparing the interstitial models of Epitaxy and DISCUS shows identical decrease of intensity for 10 % oxygen content.

In conclusion, the comparison of both simulation programs shows that the results are consistent independent of the model or program used for simulation. Variations between the simulations are small. At high oxygen contents the results of Discus and Epitaxy show an increasing difference; the difference starts becoming relevant at oxygen contents larger 30 %. However, the samples analyzed in this work do not exceed 27 % oxygen content, therefore the sample analysis with Epitaxy simulations is justified.

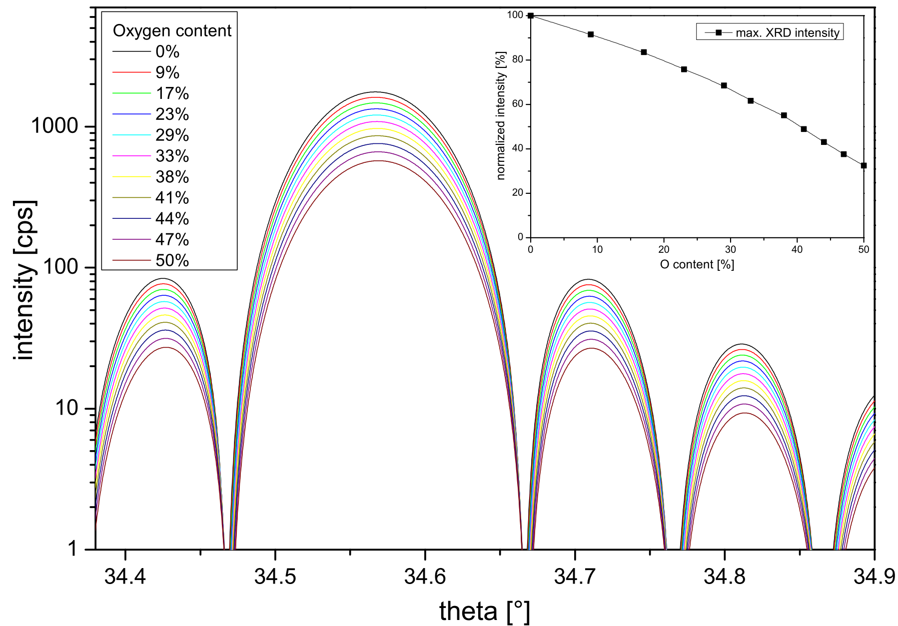

Figure 5.18: Epitaxy simulations with the interstitial model for different oxygen content. The inset shows the decrease of the maximum peak intensity with oxygen content.

Oxygen Content Calibration with SIMS

In order to evaluate the absolute oxygen content of SiO_x layers and to calibrate the simulations, SIMS measurements are performed. The measurements are carried out by courtesy of Forschungszentrum Jülich. Calibrating the reference sample and the simulations is a key task for future analysis of SiO_x multi layers.

Figure 5.19 shows the SIMS measurement of reference sample Si098; the five SiO_x layers are easy to identify. Maximum counts of the peaks decrease with sputter depth; standard deviation from the average peak height is 9.6%. A closer look at the peaks shows that their form is almost identical, but the shape is not symmetrical (see Figure 5.20). There are two possible explanations for the asymmetry of the peaks: first, the growth mechanism of the SiO_x supports diffusion of oxygen into the silicon layer; second, sputtering atoms can drag/drive the surface atoms into the crystal, so that the oxygen is there only due to the measurement. The latter is typical for SIMS measurements and the more likely cause for the peak asymmetry. Nevertheless, the depth resolution is high, the FWHM of the peak is 2.1 nm, but the resolution is not high enough to be able to measure the SiO_x layer thickness.

In order to account for all oxygen atoms in the analysis and to allow disregard for the asymmetry of the peaks, the peaks are integrated. This is justified because the distribution

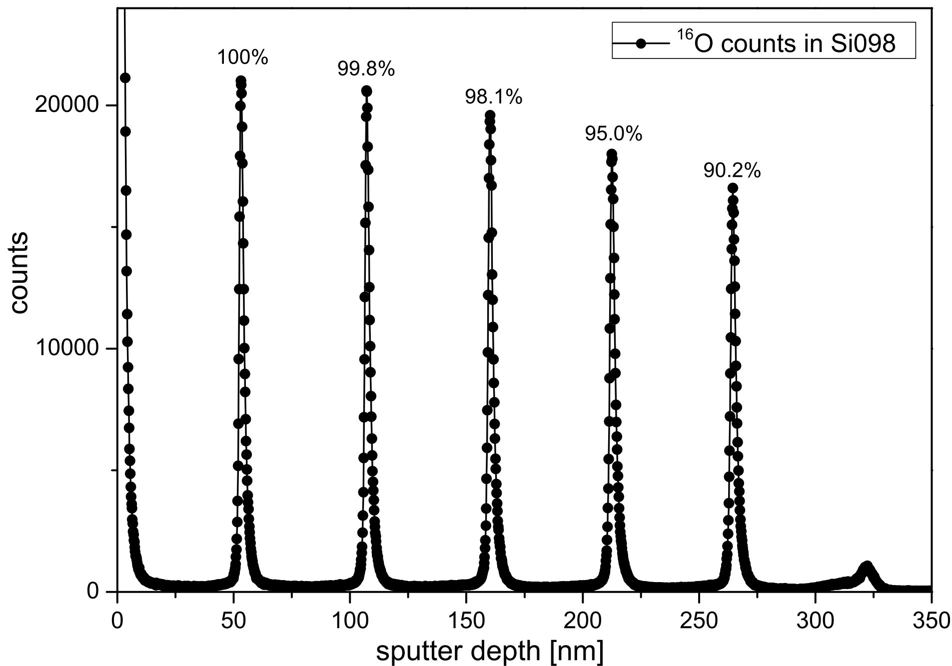

Figure 5.19: SIMS measurement of reference sample Si098. The signal represents the counts of ^{16}O atoms in the sample. Five SiO_x layers are highly visible; the small rise in counts at 322 nm is caused by the layer-substrate interface. Average maximum counts per peak is 19170 counts $\pm$ 9.6 %. The numbers above the peaks are the integrated peak counts for each peak based on the peak at 53 nm.

of oxygen is not as important for the calibration as the amount measured, and with the FWHM of the peaks the asymmetric tail would be ignored. To account for the changing heights of the peaks the average of the integrated peak counts (called intensity) is calculated. For the reference sample Si098, the average intensity is 298960 counts $\cdot$ s with a standard deviation of 4.3%.

Without a calibration standard, the intensities cannot be related to absolute values. For the standard, an industrial grade silicon wafer with a defined thermal oxide layer of 10 nm capped with 50 nm of amorphous silicon is used. During the measurement of the standard, the SIMS detector saturated because of the high oxygen concentration, so instead of ^{16}O the scarcer oxygen isotope ^{18}O is detected. With a natural ratio of 500 : 1 for ^{16}O : ^{18}O the concentration of ^{16}O can be calculated. Inaccuracies of this calibration method are matrix effects as described in section 3.7, caused by the different chemical surroundings of the atoms in the calibration standard compared with the sample. Although this standard is not the optimum the measured ^{18}O intensity of 50559 counts $\cdot$ s corresponds to 25279500 counts $\cdot$ s of ^{16}O. Using the density of silicon dioxide ($2.19 \frac{g}{cm^3}$ [WHW07]) and the thickness of 10 nm the areal density of oxygen can be calculated to $4.39 \times 10^{16} \frac{1}{cm^2}$.

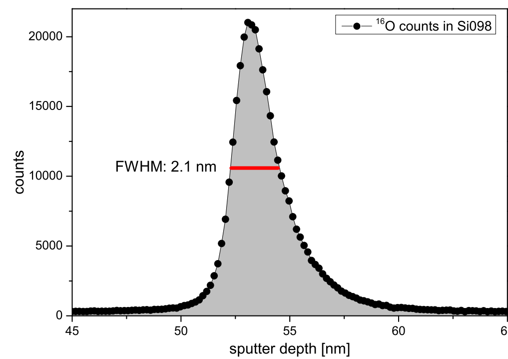

Figure 5.20: SIMS of single SiO_x peak (Si098). Peak asymmetry typical for SIMS is visible. FWHM is 2.1 nm.

In relation to the diamond lattice areal density this equals 64.75 mono layers (ML) of oxygen. The uncertainty of this value is derived from the inaccuracy of SiO_2 thickness and possible variation of the oxygen isotope ratio. With the calibration the oxygen content of the reference sample Si098 can be calculated. Integrated intensity of the sample is a factor of 0.0118 smaller than the SiO_2 standard therefore the SiO_x layer of Si098 has 0.765 mono layers of oxygen. Combining thickness (1 nm) and the oxygen coverage gives an absolute oxygen concentration of 10.4% for the SiO_x layer.

Determining the uncertainties of this analysis, it is obvious that the standard used to calibrate the SIMS is crucial. The ion yield depends on the chemical surroundings and they are quite different in the two samples. In silicon dioxide the binding partners for any Si atom are two O atoms, in SiO_x layer with $x < 0.3$ it is primarily 4 Si (compare Figure 2.4). Furthermore, SiO_x layers are mostly crystalline but SiO_2 is amorphous. Unfortunately, there was no possibility of preparing a sample with known oxygen content that is in the same order of magnitude as in the SiO_x layer. Ion implantation technique could be used to dope a Si wafer with oxygen with high precision. Although, ion implantation would not incorporate the oxygen the way it is in SiO_x , the chemical surrounding of the oxygen would be closer to SiO_x than it is in silicon dioxide. Such a standard would increase the accuracy of the analysis.

Discussion

Now that the oxygen concentration is determined, the simulations (see beginning of section 5.2.1) can be refined. The oxygen content is determined by the SIMS measurements presented in the previous section. All parameters of the simulation are now determined, except for the lattice constant a_O. By adjusting the lattice constant a_O of a virtual diamond O crystal the simulation is fitted to the measurement of the reference sample Si098. The best fit is achieved for $a_O = 5.2429$ Å, with oxygen content 10.4 % and Poisson

ratio $\nu = 0.278$ (the Poisson ratio of Si is used for the virtual material). For the $SiO_{0.21}$ layer of Sample Si098 the misfit is simulated to be -0.3603 %. The best fit simulation for the sample Si098 is shown in Figure 5.21.

The simulation fits very neatly to the XRD data, superlattice peaks are at the right positions, the fringe period is matched. On the right side of the substrate peak is a shoulder that is the 0th order of the superlattice reflexes. Being on the right side (side of larger diffraction angles) means that the layer is tensile strained. Subtle details of the XRD ω-2Θ-scan—such as the destructive minima being always on the left side of the superlattice peaks ($\Delta\omega \approx -390$" and $+360$") and the slightly asymmetric shape of the fringes—are displayed correctly by the simulation. Nonetheless, the simulation has an overall higher intensity than the XRD data. This could be caused by partial incoherent scattering of the sample or the interface imperfections, because Epitaxy does not account for these. Real interfaces have roughness and are not perfectly homogeneous but the simulation assumes they are ideal interfaces. Furthermore, slight variations of growth rate cause Si spacer layers with different thicknesses, and these broaden and decrease the diffraction peaks. From the SIMS measurement, the order of magnitude of the variation can be estimated by measuring the distance between the SiO_x layers. Spacer layer thickness of the reference sample has a standard deviation of 1.8 %. Also, the SiO_x layer has thickness variations. Their role for the diffraction pattern is not as influential, but is very important for the oxygen concentration of the sample. If the layer is 2 nm instead of 1 nm the calculated oxygen concentration is reduced by half. For this reason the integrated oxygen content is given in mono layers instead of percentage, so the layer thickness can be ignored. Within

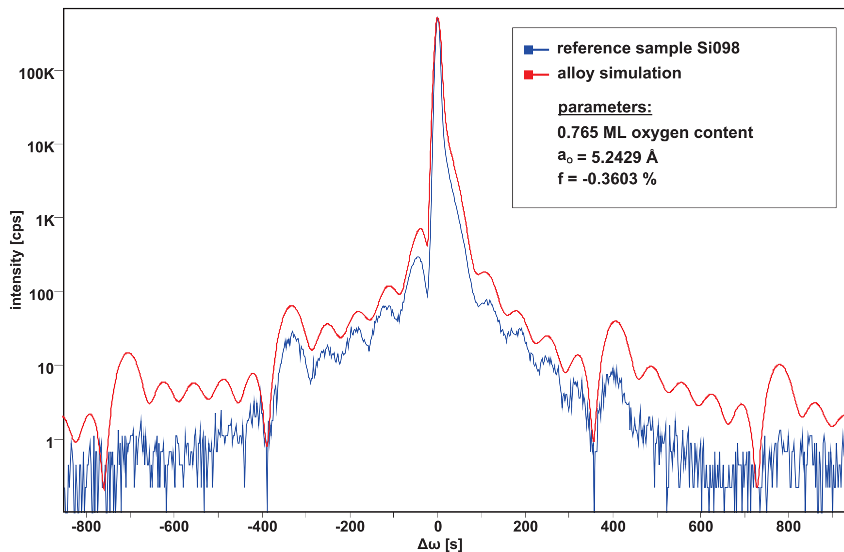

Figure 5.21: Optimized simulation with XRD data of sample Si098. O_2 content is calibrated with SIMS and fitting the simulation resulted in $f_m = 0.3603$ %.

one sample, the different SiO_x layers are assumed to have the same oxygen content, but from the readings of the pressure gauge during SiO_x growth it is suspected that the oxygen level rises slightly ($\sim 6\%$) with time. SIMS measurements confirmed this: the peak height deviates up to 10 % but the more significant integrated peak intensity deviates only up to 5 %. Simulations of layers that are based on separately analyzed peaks show no differences compared to the ones using the average oxygen content for all layers.

With DISCUS, as a second program for crystal simulations, the use of Epitaxy as a simulation tool for Si/SiO_x structures has been justified. Epitaxy produces an error of 0.15‰ in the calculations, though this error is negligible for the evaluations used here. The advantages of Epitaxy as a fast tool to fit measurement data far surpasses the minor disadvantages in precision.

On the basis of the simulations with DISCUS, the influence of oxygen, as alloy or interstitial, on the diffraction intensities has been investigated. For a single Si–O alloy layer the diffracted intensities decrease with the oxygen content, whereas the intensities of the interstitial model increase or decrease depending on the position. The variations of the intensity are not large enough to be able to explain the difference between measurement and simulation. Non-coherent scattering due to the inhomogeneous SiO_x layer and variations of the SiO_x and spacer layer thickness are the likely cause for that difference. In the simulations, non-coherent scattering is not accounted for and the layers have identical thickness', therefore the simulated intensities are considerably larger than the ones measured.

Overall the simulations have been improved to a state at which they can be used to analyze the oxygen content. However, the analysis is limited to samples that show a clear interference pattern to which the simulation can be fitted. This limits the usability of the simulations for samples with a very high oxygen content as they tend to exhibit almost no fringes. On the question of how the oxygen is incorporated in the Si matrix in SiO_x layer, the simulations give no information. Further, the presence of SiO_x clusters might lead to incoherent scattering. This is not included in the simulation and therefore the simulated intensity is higher compared to the measurements. If SiO_x clusters are present, the actual oxygen content would be higher than determined by XRD and the simulations. In addition, the SiO_x clusters contribute to the SIMS signal but not to the XRD. Hence, they could explain the difference between XRD and SIMS. Nonetheless, oxygen content determined with simulations can be used for evaluation of similar multilayer structures, because all simulations are based on the same presuppositions.

5.2.2 Optimization of Growth Parameters

With the help of the developed simulation model for SiO_x layers, the parameter space of growth parameters is explored. The focus of the study is the influence of growth parameters

on the oxygen content of SiO_x layers. Therefore, substrate temperature, oxygen pressure and duration for SiO_x growth are systematically varied. Duration of the oxygen inlet is 40 s or 45 s; only in one case is the time drastically reduced to 20 s. Pump down time, after oxygen inlet, is 10 s, except for one series where it is extended to 90 s.

Oxygen Dose

First the influence of the amount of oxygen put into the layer is studied. The crucial parameter is the amount of oxygen available at the surface, and that depends on oxygen pressure and duration of exposure. In order to simplify the comparison, the two parameters are combined; hence the oxygen dose is defined as pressure times duration.

$$Dose\,[mbar \cdot s] = p_{O_2}\,[mbar] \cdot time\,[s] \tag{5.2}$$

It should be noted that the O_2 flux can be estimated from the O_2 pressure (see page 22 in section 3.2.1). Dividing the flux density integrated over exposure time, by the amount of Si surface atoms ($6.78\times10^{14}\,cm^{-2}$) results in a mono layer coverage. This coverage is ~ 5.5 times larger than the oxygen content (in ML) determined with SIMS and XRD measurements. When the low sticking coefficient (≈ 0.01 [DNE87]) of the O_2 on the Si(100) surface is considered (see section 2.3) the calculated O_2 coverage is smaller than the measured oxygen content by a factor of 12. The unfavorable position of the pressure gauge (see section 3.2.1) is likely to cause the major contribution to this deviation. The measured O_2 pressure is possibly much smaller than the O_2 pressure at the sample surface. Furthermore, the sticking coefficient depends on the kinetic energy of the O_2 , T_{sub} and the angle of incidence [DNE87]. In order to determine the actual O_2 flux, the deviation of the measured to the actual pressure would need to be determined. For these reasons, the oxygen dose is used rather than the calculated oxygen coverage.

Five sample series are presented in this section. Within a series, one parameter is varied while all others are fixed. No errors are given to the dose because quantitative error analysis is not possible due to the sources of the errors. First and most significant is the position of the pressure gauge (see section 3.2.1). Second, the accuracy of the gauge itself is limited to one decimal digit. There is of course an error of the time measurement, but it is orders of magnitude smaller. These factors together lead to an estimated error for the relative dose (between samples) of at least 20 %. The error of the absolute dose is dominated by the position of the flux gauge, as described above, and is in the order of a factor of 12.

In Figure 5.22 the oxygen content determined by SIMS and simulation are plotted against the oxygen dose. One sample is marked because the oxygen exposure is only 20 s compared to 30 s for all other samples. In addition, sample Si098 is marked as it is the sample used to calibrate the simulations (see section 5.2.1) and thus both data points for this sample

must be identical. The origin is used as a data point for best-fit lines since zero oxygen dose must result in zero oxygen content. When comparing the simulation data with the SIMS data, it is apparent that the analysis by means of simulation results in higher oxygen content; the difference of both contents increases with higher oxygen dose. Several causes can be identified to explain this characteristic. First, the simulations are fitted to the XRD measurements; if the XRD data has much noise or the features of the diffraction pattern are hard to identify, an error occurs when fitting. Second, with more oxygen in the layers the chemical surrounding changes and thus the ion yield for SIMS changes.

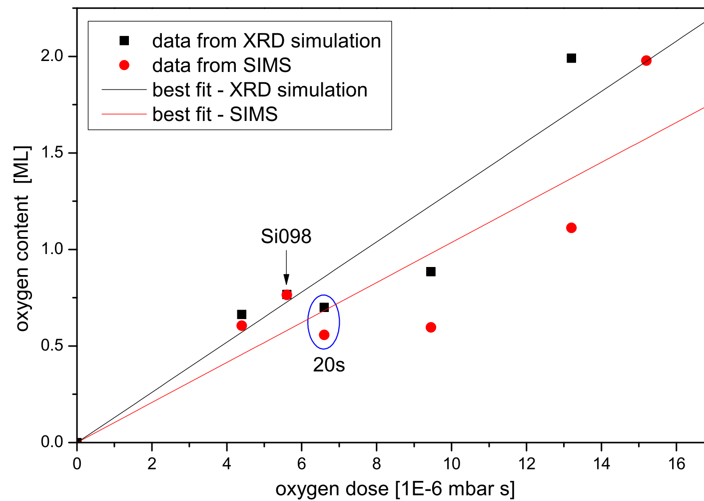

Figure 5.22: Oxygen content determined by SIMS (red) and XRD simulation (black) against oxygen dose. Best-fit lines of the data are in corresponding color. Only samples for which SIMS data was available are displayed. Oxygen content determination by simulation results in higher oxygen levels compared with SIMS. The sample (Si098) used as reference for the simulations is marked as well as the sample with only 20 s oxygen exposure.

Now the sample series are compared with respect to their oxygen content, depending on dose and growth parameter. In Figure 5.23 three sample series are plotted. The ordinate in this Figure is the oxygen content in mono layers (ML) determined from XRD measurements and it is plotted against oxygen dose. Sample series are color coded and crucial parameters are written in the graph. Best-fit line for all series through the origin is also plotted. In Figure 5.24 two more sample series are plotted in the same plot style. Here for each series a best fit line is plotted. All series show a linear correlation between oxygen dose and oxygen content. In Figure 5.23 the slope is $1.69\times10^{6}\frac{\mathrm{ML}}{\mathrm{mbar\ s}}$ and the slope of series D in Figure 5.24 is $1.43\times10^{6}\frac{\mathrm{ML}}{\mathrm{mbar\ s}}$. Considering the oxygen dose error, the slopes of the best fit lines are almost identical. The large variation of data points from the best-fit line is also attributed mainly to the oxygen dose error. When comparing series D and E, it is noticeable that series E has similar oxygen content although the dose is twice as high. This must be caused by the different growth parameter. Growth temperature and spacer

layer thickness differ in these two series, but the latter has supposedly low influence on the oxygen dose. Therefore, the growth temperature must be the reason (this behavior is discussed later in this section).

Discussion

For all sample series there is a linear correlation between oxygen dose and oxygen content: for series A to D, the slope of best-fit line is identical considering dose error. This correlation is confirmed by SIMS analysis, although the listed uncertainties result in a generally lower oxygen content. The measured oxygen content of all samples ranges from 0.60 ML to 1.98 ML. Assuming that the SiO_x layer is always 1 nm the absolute oxygen concentration ranges from 7.6 % to 26.8 %, but (as already discussed) the absolute O concentration depends on actual SiO_x layer thickness. Without methods to determine the SiO_x layer thickness with certainty, the absolute concentration is not a useful quantity. The above calculated numbers are based on an assumption, motivated by TEM measurements, of 1 nm SiO_x layer thickness. Saturation effects at high oxygen dose, as reported by Seiple et al. [SEP96], are not observed. But the doses used by Seiple et al. are up to 1000 times larger than the ones here.

Substrate Temperature

Substrate temperature is important for any layer growth, not only in MBE. Changing the substrate temperature can change the crystal properties a great deal. For silicon and silicon suboxide, substrate temperature is crucial, but usually both layers require a different temperature range. Combining the growth of the two materials requires changing the substrate temperature for each material; $T_{sub,O}$ is the temperature for oxide growth and $T_{sub,Si}$ for silicon growth. Measuring the substrate temperature has a large error in respect to absolute temperature; reproducibility of the substrate temperature is very good and as a growth parameter this is sufficient. In order to compare data with literature and publications this is a problem, because the estimated offset is as large as±50°C.

Substrate Temperature for Silicon Suboxide

Substrate temperature for SiO_x is, according to the phase diagram (see Figure 2.5 on page 15), a very important parameter. High temperatures and low O_2 pressure results in etching while low temperatures and high O_2 pressure results in oxidation. In between these two there is a transition region in which both mechanisms compete. Only a small sector of and around the transition region is explored with the samples grown. At substrate temperatures larger than 650°C, SiO_x growth was not possible with the oxygen partial pressure used. The sample series presented in Figure 5.23 and 5.24 are grown at different

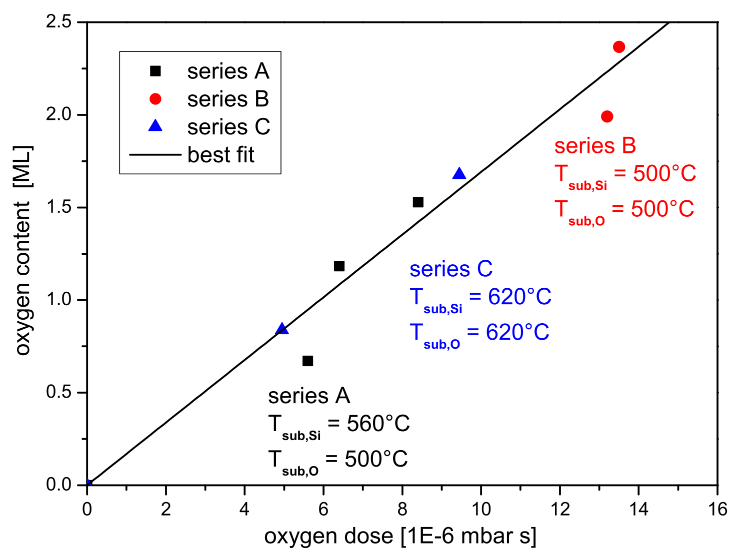

Figure 5.23: Oxygen content determined by XRD simulation versus oxygen dose for three sample series with best-fit line. Linear correlation is apparent. Parameters of the series are noted within the graph.

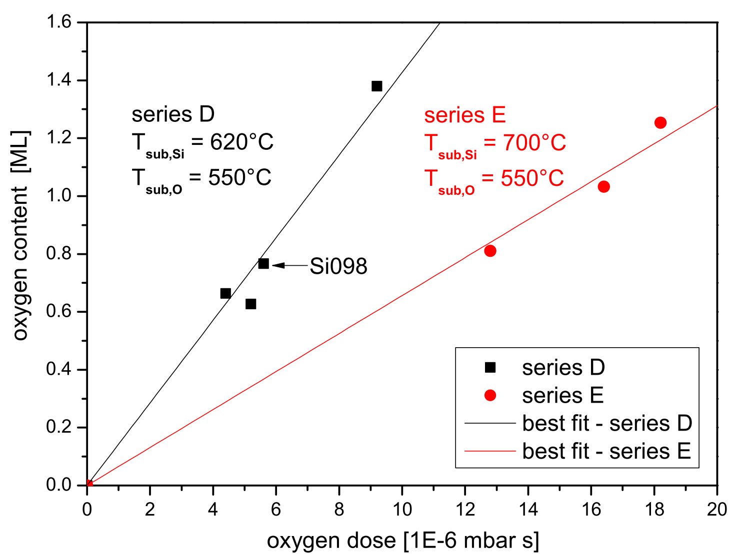

Figure 5.24: Oxygen content determined by XRD simulation versus oxygen dose for two sample series with best-fit line for each series. Linear correlation is apparent.

temperatures $T_{sub,O}$ below 650°C. Precisely, series A and B are grown at 500°C, D and E at 550°C and series C at 620°C. All series, except for series E, have identical slope when considering the uncertainties (see Fig. 5.24 and 5.23). But in series A to D, $T_{sub,O}$ varies from 550°C to 620°C. Although, a higher oxygen concentration is expected for lower $T_{sub,O}$, this is not observed in the narrow range of $T_{sub,O}$ used. At temperatures above 600°C, the influence of SiO desorption increases with temperature according to Engstrom et al. [Eng91], but the influence on the sample series is less than expected. At this point, the problem with the uncertainty of the absolute temperature might be the reason the influence is not observed. Yet, at this point, no correlation of $T_{sub,O}$ and oxygen content can be determined.

Substrate Temperature for Silicon Growth

Substrate temperature for silicon growth is considerably increased in series E compared to all other series. In Figure 5.24 the slope is less steep and the oxygen content is the same, although the dose is more than twice that of series D. The resulting oxygen content could be due to increased SiO desorption at temperatures above 600°C [Sue99; SEP96]. To test this hypothesis samples are grown with $T_{sub,Si}$ = 800°C. All other parameters are identical to series D and E. RHEED observations during growth are analogous to all other samples. During oxygen inlet the streaks disappeared and afterwards growth began—for 40 s T_{sub} is kept at $T_{sub,O}$ then it is raised with a rate <0.5°C/s—and a spotty pattern appeared. However, the time until the spotty pattern returned to a streaky pattern was considerably shorter than for previous samples. When $T_{sub,Si}$ was between 700°C and 800°C RHEED indicated the surface to be smooth again. XRD analysis showed no signs of an interference pattern. Both analyses indicate that the SiO desorption rate increased so fast that no detectable oxygen was left in the SiO_x layers in the multi layer structure.

Furthermore, oxygen incorporation depends on the surface roughness of the layer exposed to oxygen. Rougher wafer surfaces are larger than smooth ones, and rougher surfaces offer more sites with lowered incorporation barrier. Incorporation of oxygen into the surface has been discussed in section 5.1.4. Surface roughness does not depend on $T_{sub,O}$ but on $T_{sub,Si}$ as it determines how effective the roughness is evened out.

In Figure 5.25 AFM scans of multi layer samples with different $T_{sub,Si}$ are shown. For the sample in 5.25(a), substrate temperature was $T_{sub,Si}$ = 620°C, and for the sample in 5.25(b) it was $T_{sub,Si}$ = 700°C. The difference in roughness is clearly visible: RMS for the $T_{sub,Si}$ = 620°C sample is calculated to 2550 pm, whereas the $T_{sub,Si}$ = 700°C sample has a RMS of 269 pm. Although the high temperature sample has a little smaller spacer layer and more multilayers, the surface roughness is considerably better.

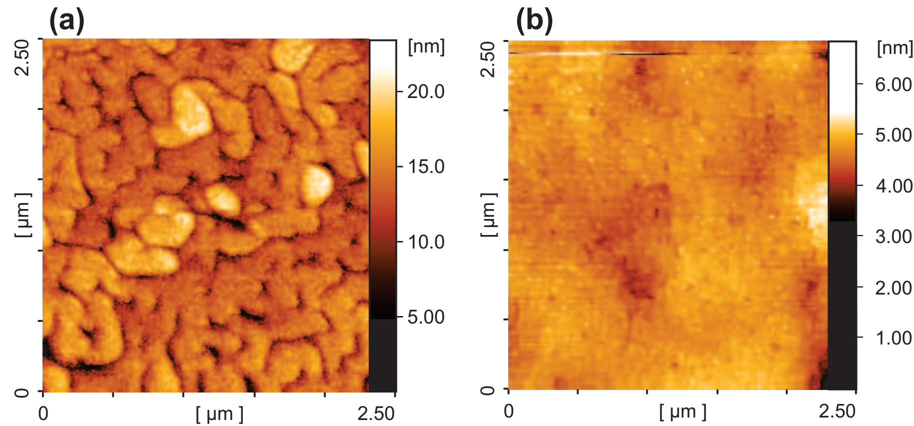

Figure 5.25: AFM scan of SiO_x multilayer samples with different $T_{sub,Si}$. (a) $T_{sub,Si}$ = 620°C the roughness is clearly visible. Top layer thickness is 35 nm and RMS is calculated to 2550 pm. (b) $T_{sub,Si}$ = 700°C: the surface is smooth, hardly any features to identify. Top layer of this sample is 32 nm and RMS is 269 pm.

Discussion

The errors and uncertainties of the characterization methods, as already described, make certain evaluation difficult. $T_{sub,O}$ has little influence on the oxygen content as long as $T_{sub,O} \leq 620°C$. At temperatures above that, SiO_x growth is not possible with the oxygen pressure used here. SiO desorption seems to have less influence below 620°C than would be expected according to A. Sticht [Sti02b].

Influence of $T_{sub,Si}$ on the oxygen content is not observed for $T_{sub,Si} \leq 620°C$, but for $T_{sub,Si} \geq 700°C$ the influence is abundantly clear and may be explained as follows. After oxide growth, the substrate temperature $T_{sub,O}$ is kept for 40 s until the temperature ramp (0.5°C/s) is started. The surface develops the islands discussed in section 5.1 and, while T_{sub} rises above 650°C, not all oxygen clusters are covered by silicon. At high temperatures, the SiO desorption increases and thus the influence of $T_{sub,Si}$ on oxygen content increases too. For $T_{sub,Si}$ = 700°C the influence is considerably larger than for $T_{sub,Si}$ = 620°C. Hence, samples grown with the same oxygen dose, but a high $T_{sub,Si}$, have a lower oxygen content than those grown with a lower $T_{sub,Si}$. For the sample with $T_{sub,Si}$ = 800°C, it is most likely that almost all oxygen is desorbed before the silicon could create a closed surface.

Furthermore, the studies show that $T_{sub,Si}$ is the important parameter for overgrowth of SiO_x layers. At elevated temperatures, surface islands disappeared faster after oxide growth. This is caused by higher mobility of the Si atoms on the surface.

Optimized Growth

In the sections before, growth parameters are investigated for their influence on the sample. Knowing what is caused by trend changing a parameter opens the possibility to improve the overall sample quality while still having the desired properties. Using $T_{sub,Si}$ = 620°C and $T_{sub,O}$ = 550°C, samples with good structural quality and oxygen content between 0.66 ML and 1,38 ML can be produced employing oxygen dose between 4.4×10^{-6} mbar·s and 9.2×10^{-6} mbar·s . Spacer layers in these samples are 50 nm thick and ten multilayer repetitions can be grown without any sign of declining structural quality. Samples with oxygen content up to 2.37 ML can be grown, but need substrate temperature for oxygen and silicon of 500°C. Their structural quality is strongly influenced for the worse by the low substrate temperature for silicon, as discussed in the previous section.

For $T_{sub,Si}$ = 700°C, the Si atom mobility is increased compared to $T_{sub,Si}$ = 620°C, and thus the island growth is evened out faster. Therefore spacer layer thickness can be reduced because the surface is smooth again. At higher temperatures desorption of SiO becomes more relevant, causing lower oxygen coverage. Even at high doses such as 1.82×10^{-5} mbar·s , oxygen coverage is only 1.25 ML (Figure 5.24).

The growth process is optimized in order to incorporate more oxygen at high temperatures, to smooth out the surface as fast as possible. For this a 550°C Si step is introduced right after the SiO_x layer. In this 300 s step, Si is grown over the SiO_x layer in order to prevent SiO desorption when the substrate temperature is raised for the spacer layer. Only after this step is $T_{sub,Si}$ raised to 700°C at a rate of 0.5°C/s. Spacer layers in this sample are 48 nm.

In Figure 5.26, XRD ω-2Θ-scans of two samples are shown. One sample (blue) is grown with the 550°C step just described; the other sample (red) is grown without that step, but with otherwise identical parameters. The sample grown without the 550°C step is colored red, oxygen dose is 1.84×10^{-5} mbar·s and oxygen content is 1.4 ML determined by simulation. The interference pattern of this sample is clear, superlattice peaks are well defined, as are fringes in between; consequently, the structural quality of this sample is good. The sample that is grown with the 550°C step exhibits an interference pattern with fewer details; oxygen dose for SiO_x layers is 1.56×10^{-5} mbar·s . Fringes are less pronounced and the superlattice peaks are broadened. The details are not distinct enough to simulate the sample properly, but the position of the superlattice peaks is moved to larger angles; therefore more oxygen content is suspected in the SiO_x layers. The 550°C step method increases the oxygen content in the SiO_x layers, but the structural quality of the sample is sacrificed. Without the step, the structural quality is increased. This is probably caused by lower oxygen content due to the higher SiO desorption rate resulting from the higher substrate temperature directly after oxide growth. Then again, the 550°C step could cause stronger island growth so that the remaining time is not sufficient to

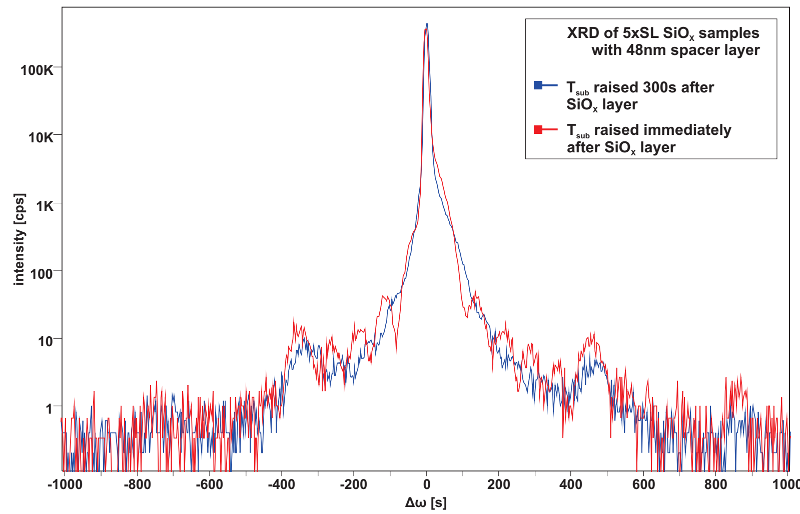

Figure 5.26: XRD of two samples with 5x SL Si/SiO_x structure. Spacer layers are 48 nm for both. First sample (blue) is grown with a 300 s step after oxide growth, before T_{Sub} is raised. Second sample (red) is grown without the extra step.

smooth the surface out. The 550°C step method is not adequate to reduce spacer layer thickness.

The growth procedure without the 550°C step is used for a superlattice with 20 repetitions. Substrate temperature for silicon is 700°C and for oxygen 550°C, spacer layers are 32 nm, oxygen dose is 1.64×10^{-5} mbar·s . Figure 5.27 shows a XRD measurement including a simulation. From simulation the oxygen content is determined to 1.03 ML. Superlattice peaks are well defined in the measurement, but fringes on the other hand are hard to identify and are not used to fit the simulation. Intensity of scan and simulation differ by a large degree; this might be caused by inhomogeneity of the spacer layers throughout the twenty repetitions. From AFM measurements, the roughness is determined to RMS = 269 pm, which attests to a very smooth surface. It is an excellent value for twenty superlattice repetitions and proves that the surfaces are completely regenerated before the next oxide layer (see Figure 5.25(b)). XRD measurement and simulation indicate overgrowth of twenty suboxide layers with monocrystalline silicon.

Discussion

For oxygen content of up to 1.4 ML, $T_{sub,Si}$ can be higher than 620°C. In order to produce smooth surfaces before the SiO_x layer, spacer thickness needs to be $\sim$ 50 nm. For higher oxygen concentration, $T_{sub,Si}$needs to be lowered to prevent SiO desorption from the sample. At 550°C, more oxygen can be incorporated and stays in the layer, but structural quality of the sample is sacrificed.

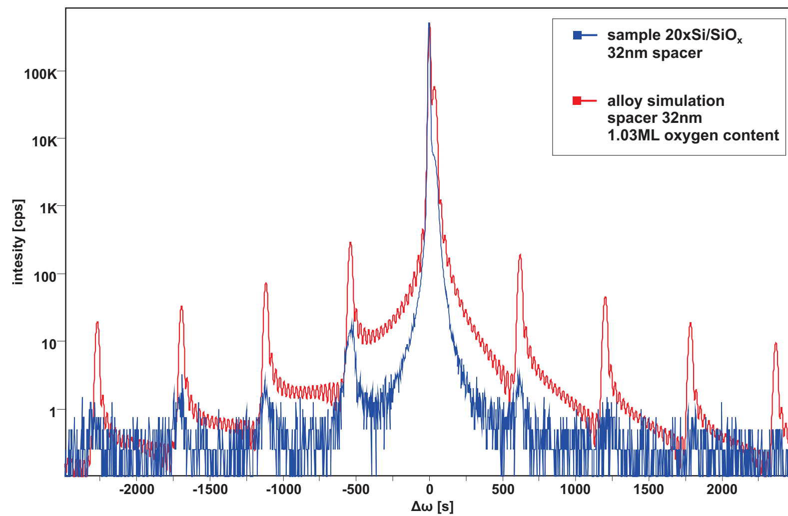

Figure 5.27: Sample with 20×SL of Si/SiO_x . ω-2Θ-scan (blue) and simulation with alloy model (red). Spacer layer is 32 nm, oxygen dose $1.64{\times}10^{-5}$ and oxygen content 1.03 ML determined by simulation.

When smooth surfaces are desired, so that defects are not intensified by each SiO_x layer, $T_{sub,Si}$ has to be increased. Raising the substrate temperature should be started directly after oxide growth. This leads to higher SiO desorption rates, and thus lower oxygen content, but structural quality is improved significantly. By these means a 20×Si/SiO_x superlattice with spacer thickness 32 nm, very smooth surface (269 pm) and oxygen content of 1.03 ML is produced.

These studies could not determine optimized growth parameters for all Si/SiO_x multilayer structures. Several parameters create opposing effects on Si/SiO_x structures. In order to obtain high structural quality, priorities for the sample have to be defined and growth procedure adjusted accordingly. For samples that do not need extreme values for oxygen content or spacer thickness substrate temperatures of 700°C for silicon and 550°C for oxide have proven effective in producing high quality crystals.

5.2.3 Further Analysis

Thermal Stability

For measurements and future applications, thermal stability of the Si/SiO_x structures is important. Temporal stability is of less concern for materials such as silicon and silicon oxide under standard conditions, as these materials have been investigated thoroughly and are well known to be stable over time. High temperatures, on the other hand, can

induce diffusion and reorganization of the crystal structure, especially at interfaces. Several groups have shown that Si/SiO_2 interface includes several oxidation states of silicon (from 1+ to 4+) [Him88; Ent98; Gru87; Kei99]. These states might by susceptible to high temperatures. To investigate the characteristics of the Si/SiO_x structures exposed to high temperatures, samples are annealed and thereafter measured with XRD. Annealing is carried out in a rapid thermal annealing (RTA) furnace for five minutes at 600°C, 700°C, 800°C, 900°C and 1000°C, by courtesy of Lehrstuhl für Technische Physik, Universität Würzburg. Following the RTA process, the samples are measured with XRD. Figure 5.28 shows ω-2Θ-scans of sample Si098 (used as reference in previous sections) before RTA and after 600°C and 1000°C annealing. Offsets in the scans are removed to improve comparability of the data. All scans show the same features, peaks are at the same angular distance from the substrate, fringe period and the peak to valley ratio are identical. Slight differences in intensity between the measurements are caused by the necessary adjustments before each measurement is performed, and are not correlated to sample properties. Considering the natural spread of the measurements caused by the adjustments, there are no differences between the diffraction pattern before and after thermal annealing. So far Si/SiO_x structures have shown a high structural stability when exposed to high temperatures. This is likely correlated to the SiO_x layer having, to a large extend a crystalline structure. However, long term studies need to be performed to validate the results in order to draw general conclusions.

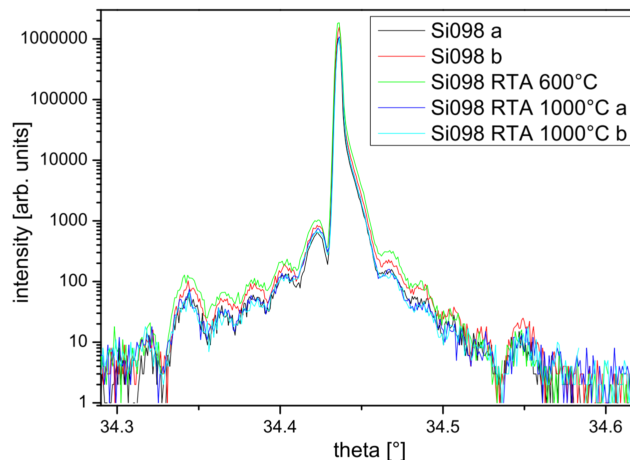

Figure 5.28: ω-2Θ-scans of sample Si098 before RTA and after 600°C and 1000°C annealing. Scans before RTA (Si098 a and b) and after 1000°C are performed twice to illustrate the data spread. Considering the spread, all scans are identical; slight differences in intensity are caused by diffractometer calibration for each sample.

Processing and Electrical Measurement

For some measurements it is necessary to process the samples. Processes for c-Si, a-Si and SiO_2 are well known, tested and used in the semiconductor industry. In Robert Hull's book, many are described and further references are given [HI99, chap. 16-17]. However, these processes are developed for thick layers compared with the SiO_x layer thickness, and thus might influence the layers. Some SiO_x multilayer samples are processed in a cooperation with the Institute für Halbleitertechnik of the TU Braunschweig (within the framework of the DFG SPP1386). The Institute für Halbleitertechnik has long time experience with processing silicon samples. For these samples, reactive ion etching (RIE) at cryogenic temperatures is used. A simple structure is chosen to test the feasibility: a square with 100 µm side length. Figure 5.29 shows SEM pictures of etched structures: magnifications are 40k×, 30k× and 70k× for (a), (b) and (c) respectively. Subfigure (b) shows the reference sample of pure silicon. The side walls are clean; some over-etching occurred because of the isotropic etching of RIE. Subfigures (a) and (c) show a SiO_x 5×superlattice with spacer layer thickness $d = 71.5$ nm, determined with XRD. Growth parameters of this sample are $T_{sub,O}$=570°C, $T_{sub,Si}$=620°C and oxygen dose 9.0×10^{-6} mbar·s . Over-etching also occurred on this sample, but below the surface features that resemble equidistant terraces are visible. Average distance between the features is 68 nm±1 nm (from 5.29(c)); the error is the standard deviation of all spacer layers. The real measurement error, however, is somewhat larger, as account has to be taken of the tilt of the sample and the error by setting the marker on the image. Overall, the error is closer to ±4 nm. Therefore, the measurements by SEM and XRD are in agreement.

The lower terraces in the images (a) and (c) have a larger overhang than the ones above them. In the image of the pure silicon sample (b), the side wall looks more vertical and unstructured, so the slope of the terraces is not an artifact from RIE. But the employed RIE process is optimized for Si and not SiO_2 or SiO_x . The cause of the slope and the terraces are the SiO_x layers, which have a higher resistance against RIE than pure Si. Therefore, in order to process Si/SiO_x layer systems the RIE process has to be modified or different methods have to be applied, such as purely physical etching processes. On the other hand, this characteristic of Si/SiO_x layer systems could be exploited to produce spatial confinements in nano pillars by etching. In any case, the samples show that processing of Si/SiO_x multilayer structures can be done, even though standard silicon processes have to be adjusted to the material system for optimized results.

The next step towards electrical characterization is contacting the samples. Contact pads are created on the sample with photo lithography and metallization. Metal deposition consists of 10 nm titanium and 90 nm gold. Samples are contacted with needles to the measurement setup, which consists of a probe station with micro manipulators connected to a HP 4145B Semiconductor Analyzer. In order to test the setup, a sample is processed from a p-doped silicon wafer. Figure 5.30b shows a characteristic curve for the not

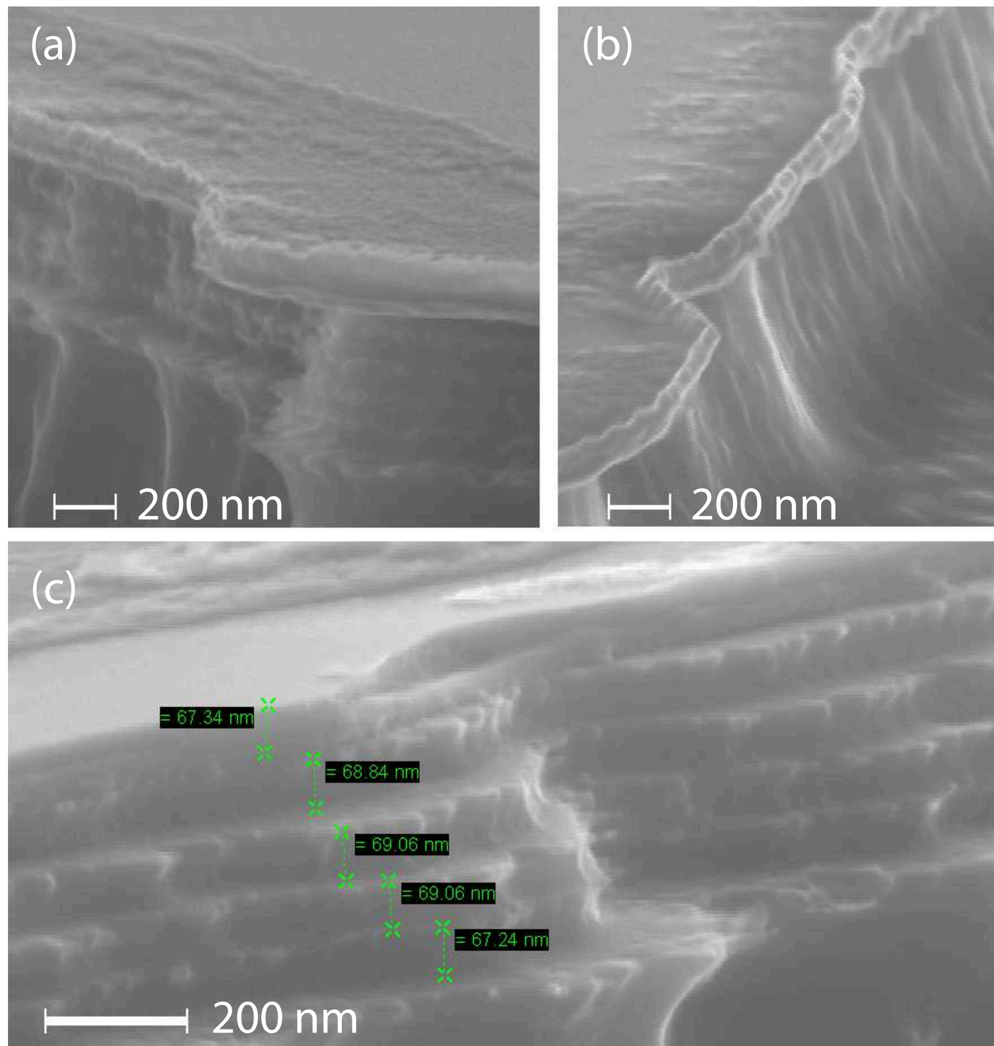

Figure 5.29: SEM images of a Si/SiO_x multilayer structure (a), (c) and a silicon reference sample (b) processed with RIE. Magnifications are 40k×, 30k× and 70k× for (a),(b) and (c) respectively. Terraces in image (a) and (b) are caused by the SiO_x layers. The different chemical environment of the SiO_x layers influences the RIE process.

tempered p-doped silicon (black). Over the range of measurement the I-V curve is not linear; that means the resistance is changing and the contact is not ohmic but Schottky-like. To improve the contacts, the sample is tempered for ten minutes at 100°C, 150°C and 200°C, depicted as red, green and blue in Figure 5.30a. With increasing temperature the curves become steeper until, for 200°C, the curve is linear in the range of measurement. Figure 5.30b shows the V-I curve of the sample tempered for ten minutes at 250°C. In the range of 0 A to 0.1 A, the curve is linear and thus the resistance constant; the resistivity is then calculated to $\rho = 0.045\,\Omega$cm. Compared with the specifications provided by the manufacturer (resistivity 0.01 – 0.02 Ωcm), the measured resistivity is a factor 2–4 too high. If some of the metal–semiconductor interface barrier has not been removed by tempering, the elevated resistivity could be explained.

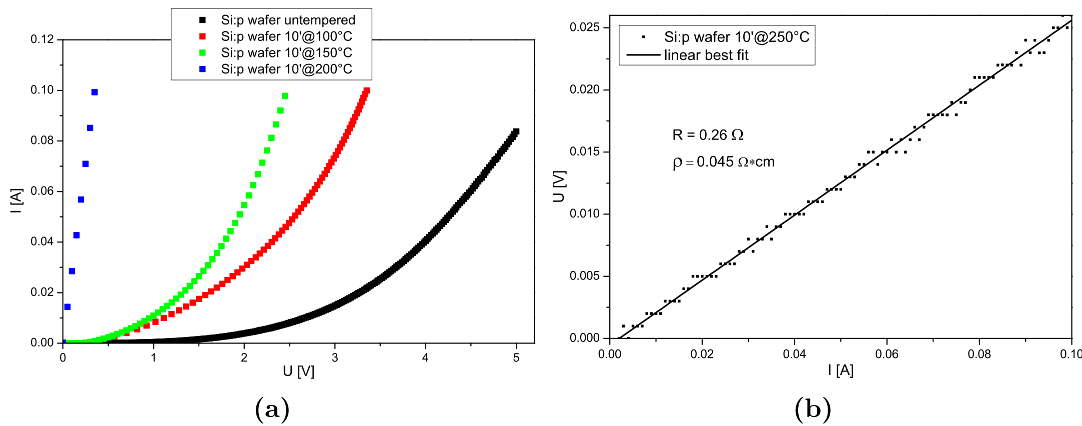

Figure 5.30: Resistivity measurements of a p-doped silicon wafer. In (a) the I-V curve is shown for the not-tempered sample (black), tempered for 10' at 100°C (red), for 10' at 150°C (green) and tempered for 10' at 200°C. In (b) the U-I curve for the range I=0 − 0.1 A is shown (annealed at 250°C). In this range the curve is linear and the resistivity can be calculated ($\rho = 0.045\,\Omega$cm).

A Si/SiO_x multilayer sample (10×SL; 72 nm spacer layers; oxygen dose 6.6×10^{-6} mbar s) is processed for electrical measurement. Within the range of 0 A to 0.1 A the characteristic curve is linear but outside that range it is not. The sample is p-doped (Boron) during growth ($p \approx 2 \times 10^{18}\,\frac{1}{\text{cm}^3}$); this level is the same level of doping as wafers used as substrates. Doping concentration is calibrated by electrochemical capacitance voltage profiling. Resistivity of the sample is 0.052 Ωcm. The resistivity should be equal to that of the silicon wafer because the doping level is set to match the wafer. Differences in the measurement are caused by the contact pads. The metal–semiconductor junction is not purely ohmic yet and causes difficulties in the measurement. In order to characterize the Si/SiO_x samples electrically, the process for the contact pads has to be improved to a level that the results are reliable and reproducible.

Heat Conductivity

Since Si/SiO_x superlattice structures are of interest for thermoelectric research, the heat conductivity of the samples is studied. For measurements of this property special equipment is necessary. A cooperation partner, the Lehrstuhl für Halbleitertechnik of the TU Braunschweig, has laboratories equipped, and expert staff, to perform such measurements. Figure 5.31 shows the results of the study, courtesy of A. Stranz. The heat conductivity is measured and normalized to pure silicon, with a reference sample. Two samples are measured: a 4×SL and a 10×SL Si/SiO_x structure (sample structure is depicted in Fig 5.31). Figure 5.31 shows that with increasing SL repetitions the heat conductivity is lowered. However, the error of the heat conductivity measurement is quite large in two of the measurements; it can be traced back to the measurement setup. The employed setup is developed for measurements of nano pillar systems [Str11], and not for very thin layer systems like the Si/SiO_x samples. Therefore, the quantitative influence of the Si/SiO_x superlattice on the heat conductivity cannot be determined. But the results point towards Si/SiO_x superlattices having an influence on the heat conductivity. This could be caused by the disorder that is incorporated with the SiO_x layer and disturbs the phonons traveling perpendicular to the superlattice. In order to reduce the error of the measurement and determine the exact influence of the superlattice on the heat conductivity, samples with much higher SL repetitions (≤ 100) should be measured. Further, other methods, such as the 3-Omega-method[6], could be used to explore the thermoelectric properties of the Si/SiO_x structures.

Raman Spectroscopy

Information on the crystal structure of the SiO_x layer is hard to obtain, as mentioned in section 5.1. By probing the vibration modes, information of the Si–O bonds in the SiO_x layer can be gained. Raman spectroscopy is the most suitable tool for this investigation, because in addition information on strain and crystal orientation could be extracted from the data. In order to increase the sensitivity of the measurement, superlattice structures are probed, because the absolute oxygen content is a multiple of that of a single layer.

The spectra of the samples is expected to be dominated by the well-known spectra of silicon (see [PFA67; YC10]). But additional peaks from SiO_2 might be visible, such as the D2 defect mode ($605\,cm^{-1}$), deformation modes ($797\,cm^{-1}$), TO asymmetric stretching ($1060\,cm^{-1}$) or further modes. These peaks are associated with SiO_2 glasses and the data are taken from Henderson et al., Galeener and Geissberger, and Pasquarello and Car [Hen09; GG83a; GG83b; PC98].

6 Cahill and Pohl describe the development of this method in[CP87]

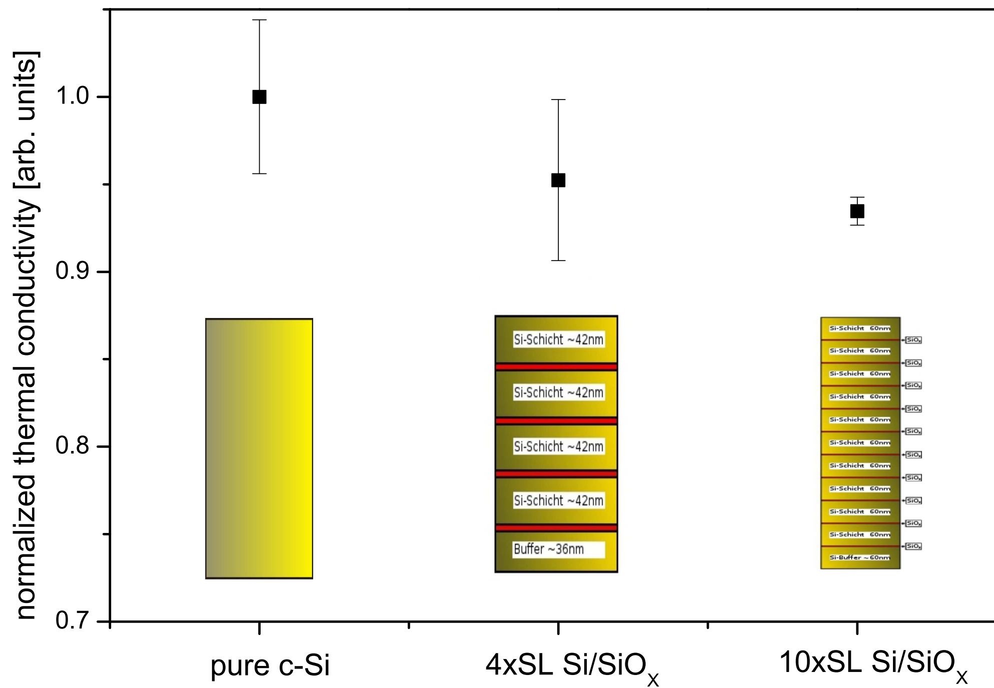

Figure 5.31: Heat conductivity normalized to pure c-Si. Heat conductivity is reduced slightly by the superlattices, although the error of the measurement is quite large. Courtesy of A. Stranz, TU Braunschweig.

Investigation is performed by the Raman spectroscopy group of Prof. Geurts of the Lehrstuhl für Experimentelle Physik III at the Universität Würzburg. The samples are measured with three different laser wavelengths (He-Ne laser: 633 nm, Nd:YAG laser: 532 nm and 473 nm) and different power. In Figure 5.32(a), measurement of a $4\times Si/SiO_x$ SL, a $4\times Si/SiGe_{21,5\%}$ SL and a Si reference is shown. The peaks for silicon are clearly visible for all samples—in particular, the 1LO-phonon peak at $520\,cm^{-1}$ and the two-phonon peak at $964\,cm^{-1}$. All three spectra in the Figure are plotted with normalized intensities; for this the 2TA(X)-Si-mode has been used. Thereby, the sensitivity is increased because intensity of the 2TA(X)-mode is only about 1% of the silicon 1LO-phonon. The spectra in red are from a $Si/SiGe_{21.5\%}$ $4\times$superlattice; the peaks at $432\,cm^{-1}$, $406\,cm^{-1}$, $281\,cm^{-1}$ and around $243\,cm^{-1}$ correspond to the SiGe alloy. Apart from that, the spectra show no deviation from silicon, no oxygen peaks or shifts that could be associated with Si–O bonds. Furthermore, folded phonon modes from the superlattice could not be observed because the SL period is too large and thus the phonon mode too close to the laser line.

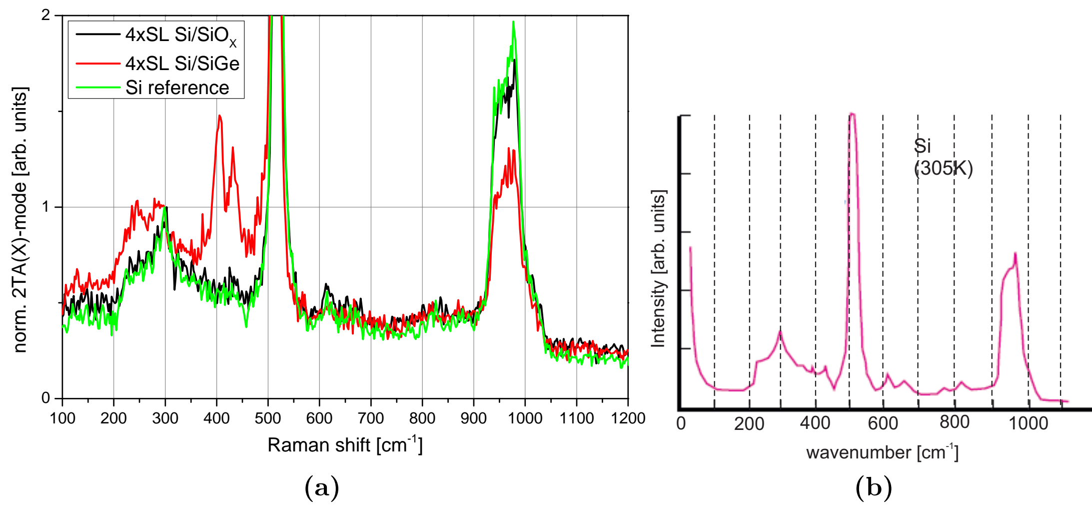

Figure 5.32: (a) Raman measurement of 4×superlattices, one Si/SiO_x , the other Si/SiGe (Ge content 21.5%), and a Si reference sample, measured at a wavelength of 473 nm. Intensities are normalized to the 2TA(X)-mode. No significant difference between the Si/SiO_x and the Si reference is visible. The SiGe alloy sample shows peaks associated with SiGe alloy. Measurements courtesy of C. Kehl. (b) Reference silicon spectrum from Yu and Cardona [YC10, p.389].

5.3 Summary

SiO_x layers have been grown and overgrown with mono crystalline Si, on Si(100) substrates with MBE technology. The overgrowth has been investigated in situ with RHEED and ex situ with XRD, AFM and STEM. From the STEM analysis it could be shown that the oxygen incorporation into the silicon is not homogeneous, but within the SiO_x layer of about 1 nm thickness regions with higher and lower oxygen concentration exist. Investigations with RHEED and AFM show that the silicon overgrowth of the oxide layer starts in an island growth mode. By choosing the right MBE parameter it is possible to smooth the islands in the further growth process, so that after certain time the surface is two-dimensional. For this process the substrate temperature for Si growth $T_{sub,Si}$ is the most crucial factor. At higher temperatures the smoothing process is much faster, so that the Si spacer layer can be reduced by almost half (to $\sim$ 30 nm); this is due to higher diffusivity of the Si surface atoms and partial decomposition of SiO_x to volatile SiO.

Further on, the expertise on single SiO_x layers and their overgrowth has led to the growth of Si/SiO_x superlattice structures. By optimizing the MBE parameters, a superlattice structure with 20 repetitions and a spacer layer of only 32 nm has been grown. Substrate temperature of $T_{sub,Si} = 700°C$ and $T_{sub,O} = 550°C$ were used for the superlattice structure. Oxygen coverage was determined to be 1.03 mono layers. In order to minimize the island

growth, the temperature ramp from $T_{sub,Si}$ to $T_{sub,O}$ has to be started right after the oxide layer.

However, with lower $T_{sub,Si}$, superlattice structures with good crystal quality have also been produced. At $T_{sub,Si} = 620°C$, the spacer layer had to be increased to about 50 nm to ensure a flat surface before the oxide spike.

Oxygen coverage of the samples has been determined with XRD measurements and simulations, which have been calibrated with SIMS. The strain of the layer in the XRD measurements has been simulated by adjusting the lattice mismatch of SiO_x in the simulations. Furthermore, the investigations showed that the chemical contrast of the oxygen in the SiO_x layer has no noteworthy influence on the simulations. Evaluation of the actual structure of SiO_x and incorporation of oxygen in Si could not be performed.

The oxygen coverage, determined with simulations, scales linearly with the oxygen dose. Within the dose range used the predicted saturation of the oxygen coverage at high doses could not be observed. The predicted relation of the oxygen coverage and $T_{sub,O}$ [Sti02a] could not be observed either.

The oxygen content determined by XRD and the oxygen content measured with SIMS differ slightly from each other. This could be caused by limitations of the simulation model and uncertainties when fitting the simulation to the XRD data. Also, changes in the chemical environment could lead to deviations in the SIMS results. Nonetheless, the oxygen coverage mainly depends on the oxygen dose. In the samples the coverage was determined to be between 0.6 ML and 2.4 ML. Because of the uncertainty of the exact SiO_x structure, the coverage cannot be converted to absolute numbers, unless assumptions are made on the SiO_x . For the SiO_x thickness one can assume 1 nm, backed up by the TEM measurements; with that the absolute oxygen concentration in the samples lies between 8% and 33%. With the data of the oxygen coverage it has been shown that for high temperatures the silicon substrate temperature $T_{sub,Si}$has a large influence on the oxygen coverage. For $T_{sub,Si} \geq 700°C$, the SiO desorption from the surface is a dominant process, whereas for temperatures smaller than 620°C the influence is negligible.

In the course of this work a large parameter space for SiO_x layer growth has been explored. However, universally valid parameters for SiO_x growth and c-Si overgrowth could not been determined. In fact, the growth parameters strongly depend on purpose and layout of the sample. For Si/SiO_x multilayer structure that do not need a very high oxygen content (>2 ML) or very thin spacer layers (< 20 nm) the growth at $T_{sub,O} = 550°C$ and $T_{sub,Si} = 700°C$ has been proven to produce high crystal quality samples.

Studying the structural stability of the samples with RTA has shown that the layers are very stable towards high temperatures. Annealing for five minutes in up to 1000°C had no influence on the samples that could be detected with XRD. On the other hand, reactive ion etching shows a certain selectivity on the material. SEM images of processed structures show a higher resistance of the SiO_x layer against etching than silicon. Therefore, in order

to process Si/SiO_x multilayers, the process has to be adjusted to the material in order to get very good results.

Electrical contacts have been established on the samples, although the stability and reproducibility were not as good as required for electrical characterization. Here, too, adjustments to the processes are needed in order to receive reliable results.

Optical measurements, namely Raman spectroscopy, have been performed to gather more detailed information on the structure of SiO_x . Unfortunately, the data have shown no sign of oxygen or influence from the SL structure.

With regard to possible future applications, the heat conductivity of the Si/SiO_x structures has been investigated on some samples. The results lead to the conclusion that the SL influences the heat conductivity. A slight reduction of the heat conductivity has been measured, but the data need confirmation to be conclusive.

Bibliography

[ALB91] P. Avouris, I.-W. Lyo, and F. Bozso. “Atom-resolved surface chemistry: The early steps of Si(111)-7×7 oxidation”. In: *J. Vac. Sci. Technol. B* 9 (2) (1991). Fifth international conference on scanning tunneling microscopyl spectroscopy, pp. 424–430. DOI: 10.1116/1.585584.

[Aza11] S. Azatyan et al. “Variable termination of MnSi/Si(111) $\sqrt{3} \times \sqrt{3}$ films and its effect on surface properties”. In: *Surf. Sci.* 605 (34) (2011), pp. 289–295. ISSN: 0039-6028. DOI: 10.1016/j.susc.2010.10.031.

[Ban10] K. Bangert. “Thermopower!” In: *E-Futures* 47 (2010), pp. 1–6.

[Beh81] R. Behrisch, ed. *Sputtering by Particle Bombardment I*. Vol. 47. Topics in Applied Physics. ISBN 3-540-10521-2. Springer Verlag Berlin Heidelberg New York, 1981.

[BRW87] A. Benninghoven, F. Rüdenauer, and H. Werner. *Secondary Ion Mass Spectrometry*. Ed. by P. Elving and J. Winefordner. Vol. 86. Chemical Analysis. Wiley-Interscience, 1987.

[Bor33] B. Borén. In: *Arkiv. Kemi. Mine. Geol. A* 11 (10) (1933), pp. 1–28.

[CP87] D. G. Cahill and R. O. Pohl. “Thermal conductivity of amorphous solids above the plateau”. In: *Phys. Rev. B* 35 (8 Mar. 1987), pp. 4067–4073. DOI: 10.1103/PhysRevB.35.4067.

[Cha89] Y. J. Chabal et al. “Infrared spectroscopy of Si(111) and Si(100) surfaces after HF treatment: Hydrogen termination and surface morphology”. In: *Journal of Vacuum Science & Technology A: Vacuum, Surfaces, and Films* 7 (3) (1989), pp. 2104–2109. DOI: 10.1116/1.575980.

[Chi90] A. Chichagov et al. “Information-calculating system on Crystal Structure data for Minerals (MINCRYST)”. In: *Kristallografiya* 35 (3) (1990). in Russian, pp. 610–616.

[Cho70] A. Y. Cho. “Morphology of epitaxial growth of GaAs by a molecular beam method: The observation of surface structures”. In: *J. Appl. Phys.* 41 (7) (1970), pp. 2780–2786. DOI: 10.1063/1.1659315.

[Cho99] A. Y. Cho. “How molecular beam epitaxy (MBE) began and its projection into the future”. In: *J. Cryst. Growth* 201-202 (0) (1999), pp. 1–7. ISSN: 0022-0248. DOI: 10.1016/S0022-0248(98)01265-2.

[CF90] A. X. Chu and W. B. Fowler. “Theory of oxide defects near the Si-SiO_2 interface”. In: *Phys. Rev. B* 41 (8 Mar. 1990), pp. 5061–5066. DOI: 10.1103/PhysRevB.41.5061.

[Cti02] G. Ctistis et al. “Growth and structural properties of Mn films on Si(111)-($\sqrt{3} \times \sqrt{3}$):Bi”. In: *J. Magn. Magn. Mater.* 240 (1-3) (2002). 4th International Symposium on Metallic Multilayers, pp. 420–422. ISSN: 0304-8853. DOI: 10.1016/S0304-8853(01)00881-2.

[CS01] B. Cullity and S. Stock. *Elements of x-ray diffraction*. Ed. by B. Cullity and S. Stock. Pearson education. Prentice Hall, 2001. ISBN: 9780201610918.

[DNE87] M. P. D’Evelyn, M. M. Nelson, and T. Engel. “Kinetics of the adsorption of O_2 and of the desorption of SiO on Si(100): A molecular beam, XPS, and ISS study”. In: *Surf. Sci.* 186 (1-2) (1987), pp. 75–114. ISSN: 0039-6028. DOI: 10.1016/S0039-6028(87)80037-7.

[DME08] DME. *DualScope™ /Rasterscope™ Scanning Probe Microscopes Operation Manual*. DME - Danish Micro Engineering A/S. DK-2730, Herlev, Denmark, May 2008.

[DM00] J. Dabrowski and H.-J. Müssig. *Silicon Surfaces and Formation of Interfaces: Basic Science in the Industrial World*. World Scientific, Sept. 2000, p. 550. ISBN: 978-981-02-3286-3.

[Day09] C. Day. “Exotic spin textures show up in divers materials”. In: *Phys. Today* 62 (4) (Apr. 2009), p. 12.

[DEP64] J. P. Dismukes, L. Ekstrom, and R. J. Paff. “Lattice parameter and density in germanium-silicon alloys”. In: *The Journal of Physical Chemistry* 68 (10) (1964), pp. 3021–3027. DOI: 10.1021/j100792a049.

[DL03] N. Doiron-Leyraud et al. “Fermi-liquid breakdown in the paramagnetic phase of a pure metal”. In: *Nature* 425 (6958) (Oct. 2003), pp. 595–599. ISSN: 0028-0836. DOI: 10.1038/nature01968.

[Eng93] T. Engel. “The interaction of molecular and atomic oxygen with Si(100) and Si(111)”. In: *Surf. Sci. Rep.* 18 (4) (1993), pp. 93–144. ISSN: 0167-5729. DOI: 10.1016/0167-5729(93)90016-I.

[EBE92] J. Engstrom, D. Bonser, and T. Engel. “The reaction of atomic oxygen with Si(100) and Si(111): II. Adsorption, passive oxidation and the effect of coincident ion bombardment”. In: *Surf. Sci.* 268 (1-3) (1992), pp. 238–264. ISSN: 0039-6028. DOI: 10.1016/0039-6028(92)90966-A.

[Eng91] J. Engstrom et al. “The reaction of atomic oxygen with Si(100) and Si(111): I. Oxide decomposition, active oxidation and the transition to passive oxidation”. In: *Surf. Sci.* 256 (3) (1991), pp. 317–343. ISSN: 0039-6028. DOI: 10.1016/0039-6028(91)90875-S.

[Ent98] Y. Enta et al. “Real-time measurements of Si $2p$ core level during dry oxidation of Si(100)”. In: *Phys. Rev. B* 57 (11 Mar. 1998), pp. 6294–6296. DOI: 10.1103/PhysRevB.57.6294.

[EGN96] M. M. R. Evans, J. C. Glueckstein, and J. Nogami. “Epitaxial growth of manganese on silicon: Volmer-Weber growth on the Si(111) surface”. In: *Phys. Rev. B* 53 (7 Feb. 1996), pp. 4000–4004. DOI: 10.1103/PhysRevB.53.4000.

[Fie99] R. Fiederling et al. “Injection and detection of a spin-polarized current in a light-emitting diode”. In: *Nature* 402 (6763) (Dec. 1999), pp. 787–790. ISSN: 0028-0836.

[Fuo88] P. H. Fuoss et al. “X-ray scattering studies of the Si-SiO_2 interface”. In: *Phys. Rev. Lett.* 60 (7 Feb. 1988), pp. 600–603. DOI: 10.1103/PhysRevLett.60.600.

[GG83a] F. L. Galeener and A. E. Geissberger. “Vibrational dynamics in ^{30}Si-substituted vitreous SiO_2”. In: *Phys. Rev. B* 27 (10 May 1983), pp. 6199–6204. DOI: 10.1103/PhysRevB.27.6199.

[GG83b] A. E. Geissberger and F. L. Galeener. “Raman studies of vitreous SiO_2 versus fictive temperature”. In: *Phys. Rev. B* 28 (6 Sept. 1983), pp. 3266–3271. DOI: 10.1103/PhysRevB.28.3266.

[GDB87] C. A. Gogol, R. A. Deutschman, and J. C. Bean. “Automatic process control for artificially layered structures”. In: *Journal of Vacuum Science & Technology A: Vacuum, Surfaces, and Films* 5 (4) (1987), pp. 2077–2080. DOI: 10.1116/1.574923.

[Gre03] T. Grehl. “Improvement in TOF-SIMS Instrumentation for Analytical Application and fundamental Research”. PhD thesis. Westfälische Wilhelms-Universität Münster, 2003.

[Gru87] P. J. Grunthaner et al. "The localization and crystallographic dependence of Si suboxide species at the SiO_2/Si interface". In: *J. Appl. Phys.* 61 (2) (1987), pp. 629–638. DOI: 10.1063/1.338215.

[Har05] T. Harman et al. "Nanostructured thermoelectric materials". English. In: *Journal of Electronic Materials* 34 (5 2005), pp. L19–L22. ISSN: 0361-5235. DOI: 10.1007/s11664-005-0083-8.

[Hen09] G. S. Henderson et al. "The structure of GeO_2-SiO_2 glasses and melts: A Raman spectroscopy study". In: *J. Non-Cryst. Solids* 355 (8) (Apr. 2009), pp. 468–474. ISSN: 0022-3093. DOI: 10.1016/j.jnoncrysol.2009.01.024.

[HSM85] M. A. Henesian, C. D. Swift, and J. R. Murray. "Stimulated rotational Raman scattering in nitrogen in long air paths". In: *Opt. Lett.* 10 (11) (Nov. 1985), pp. 565–567. DOI: 10.1364/OL.10.000565.

[HS96] M. A. Herman and H. Sitter. *Molecular beam epitaxy.* Ed. by M. A. Herman and H. Sitter. 2nd. Vol. 7. Springer series in materials science. Springer, 1996, p. 453. ISBN: 3-540-60594-0.

[Her95] H. Herzog. "Properties of strained and relaxed silicon germanium". In: ed. by E. Kasper. 2nd ed. 12. INSPEC, Institution of electrical engineers London, 1995, p. 49.

[HKT09] S. Higashi, P. Kocán, and H. Tochihara. "Reactive epitaxial growth of MnSi ultrathin films on Si(111) by Mn deposition". In: *Phys. Rev. B* 79 (20 May 2009), p. 205312. DOI: 10.1103/PhysRevB.79.205312.

[Him88] F. J. Himpsel et al. "Microscopic structure of the SiO_2/Si interface". In: *Phys. Rev. B* 38 (9 Sept. 1988), pp. 6084–6096. DOI: 10.1103/PhysRevB.38.6084.

[HH83] G. Hollinger and F. J. Himpsel. "Multiple-bonding configurations for oxygen on silicon surfaces". In: *Phys. Rev. B* 28 (6 Sept. 1983), pp. 3651–3653. DOI: 10.1103/PhysRevB.28.3651.

[HH84] G. Hollinger and F. J. Himpsel. "Probing the transition layer at the SiO_2-Si interface using core level photoemission". In: *Appl. Phys. Lett.* 44 (1) (1984), pp. 93–95. DOI: 10.1063/1.94565.

[Hol87] G. Hollinger et al. "Anomalous bonding in SiO2 at the SiO2–Si interface". In: *Philosophical Magazine Part B* 55 (6) (1987), pp. 735–746. DOI: 10.1080/13642818708218377.

[Hor06] M. Hortamani. “Theory of Adsorption, Diffusion and Spinpolarization of Mn on Si(001) and Si(111) Substrates”. PhD thesis. Freie Universitaet Berlin, 2006.

[Hor08] M. Hortamani et al. “Exchange interactions and critical temperature of bulk and thin films of MnSi: A density functional theory study”. In: *Phys. Rev. B* 78 (10 Sept. 2008), p. 104402. DOI: 10.1103/PhysRevB.78.104402.

[HKS07] M. Hortamani, P. Kratzer, and M. Scheffler. “Density-functional study of Mn monosilicide on the Si(111) surface: Film formation versus island nucleation”. In: *Phys. Rev. B* 76 (23 Dec. 2007), p. 235426. DOI: 10.1103/PhysRevB.76.235426.

[Hua07] B. Huang et al. “35% magnetocurrent with spin transport through Si”. In: *Applied Physics Letters* 91 (5), 052501 (2007), p. 052501. DOI: 10.1063/1.2767198.

[HI99] R. Hull and INSPEC. *Crystalline Silicon*. EMIS Datareviews Series. Inst. of Engineering & Technology, 1999, p. 1016. ISBN: 978-0-85-296933-5.

[IC04] A. Ichimiya and P. I. Cohen. *Reflection High Energy Electron Diffraction*. Ed. by A. Ichimiya and P. I. Cohen. Cambridge University Press, 2004, p. 353. ISBN: 978-0-521-45373-8. DOI: 10.2277/0521453739.

[Inc87] L. Incoccia et al. “The adsorption site of oxygen on Si(100) determined by SEXAFS”. In: *Surf. Sci.* 189-190 (0) (1987), pp. 453–458. ISSN: 0039-6028. DOI: 10.1016/S0039-6028(87)80467-3.

[Ish85] M. Ishida et al. “Crystal chirality and helicity of the helical spin density wave in MnSi. II. Polarized neutron diffraction”. In: *Journal of the Physical Society of Japan* 54 (8) (1985), pp. 2975–2982. DOI: 10.1143/JPSJ.54.2975.

[Ish76] Y. Ishikawa et al. “Helical spin structure in manganese silicide MnSi”. In: *Solid State Commun.* 19 (6) (1976), pp. 525–528. ISSN: 0038-1098. DOI: 10.1016/0038-1098(76)90057-0.

[JHC97] S. C. Jain, A. H. Harker, and R. A. Cowley. “Misfit strain and misfit dislocations in lattice mismatched epitaxial layers and other systems”. In: *Philos. Mag. A* 75 (6) (1997), pp. 1461–1515. DOI: 10.1080/01418619708223740.

[JP04] T. Jeong and W. E. Pickett. “Implications of the B20 crystal structure for the magnetoelectronic structure of MnSi”. In: *Phys. Rev. B* 70 (7 Aug. 2004), p. 075114. DOI: 10.1103/PhysRevB.70.075114.

[JE92] K. E. Johnson and T. Engel. “Direct measurement of reaction kinetics for the decomposition of ultrathin oxide on Si(001) using scanning tunneling microscopy”. In: *Phys. Rev. Lett.* 69 (2 July 1992), pp. 339–342. DOI: 10.1103/PhysRevLett.69.339.

[Jon10] F. Jonietz et al. “Spin transfer torques in MnSi at ultralow current densities”. In: *Science* 330 (6011) (Dec. 2010), pp. 1648–1651. DOI: DOI:10.1126/science.1195709.

[Kah01] U. Kahler. “Darstellung, Charakterisierung und Oberflächenmodifizierung von Siliziumnanopartikeln in SiO_2”. PhD thesis. Martin-Luther-Universität Halle-Wittenberg, 2001.

[Kan99] C. Kaneta et al. “Structure and electronic property of Si(100)SiO_2 interface”. In: *Microelectron. Eng.* 48 (1-4) (1999), pp. 117–120. ISSN: 0167-9317. DOI: 10.1016/S0167-9317(99)00351-2.

[Kan08] J. Kang et al. “Direct and defect-assisted electron tunneling through ultrathin SiO_2 layers from first principles”. In: *Phys. Rev. B* 77 (19), 195321 (2008), p. 195321. DOI: 10.1103/PhysRevB.77.195321.

[Kar12a] E. A. Karhu et al. “Chiral modulations and reorientation effects in MnSi thin films”. In: *Phys. Rev. B* 85 (9 Mar. 2012), p. 094429. DOI: 10.1103/PhysRevB.85.094429.

[Kar10] E. Karhu et al. “Structure and magnetic properties of MnSi epitaxial thin films”. In: *Phys. Rev. B* 82 (18 Nov. 2010), p. 184417. DOI: 10.1103/PhysRevB.82.184417.

[Kar12b] E. A. Karhu. “Structural and Magnetic Properties of Epitaxial MnSi(111) Thin Films”. PhD thesis. Dalhousie University Halifax, 2012.

[Kas82] E. Kasper. “Growth kinetics of Si-molecular beam epitaxy”. In: *Applied Physics A: Materials Science & Processing* 28 (2 1982), pp. 129–135. ISSN: 0947-8396.

[Kei99] J. W. Keister et al. “Structure of ultrathin SiO_2/Si(111) interfaces studied by photoelectron spectroscopy”. In: *Papers from the 45th National Symposium of the American Vacuum Society* 17 (4) (1999), pp. 1250–1257. DOI: 10.1116/1.581805.

[Kit05] C. Kittel. *Einführung in die Festkörperphysik*. 14th. ISBN 3-486-57723-9. Oldenbourg, 2005, p. 754. ISBN: 3-486-27219-5.

[Kum04] A. Kumar et al. “Thin manganese films on Si(111)-(7×7): electronic structure and strain in silicide formation”. In: *J. Phys. D: Appl. Phys.* 37 (7) (2004), p. 1083.

[LLR87] M. Liehr, J. E. Lewis, and G. W. Rubloff. “Kinetics of high-temperature thermal decomposition of SiO_2 on Si(100)”. In: *Journal of Vacuum Science & Technology A: Vacuum, Surfaces, and Films* 5 (4) (1987), pp. 1559–1562. DOI: 10.1116/1.574564.

[Mag10] E. Magnano et al. “Ferromagnetic and ordered MnSi(111) epitaxial layers”. In: *Appl. Phys. Lett.* 96 (15), 152503 (2010), p. 152503. DOI: 10.1063/1.3392373.

[Mah93] J. E. Mahan et al. “Surface electron-diffraction patterns of beta-$FeSi_2$ films epitaxially grown on silicon”. In: *Journal of Applied Physics* 74 (3) (1993), pp. 1747–1761. DOI: 10.1063/1.354804.

[Mah07] S. Mahapatra. “Formation and properties of epitaxial CdSe/ZnSe quantum dots”. PhD thesis. Julius-Maximilians-Universität Würzburg, 2007.

[Mar93] L. Martinsson et al. “A test of different rotational Raman linewidth models: Accuracy of rotational coherent anti-Stokes Raman scattering thermometry in nitrogen from 295 to 1850 K”. In: *The Journal of Chemical Physics* 99 (4) (1993), pp. 2466–2477. DOI: 10.1063/1.466197.

[Men03] F. P. Mena et al. “Heavy carriers and non-Drude optical conductivity in MnSi”. In: *Phys. Rev. B* 67 (24 June 2003), p. 241101. DOI: 10.1103/PhysRevB.67.241101.

[Mor85] T. Moriya. *Spin fluctuations in itinerant electron magnetism.* Ed. by T. Moriya. Vol. 56. Springer series in solid-state science. Springer, 1985, p. 239.

[Mue09] S. Muehlbauer et al. “Skyrmion lattice in a chiral magnet”. In: *Science* 323 (5916) (2009), pp. 915–919. DOI: 10.1126/science.1166767.

[Nag99] T. Nagao et al. “Morphology of ultrathin manganese silicide on Si(111)”. In: *Surf. Sci.* 419 (2-3) (1999), pp. 134–143. ISSN: 0039-6028. DOI: 10.1016/S0039-6028(98)00771-7.

[NP08] R. B. Neder and T. Proffen. *Diffuse Scattering and Defect Structure Simulations.* International Union of Crystallography Book Series. Great Clarendon Street Oxford OX26DP: Oxford University Press, 2008, p. 228. ISBN: 978-0-19-923369-4.

[NP10] R. B. Neder and T. Proffen. *DISCUS Users Guide, Version 3.6.* Jan. 2010.

[Neu09] A. Neubauer et al. "Hall effect and magnetoresistance in MnSi". In: *Physica B* 404 (19) (2009). Proceedings of the International Conference on Strongly Correlated Electron Systems, pp. 3163–3166. ISSN: 0921-4526. DOI: 10.1016/j.physb.2009.07.055.

[Ohk92] K. Ohkubo et al. "SiO production from Si(100) and (111) surfaces by reaction with O2 beams". In: *Surf. Sci.* 260 (1-3) (1992), pp. 44 –52. ISSN: 0039-6028. DOI: 10.1016/0039-6028(92)90017-Z.

[Ohn99] Y. Ohno et al. "Electrical spin injection in a ferromagnetic semiconductor heterostructure". In: *Nature* 402 (6763) (Dec. 1999), pp. 790–792. ISSN: 0028-0836.

[Oht08] N. Ohtsu et al. "X-ray photoelectron spectroscopic studies on initial oxidation of iron and manganese mono-silicides". In: *Applied Surface Science* 254 (11) (2008), pp. 3288 –3294. ISSN: 0169-4332. DOI: 10.1016/j.apsusc.2007.11.005.

[Our87] A. Ourmazd et al. "Si→SiO_2 transformation: Interfacial structure and mechanism". In: *Phys. Rev. Lett.* 59 (2 July 1987), pp. 213–216. DOI: 10.1103/PhysRevLett.59.213.

[PFA67] J. H. Parker, D. W. Feldman, and M. Ashkin. "Raman Scattering by Silicon and Germanium". In: *Phys. Rev.* 155 (3 Mar. 1967), pp. 712–714. DOI: 10.1103/PhysRev.155.712.

[PC98] A. Pasquarello and R. Car. "Identification of Raman defect lines as signatures of ring structures in vitreous silica". In: *Phys. Rev. Lett.* 80 (23 June 1998), pp. 5145–5147. DOI: 10.1103/PhysRevLett.80.5145.

[PJL01] C. Pfleiderer, S. R. Julian, and G. G. Lonzarich. "Non-Fermi-liquid nature of the normal state of itinerant-electron ferromagnets". In: *Nature* 414 (6862) (Nov. 2001), pp. 427–430. ISSN: 0028-0836. DOI: 10.1038/35106527.

[Pfl04] C. Pfleiderer et al. "Partial order in the non-Fermi-liquid phase of MnSi". In: *Nature* 427 (2004), pp. 227–231. DOI: 10.1038/nature02232.

[PR10] C. Pfleiderer and A. Rosch. "Condensed-matter physics: Single skyrmions spotted". In: *Nature* 465 (7300) (June 2010), pp. 880–881. ISSN: 0028-0836.

[Phi71] H. Philipp. "Optical properties of non-crystalline Si, SiO, SiOx and SiO_2". In: *J. Phys. Chem. Solids* 32 (8) (1971), pp. 1935–1945. ISSN: 0022-3697. DOI: 10.1016/S0022-3697(71)80159-2.

[Poh13] C. Pohl et al. “Multilayer structures of silicon-suboxide embedded in single crystal silicon”. submitted to *J. Cryst. Growth*. Aug. 2013.

[Pri04] E. Prince, ed. *International Tables for Crystallography, Volume C*. 3rd. Kluwer Academic Publishers Dordrecht/Boston/London, 2004, p. 1020.

[Raa12] N. Raab. “Molekularstrahlepitaxie und Charakterisierung von Si/SiO_x- Schichtstrukturen”. unpublished. MA thesis. Julius-Maximilians-Universität Würzburg, Oct. 2012.

[Rab91] T. A. Rabedeau et al. “X-ray scattering studies of the SiO_2/Si(001) interfacial structure”. In: *Appl. Phys. Lett.* 59 (6) (1991), pp. 706–708. DOI: 10.1063/1.105371.

[Ren91] G. Renaud et al. “Native oxidation of the Si(001) surface: Evidence for an interfacial phase”. In: *Appl. Phys. Lett.* 58 (10) (1991), pp. 1044–1046. DOI: 10.1063/1.104418.

[Roc97] F. Rochet et al. “Suboxides at the Si/SiO_2 interface: a Si2p core level study with synchrotron radiation”. In: *J. Non-Cryst. Solids* 216 (0) (1997), pp. 148–155. ISSN: 0022-3093. DOI: 10.1016/S0022-3093(97)00181-6.

[Rub90] G. W. Rubloff. “Defect microchemistry in SiO_2/Si structures”. In: *Journal of Vacuum Science & Technology A: Vacuum, Surfaces, and Films* 8 (3) (1990), pp. 1857–1863. DOI: 10.1116/1.576816.

[SI91] D. Sander and H. Ibach. “Experimental determination of adsorbate-induced surface stress: Oxygen on Si(111) and Si(100)”. In: *Phys. Rev. B* 43 (5 Feb. 1991), pp. 4263–4267. DOI: 10.1103/PhysRevB.43.4263.

[Sch05] K. Schwinge et al. “Structure and magneto-optic Kerr measurements of epitaxial MnSi films on Si(111)”. In: *J. Appl. Phys.* 97 (10), 103913 (2005), p. 103913. DOI: 10.1063/1.1900934.

[SL83] V. Scott and G. Love. *Quantitative Electron Probe Microanalysis*. ISBN 0-85312-514-7. Ellis Horwood Limited, 1983, p. 350.

[SEP96] J. V. Seiple, C. Ebner, and J. P. Pelz. “Oxide-cluster nucleation, growth, and saturation on Si(001)-(2×1) surfaces: Atomic-scale measurements and models”. In: *Phys. Rev. B* 53 (23 June 1996), pp. 15432–15435. DOI: 10.1103/PhysRevB.53.15432.

[SP95] J. V. Seiple and J. P. Pelz. “Evolution of atomic-scale roughening on Si(001)-(2×1) surfaces resulting from high temperature oxidation”. In: *Journal of

Vacuum Science & Technology A: Vacuum, Surfaces, and Films 13 (3) (1995), pp. 772–776. DOI: 10.1116/1.579825.

[Shi97] S. Shivaprasad et al. “The formation of MnSi(111) interface at room and high temperatures”. In: *Surf. Sci.* 382 (13) (1997), pp. 258–265. ISSN: 0039-6028. DOI: 10.1016/S0039-6028(97)00161-1.

[SG82] F. W. Smith and G. Ghidini. “Reaction of oxygen with Si(111) and (100): Critical conditions for the growth of SiO_2”. In: *J. Electrochem. Soc.* 129 (6) (1982), pp. 1300–1306. DOI: 10.1149/1.2124122.

[Smi71] J. E. Smith et al. “Raman spectra of amorphous Si and related tetrahedrally bonded semiconductors”. In: *Phys. Rev. Lett.* 26 (11 Mar. 1971), pp. 642–646. DOI: 10.1103/PhysRevLett.26.642.

[Sti02a] A. Sticht et al. “Thin SiO_x layers embedded in single crystalline silicon”. In: *Physica E: Low-dimensional Systems and Nanostructures* 13 (2-4) (2002), pp. 978–981. ISSN: 1386-9477. DOI: DOI:10.1016/S1386-9477(02)00249-7.

[Sti02b] A. Sticht. “Herstellung und Charakterisierung von dünnen Silizium/Siliziumoxid-Schichtsystemen”. PhD thesis. Walter Schottky Institut, Technische Universität München, 2002.

[Sti07] S. M. Stishov et al. “Magnetic phase transition in the itinerant helimagnet MnSi: Thermodynamic and transport properties”. In: *Phys. Rev. B* 76 (5 Aug. 2007), p. 052405. DOI: 10.1103/PhysRevB.76.052405.

[SP11] S. M. Stishov and A. E. Petrova. “Itinerant helimagnet MnSi”. In: *Phys. Usp.* 54 (11) (2011), p. 1117. DOI: 10.3367/UFNe.0181.201111b.1157.

[Str11] A. Stranz et al. “Nanowire silicon as a material for thermoelectric energy conversion”. In: *Microsystem Technologies* 17 (2011). 10.1007/s00542-011-1390-z, pp. 1–6. ISSN: 0946-7076.

[Sue99] M. Suemitsu et al. “Initial Oxidation of Si(100)- (2×1) as an Autocatalytic Reaction”. In: *Phys. Rev. Lett.* 82 (11 Mar. 1999), pp. 2334–2337. DOI: 10.1103/PhysRevLett.82.2334.

[SBE91] Y.-K. Sun, D. J. Bonser, and T. Engel. “Spatial inhomogeneity and void-growth kinetics in the decomposition of ultrathin oxide overlayers on Si(100)”. In: *Phys. Rev. B* 43 (17 June 1991), pp. 14309–14312. DOI: 10.1103/PhysRevB.43.14309.

[Sut09] H. Suto et al. “Growth process and surface structure of MnSi on Si(111)”. In: *Surf. Sci.* 603 (1) (2009), pp. 226–231. ISSN: 0039-6028. DOI: 10.1016/j.susc.2008.11.008.

[Tan85] M. Tanaka et al. “Crystal chirality and helicity of the helical spin density wave in MnSi. I. Convergent-beam electron diffraction”. In: *Journal of the Physical Society of Japan* 54 (8) (1985), pp. 2970–2974. DOI: 10.1143/JPSJ.54.2970.

[TP89] L. Tapfer and K. Ploog. “X-ray interference in ultrathin epitaxial layers: A versatile method for the structural analysis of single quantum wells and heterointerfaces”. In: *Phys. Rev. B* 40 (14) (Nov. 1989), pp. 9802–9810. DOI: 10.1103/PhysRevB.40.9802.

[Tem75] R. Temkin. “An analysis of the radial distribution function of SiO_x”. In: *J. Non-Cryst. Solids* 17 (2) (1975), pp. 215–230. ISSN: 0022-3093. DOI: 10.1016/0022-3093(75)90052-6.

[The95] C. Thessieu et al. “Magnetism and spin fluctuations in a weak itinerant ferromagnet: MnSi”. In: *Solid State Commun.* 95 (10) (1995), pp. 707–712. ISSN: 0038-1098. DOI: 10.1016/0038-1098(95)00356-8.

[TFL89] J. Thompson, Z. Fisk, and G. Lonzarich. “Perspective on heavy-electron and Kondo-lattice systems from high pressure studies”. In: *Physica B: Condensed Matter* 161 (1-3) (1989), pp. 317–323. ISSN: 0921-4526. DOI: 10.1016/0921-4526(89)90155-5.

[Tit10] T. Tite et al. “Structural and thermal properties of MnSi single crystal”. In: *Appl. Phys. Lett.* 97 (3), 031909 (2010), p. 031909. DOI: 10.1063/1.3464980.

[Tok90] H. Tokumoto et al. “Real-time observation of oxygen and hydrogen adsorption on silicon surfaces by scanning tunneling microscopy”. In: *Journal of Vacuum Science & Technology A: Vacuum, Surfaces, and Films* 8 (1) (1990), pp. 255–258. DOI: 10.1116/1.577079.

[TTN01] D. Tsoukalas, C. Tsamis, and P. Normand. “Diffusivity measurements of silicon in silicon dioxide layers using isotopically pure material”. In: *J. Appl. Phys.* 89 (12) (2001), pp. 7809–7813. DOI: 10.1063/1.1371003.

[TT00] Y. Tu and J. Tersoff. “Structure and Energetics of the Si-SiO_2 Interface”. In: *Phys. Rev. Lett.* 84 (19 May 2000), pp. 4393–4396. DOI: 10.1103/PhysRevLett.84.4393.

[Uem04] M. Uematsu et al. “Modeling of Si self-diffusion in SiO_2: Effect of the Si/SiO_2 interface including time-dependent diffusivity”. In: *Appl. Phys. Lett.* 84 (6) (2004), pp. 876–878. DOI: 10.1063/1.1644623.

[Veg21] L. Vegard. “Die Konstitution der Mischkristalle und die Raumfüllung der Atome”. German. In: *Zeitschrift für Physik* 5 (1 1921), pp. 17–26. ISSN: 0044-3328. DOI: 10.1007/BF01349680.

[Ven01] R. Venkatasubramanian et al. “Thin-film thermoelectric devices with high room-temperature figures of merit”. In: *Nature* 413 (6856) (Oct. 2001), pp. 594–602. DOI: 10.1038/35098012.

[VB01] J. C. Vickerman and D. Briggs, eds. *ToF-SIMS: Surface Analysis by Mass Spectometry*. IM Publications, 2001. ISBN: 1-901019-03-9.

[Wag79] C. D. Wagner et al. *Handbook of X-ray Photoelectron Spectroscopy*. Ed. by G. E. Muilenberg. Perkin-Elmer Corporation, 1979, p. 190. DOI: 10.1002/sia.740030412.

[War69] B. E. Warren. *X-Ray Diffraction*. Dover Books on Physics Series. Dover Publications, 1969, p. 374. ISBN: 978-0-486-66317-3.

[WWS97] Y. Wei, R. M. Wallace, and A. C. Seabaugh. “Controlled growth of SiO_2 tunnel barrier and crystalline Si quantum wells for Si resonant tunneling diodes”. In: *J. Appl. Phys.* 81 (9) (1997), pp. 6415–6424. ISSN: 00218979. DOI: 10.1063/1.364422.

[WWS72] J. Wernick, G. Wertheim, and R. Sherwood. “Magnetic behavior of the monosilicides of the 3d-transition elements”. In: *Materials Research Bulletin* 7 (12) (1972), pp. 1431 –1441. ISSN: 0025-5408. DOI: 10.1016/0025-5408(72)90180-8.

[WHW07] E. Wieberg, A. F. Holleman, and N. Wieberg. *Lehrbuch der Anorganischen Chemie*. 102nd ed. Walter de Gruyter, 2007.

[Wie77] H. Wiesmann et al. “Simple model for characterizing the electrical resistivity in A−15 superconductors”. In: *Phys. Rev. Lett.* 38 (14 Apr. 1977), pp. 782–785. DOI: 10.1103/PhysRevLett.38.782.

[WC96] D. Williams and C. Carter. *Transmission Electron Microscopy*. Plenum Press New York, 1996, p. 720. ISBN: 0-306-45247-2.

[Wu04] H. Wu et al. “First-Principles study of ferromagnetism in epitaxial Si-Mn thin films on Si(001)”. In: *Phys. Rev. Lett.* 92 (23 June 2004), p. 237202. DOI: 10.1103/PhysRevLett.92.237202.

[YC10] P. Y. Yu and M. Cardona. *Fundamentals of Semiconductors*. English. 4th. Graduate Texts in Physics. Springer Berlin Heidelberg, 2010, p. 793. ISBN: 978-3-642-00709-5. DOI: 10.1007/978-3-642-00710-1_2.

[Zha02] Q. Zhang et al. “Analytical UHV transmission electron microscopy studies of electronic structure changes between as-deposited Mn and Mn silicide on Si(111) surface”. In: *Surf. Sci.* 507-510 (0) (2002), pp. 453–457. ISSN: 0039-6028. DOI: 10.1016/S0039-6028(02)01403-6.

[ZS61] N. N. Zhuravlev and A. A. Stepanova. “X-ray determination of the thermal expansion coefficients of manganese and cobalt monosilicides”. In: *Atomnaya Energiya* 13 (2) (1961), pp. 183–184.

[ZL11] Z.-Q. Zou and W.-C. Li. “Two-dimensional fractal-like growth on semiconductors: The formation of continuous manganese monosilicide ultrathin films on Si(111)”. In: *Phys. Lett. A* 375 (4) (2011), pp. 849–854. ISSN: 0375-9601. DOI: 10.1016/j.physleta.2010.12.039.

Acknowledgment

I am thankful to all those who have contributed to this work, be it subject related or outside the world of physics. Without you I would not have succeeded with this endeavor.

I owe special thanks to my supervisor Prof. Karl Brunner for offering me the PhD position and his help and support throughout the last four years. Especially during the times, that were unfortunately not rare enough, when the lab descended into chaos and we had to pick parts of a turbo pump out of the chamber or we had to drain water from it.

I would like to thank Prof. Laurens W. Molenkamp for the possibility to work in the EP3 and to benefit from the vast and excellent infrastructure he has built in his chair.

For the cooperation, assistance and great general atmosphere in the EP3 I would like to thank all of my colleagues. I thank Claus Schumacher for his advice on technical and organizational questions. For the great atmosphere in our office, an open ear and helping hand when needed I thank Christopher Ames and Steffen Schreyeck. My masters students Nico Raab and Martin Mitterer have been very helpful and deserve a special thanks, without them this work could not have been done in this time. For discussions and the welcome diversions I would like to thank Rebekka, Tsvetelina, Philipp, Holger, Lars and Petra. I thank Greg Karczewski for proof-reading this thesis.

The technical staff of EP3 and the staff of the mechanic and electronic workshop have contributed a great deal to this work. Without their support I would not have been able to get the MBE up and running, time and time again. I especially would like to express my gratitude to Matin Zipf, Alfred Schönteich, Volkmar Hock, Petra Wolf-Müller, Jana Hinterberger, Rainer Brauner, Thomas Grünebaum, Franz Krause and Heinz Rüb.

I would like to express my heartfelt gratitude to Friederike for always supporting me and pointing out that silver lining on the horizon when I couldn't see it. My sister, Stefanie, although far away, supported me and even found the time to look for all the typos and spelling errors. And of course my parents, I am very thankful for all they have done for me over all these years. They have always been patient and supporting but knew when it was time to give me a push forward. Thank you.